https://ntrs.nasa.gov/search.jsp?R=19720009093 2018-05-25T16:34:40+00:00Z

N72-16743

NATIONAL AERONAUTICS AND SPACE ADMINISTRATION

Technical Report 32-1550

Mariner Mars 1971 Project Final Report

Volume II. Preliminary Science Results

Prepared by

Mariner Mars 1971 Science Experimenter Teams

CASE FILE COPY

JET PROPULSION LABORATORY
CALIFORNIA INSTITUTE OF TECHNOLOGY
PASADENA, CALIFORNIA

February 1, 1972

NATIONAL AERONAUTICS AND SPACE ADMINISTRATION

Technical Report 32-1550

Mariner Mars 1971 Project Final Report

Volume II. Preliminary Science Results

Prepared by
Mariner Mars 1971 Science Experimenter Teams

JET PROPULSION LABORATORY
CALIFORNIA INSTITUTE OF TECHNOLOGY
PASADENA, CALIFORNIA

February 1, 1972

Preface

This four-volume document constitutes the *Mariner* Mars 1971 Project Final Report.

Volume I of this Technical Report consists of Project development through launch and first trajectory-correction maneuver. Volume II presents the preliminary science results derived from data evaluation to December 14, 1971. The information contained in this volume has appeared in *Science*, Vol. 175, January 1972. Volume III covers flight operations after the first trajectory-correction maneuver and during the basic 90-day orbital mission. Volume IV consists of the science results derived from the basic 90-day orbital mission and experimenters' interpretations of the data.

Contents

I. Summary 1

R. H. Steinbacher, A. J. Kliore, J. Lorell, H. Hipsher, C. A. Barth, H. Masursky, G. Münch, J. Pearl, and B. Smith

References 3

Acknowledgment 3

II. Television Reconnaissance of Mars and its Satellites 5

H. Masursky, R. M. Batson, M. H. Carr, J. F. McCauley, D. J. Milton, L. A. Soderblom, R. L. Wildey, D. E. Wilhelms, B. A. Smith, T. B. Kirby, J. C. Robinson, C. B. Leovy, G. A. Briggs, T. C. Duxbury, C. H. Acton, Jr., B. C. Murray, J. A. Cutts, R. B. Leighton, R. P. Sharp, Susan Smith, C. Sagan, J. Veverka, M. Noland, J. Lederberg, E. Levinthal, J. B. Pollack, J. T. Moore, Jr., W. K. Hartmann, E. N. Shipley, G. de Vaucouleurs, and M. E. Davies

A. Atmospheric Phenomena 8

1. Photometric Function 8

2. Visibility of Surface Features 8

3. Structure of the Limb 10

4. Atmospheric Waves 12

5. Interpretations 13

B. Surface Features of the South Polar Region 14

C. Geology 14

D. Satellite Astronomy 22

References 25

Acknowledgment 26

III. Infrared Spectroscopy Experiment 27

R. A. Hanel, B. J. Conrath, W. A. Hovis, V. G. Kunde, P. D. Lowman, J. C. Pearl, C. Prabhakara, B. Schlachman, and G. V. Levin

References 32

Acknowledgment 33

IV. Infrared Radiometry Experiment 35

S. C. Chase, Jr., H. Hatzenbeler, H. H. Kieffer, E. Miner, G. Münch, and G. Neugebauer

References 36

Acknowledgment 37

Contents (contd)

V. Ultraviolet Spectrometer Experiment 39

C. A. Barth, C. W. Hord, A. I. Stewart, and A. L. Lane

A. Upper Atmosphere 39

B. Lower Atmosphere 42

C. Phobos 44

D. Summary 45

References 45

Acknowledgment 46

VI. S-Band Occultation Experiment: Atmosphere, Ionosphere, and Topography of Mars 47

A. J. Kliore, D. L. Cain, G. Fjeldbo, B. L. Seidel, and S. I. Rasool

References 57

Acknowledgment 57

VII. Celestial Mechanics Experiment: Gravity Field Pole Direction of Mars 59

J. Lorell, C. H. Born, E. J. Christensen, J. F. Jordan, P. A. Laing, W. L. Martin, W. L. Sjogren, I. I. Shapiro, R. D. Reasenberg, and G. L. Slater

References 65

Acknowledgment 66

Figures

II-1. (a) Earth-based photograph of Mars. (b) *Mariner 7* picture of Nix Olympica and the three dark spots. (c) *Mariner 9* picture of same region shown in (b). (d) *Mariner 9* mosaic of the four dark spots. (e) Filtered *Mariner 9* picture of South Spot 7

II-2. Relative brightness profiles across the polar cap edge, measured with the narrow-angle camera 9

II-3. Limb views from Rev 16 10

II-4. Mercator map showing approximate locations of wave clouds visible in some wide-angle pictures 11

II-5. Detached haze layer located near the terminator on Rev 29 . . . 12

II-6. Terminator wave clouds from wide-angle frame on Rev 18 . . . 13

II-7. *Mariner 9* and *Mariner 7* views of the south polar cap 15

II-8. Details of the south polar cap 16

Contents (contd)

Figures (contd)

II-9. *Mariner 9* pictures displaying the gradual disappearance of the residual polar cap 17

II-10. Narrow-angle views of craters in the dark spots, rectified on the basis of preliminary orbital data 19

II-11. Narrow-angle picture from Rev 42 showing linear scarps 20

II-12. Evidence of topographic control of atmosphere features 21

II-13. Field of sinuous features near the south pole 22

II-14. Computer-enhanced picture of Deimos 23

II-15. Computer-enhanced pictures of Phobos 24

II-16. Brightness traces across the two prominent craters on Deimos . . . 25

III-1. Examples of non-polar and polar thermal emission spectra. (a) Non-polar. (b) polar 29

III-2. Temperature as a function of atmospheric pressure level for three Martian locations 30

III-3. Isotherms for a cross section obtained from a single pass in the south polar region 31

III-4. Portion of the south polar cap spectrum of Fig. III-1b shown on an expanded scale (a); spectral lines appearing in emission are due to rotational water vapor lines in lower Martian atmosphere. Synthetic water vapor spectrum (b) included for comparison 32

V-1. Airglow spectrum of Mars between 1910 and 2460 Å 40

V-2. Airglow spectrum of Mars between 1420 and 1760 Å 40

V-3. Emission rates of the CO a-X Cameron bands and the sum of the CO A-X fourth positive 41

V-4. Apparent emission rates of the atomic hydrogen 1216 Å line and the atomic oxygen 1304 Å line as a function of altitude . . . 41

V-5. Ultraviolet reflectance in dusty region 43

V-6. Ultraviolet reflectance in polar region 43

V-7. Reflectance at 3050 Å and blue and red color ratios for Rev 48 observations 44

V-8. Phobos ultraviolet reflectance 45

VI-1. Locations of occultation measurement points on the surface of Mars 49

VI-2. Atmospheric temperature profiles for Rev 1 through 9 50

VI-3. Atmospheric temperature profiles for Revs 10 through 17 51

I. Summary

R. H. Steinbacher, A. J. Kliore, and J. Lorell
Jet Propulsion Laboratory, Pasadena, California

H. Hipsher
NASA Headquarters, Washington, D.C.

G. Münch
California Institute of Technology, Pasadena

C. A. Barth
University of Colorado, Boulder

J. Pearl
Goddard Space Flight Center, Greenbelt, Maryland

H. Masursky
U.S. Geological Survey, Flagstaff, Arizona

B. Smith
New Mexico State University, Las Cruces

Mariner 9 was launched from Cape Kennedy, Florida, at 22:23:04 GMT on May 30, 1971. On June 5, 6 days after launch, a trajectory-correction maneuver placed the spacecraft's aiming point closer to Mars with such accuracy that no additional trajectory corrections were necessary. *Mariner* was inserted successfully into orbit[1] with a 15-min, 23-sec motor burn completed on November 14, 00:15:29 GMT, becoming the first man-made object to orbit the red planet.

To form the science payload, NASA had selected six experiments: television, infrared spectroscopy, infrared radiometry, ultraviolet spectrometer, S-band occultation, and celestial mechanics (Ref. I-1). A brief summary of results from these experiments, for the first 30 days after orbit insertion, is presented in the subsequent paragraphs. More detailed information from each experiment is given in the following sections of this document.

At the time of arrival of *Mariner* 9 at Mars, there was a planet-wide obscuration, by dust, of surface features viewed by means of the television experiment. Obscuration caused by dust was confirmed by the infrared spectroscopy, infrared radiometry, and ultraviolet spectrometer experiments; and supported by the S-band occultation experiment. Several instruments observed less dust entrained over the south polar region than over many other areas, even allowing for the intrinsic contrast of polar cap features. High elevations—notably the three spots in Tharsis—were relatively clear, although surface detail also was visible in some regions of lower altitude. A slow and sporadic clearing of the dust is evident in television pictures of the south polar and other regions; such a progressive clearing is not inconsistent with results from the other science instruments. The progress of dust clearing is a complex meteorological phenomenon; to date, no one-to-one connection of clearing with latitude, longitude, elevation, or time has been found.

Confirmation by the *Mariner* 9 ultraviolet spectrometer (UVS) of the observations of CO and O airglow made by the UVS on *Mariners* 6 and 7 in 1969 and the

[1]See Table VII-2 for *Mariner* 9 orbital parameters.

detection of the 15-μm CO_2 band by the infrared interferometer spectrometer (IRIS) are consistent with a predominantly CO_2 atmosphere. The IRIS observation of H_2O rotational lines in the lower atmosphere and UVS detection of the water vapor dissociation products, H and O, in the upper atmosphere are mutually complementary results. Above the dust, water vapor is photodissociated, while the infrared observation penetrates to a deeper level in the Martian atmosphere to observe the water vapor lines.

In agreement with theory that predicts the formation of an ionosphere from a predominantly CO_2 upper atmosphere, the average plasma scale height of about 38 km, as determined by means of the S-band occultation experiment, is about twice the neutral scale height of about 20 km measured by the UVS. The upper-atmosphere temperature derived from these results is lower than that measured in 1969 and higher than in 1964, reflecting the change in solar activity between these times of measurement.

The mid-latitude temperature profiles of the Martian lower atmosphere, as determined by IRIS and the S-band occultation experiment, are more isothermal than the subadiabatic profiles determined by the 1969 occultation measurements, which were at that time somewhat more isothermal than generally expected for these latitudes and seasons (Ref. I-2). The mean temperatures at all tropospheric levels also are higher than expected. A reasonable explanation is solar energy deposition in the first 1 or 2 scale heights due to absorption by entrained dust. The reduced UVS Rayleigh scattering at normal viewing in 1971 compared with 1969 also implies significant dust in at least the lowest scale height. An intriguing question is whether a subadiabatic atmosphere implies the absence of convection when significant thermal exchange processes involving dust are present. Infrared results suggest significant thermal coupling among particles and gas. In the absence of convective support, particles entrained for 30 days at several scale heights will, from the Stokes–Cunningham equation, have diameters less than several micrometers (Ref. I-3). With convection, larger particles may be present in the middle troposphere. Detached limb hazes are visible in television pictures at 60-km altitude, but whether these are dust or condensates is indeterminate at present.

In contrast to the more isothermal atmospheric temperature profiles observed at lower latitudes, a region of strong temperature inversion exists near the south polar cap. This suggests a relation with the relative absence of atmospheric dust in this area.

The interpretation of the spectral and radiometric infrared measurements over the polar cap does not allow, at present, a decisive inference of the composition of the residual polar cap.

The margin of the remnant of the south polar cap viewed in 1971 is remarkably regular and uniform compared with the cap margin observed in 1969. This observation indicates that the underlying topography is more uniform and less cratered than the frost-covered area at the edge of the cap as viewed in 1969. The emergence of certain areas of the cap during the period of observation indicates that the frost cover is only a few centimeters thick in these areas. The thickness of the frost in other areas is still undetermined. The frost-covered curvilinear features observed in 1969 are frost free in 1971; comparison with frost-free crater rims and frost-covered crater floors indicates that the curvilinear features may be ridges.

The S-band occultation experiment revealed overall elevation differences of about 12 km, with an associated variation in atmospheric surface pressure of about 3 to 8 mb. The floor of Hellas is a low area, lying about 6 km below its western rim (4 km below the mean radius) and gradually sloping up toward the east. This finding is in good agreement with the pressure mapping results from the ultraviolet and infrared spectrometers on *Mariner* 7. The area at 33 to 40°S latitude between Mare Sirenum and Solis Lacus is elevated by 5 to 8 km, in good agreement with planetary ranging results at more northerly latitudes. Radius measurements from the S-band occultation experiment are consistent with a mean equatorial radius of 3394 km.

Dynamical measurements give broad-scale elevation contours that are compatible with radar and occultation elevations. The variations are much greater than would be expected by scaling from the Earth and the Moon, implying large crustal stresses. Equatorial variations in the dynamical measurements have a high of 3 km in the area of Tharsis, where the radar profile peaks at 8 km above the mean radius. These values suggest that less dense rocks underlie the Tharsis ridge. The picture of the possible volcanic vents along this ridge is consistent with this suggestion.

From the IRIS data, it is suggested that the composition of the Martian dust corresponds approximately to that of rocks of intermediate SiO_2 content (55 to 65 wt %). The form of the possible volcanic vents at Nix Olympica and the three spots along the Tharsis ridge is consistent with this intermediate igneous rock composition, and therefore implies planetary differentiation.

The large dynamical pole flattening obtained from satellite observations has been confirmed by the *Mariner* 9 data. The effect of this flattening on the spacecraft's orbit has been used to improve knowledge of the polar axis direction; television picture measurements confirm these results. Television pictures also have been used metrically to improve the ephemerides of the orbits of the Martian satellites, Phobos and Deimos.

Close-up views of Phobos and Deimos, obtained for the first time, show irregular, cratered surfaces of low visual albedo. Data from the UVS indicate an ultraviolet albedo lower than, but a reddish color similar to, that of Mars.

References

I-1. "Mariner Mars 1971 Experiments," *Icarus,* Vol. 12, pp. 3–90, Jan. 1970.

I-2. Gierasch, P., and Goody, R., *Planet. Space Sci.*, Vol. 16, p. 615, 1968.

I-3. Pollack, J. B., and Sagan, C., *Space Sci. Rev.*, Vol. 9, p. 243, 1969.

Acknowledgment

The authors thank Dr. C. Sagan, Cornell University, for his advice and support in preparing this material. Special recognition is extended to T. Vrebalovich, A. B. Whitehead, S. Gunter, and E. Christensen for guiding the science activities during the first 30 days of a "dusty" Mars mission.

II. Television Reconnaissance of Mars and Its Satellites

H. Masursky, R. M. Batson, M. H. Carr, J. F. McCauley, D. J. Milton, L. A. Soderblom, R. L. Wildey, and D. E. Wilhelms
Branch of Astrogeologic Studies, U. S. Geological Survey, Flagstaff, Arizona, and Menlo Park, California

B. A. Smith, T. B. Kirby, and J. C. Robinson
New Mexico State University, Las Cruces

C. B. Leovy
University of Washington, Seattle

G. A. Briggs, T. C. Duxbury, and C. H. Acton, Jr.
Jet Propulsion Laboratory, Pasadena, California

B. C. Murray, J. A. Cutts, R. B. Leighton, R. P. Sharp and Susan Smith
California Institute of Technology, Pasadena

C. Sagan, J. Veverka, and M. Noland
Cornell University, Ithaca, New York

J. Lederberg and E. Levinthal
Stanford University School of Medicine, California

J. B. Pollack and J. T. Moore, Jr.
Ames Research Center, Moffett Field, California

W. K. Hartmann
IIT Research Institute, Tucson, Arizona

E. N. Shipley
Bellcomm, Inc., Washington, D.C.

G. de Vaucouleurs
The University of Texas, Austin

M. E. Davies
Rand Corporation, Santa Monica, California

Mariner 9 arrived at Mars on November 14, 1971, during a planet-wide dust storm of unusual intensity. While forcing the postponement of most geologic and cartographic objectives, the storm has provided an unparalleled opportunity to examine at close range a phenomenon connected with Martian meteorology, topography, depositional and erosional processes, and variable features.

On September 22, Earth-based observers (Ref. II-1) recorded a bright yellow cloud that had developed over Noachis, in the mid-southern latitudes of Mars. It spread rapidly over the rest of the planet, and in a little more than 2 weeks the entire visible globe was covered by dust; even the south polar cap had disappeared from view of Earth-based telescopes. By the fifth week, the dust storm had reached its peak, exceeding all previously observed Martian storms in obscuration, areal extent, and duration. Over the next several weeks, the atmosphere of Mars showed a gradual clearing, and the south polar cap reappeared. Upon its arrival, *Mariner* 9 found the obscuration still severe.

As Mars rotated in view of the approaching spacecraft, three pre-orbital science (POS) sequences of pictures were taken, giving total global coverage of the dust-shrouded planet. Only five distinct features could be seen: the south polar cap and four dark spots (Fig. II-1). One of these has been identified as Nix Olympica, and the other three (provisionally labeled North, Middle, and South Spots) have been identified with a group of features that become bright (the "W-cloud"; see Ref. II-2) during the Martian afternoon at certain seasons. The rest of Mars was veiled by heavy, but regionally variable, atmospheric dust. It was apparent that Mars was not the same planet for which this mission had been planned.

Gradual clearing began during the third week of orbital operations. The degree of obscuration varies from region to region, with the south polar region, for example, remaining consistently clearer than other parts of the planet. However, as of this writing (mid-December), Mars must still be described as heavily obscured.

The dust storm has had a pronounced effect on the original mission plan (Ref. II-3), which included both global surveillance of Mars and contiguous, high-resolution "mapping" sequences near periapsis. The mapping sequences were soon found to be ineffective: Dust obscuration varied widely from one region to another, but the mapping sequences could not be made sufficiently flexible to take advantage of regions that were relatively clear. Periapsis was located close to the evening terminator where the more diffuse illumination at the surface severely degrades surface contrast. It was necessary to direct the high-resolution photography to the few places where it would be effective. Therefore, a new mission plan, the "reconnaissance mode," was developed and implemented on Revolution (Rev) 26, the earliest possible opportunity. This mode included global coverage each revolution, from which specific targets in relatively clear areas could be located, and two groups of four high-resolution frames each (tetrads), which could be placed on such targets.

The *Mariner* 9 spacecraft is equipped with two television cameras (Ref. II-3) similar to those flown on *Mariners 6* and *7*. The wide-angle camera has a field of view of 11° by 14° and employs eight interchangeable filters (Table II-1). The narrow-angle camera has a field of view of 1.1° by 1.4° and is equipped with a fixed yellow filter. Thirty-one pictures are taken on each revolution of 12 hr.

Table II-1. Camera filters

Camera	Filter type	Effective wavelength,[a] μm
Wide angle	Orange	0.610
Wide angle	Green	0.545
Wide angle	Blue	0.477
Wide angle	Violet	0.414
Wide angle	Polarization[b]	0.565
Wide angle	Yellow (minus blue)	0.560
Narrow angle	Yellow (minus blue)	0.558

a For sunlight.

b Three filters with axes spaced in 120° steps.

Caution must be used in interpreting the details visible in the pictures shown in this document.[1] Ordinarily, the contrast of visible detail on Mars is some tens of percent. However, the 1971 dust storm has drastically reduced contrasts. In order to make visible any detail other than the polar cap and the four dark spots, it has been necessary to increase the contrast of the *Mariner* 9 pictures by much more than the usual photographic factor of 2 or 3.

Some of the pictures reproduced here (e.g., Figs. II-12c and II-13) have been photometrically "stretched" so that a small brightness range (usually about 20% of the original range of the data) is expanded to cover the full range from white to black. This technique (Ref. II-4) is limited by the strong limb-to-terminator brightness gradient (see Fig. II-1c). It is not practical to increase contrast more without first removing the average brightness gradients across a picture. This is accomplished by subtracting a running mean (e.g., 175 consecutive picture elements or samples along each line) from the signal level at each sample in the original data. Thus, features much larger than 175 samples in width are removed from the data. The remaining small-detail modulation, typically on the order of a few percent, then can be expanded to cover the full range from white to black. In this way, the contrast of small detail can be increased by a factor of about 50. The process amounts to a high-(spatial)-frequency filter, followed by severe "stretching" as described; the products are, for brevity, called "filtered."

It is essential to bear in mind the enormous exaggeration of contrast in such filtered pictures. Most of the

[1]Ordering information for pictures presented is included in each figure caption. Pictures may be ordered through the National Space Science Data Center, Greenbelt, Maryland.

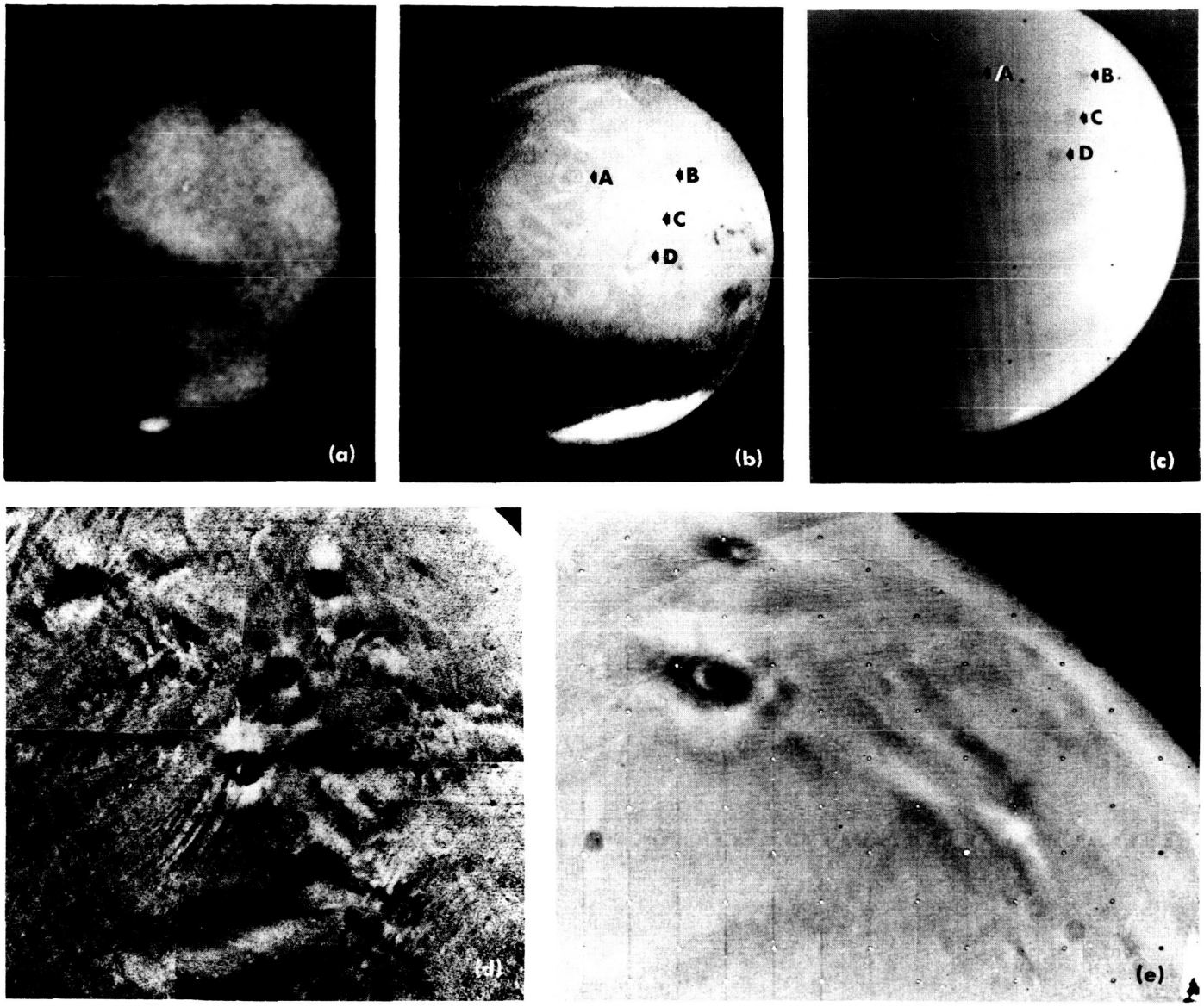

Fig. II-1. (a) Earth-based telescopic photograph of Mars by E. C. Slipher during the 1956 dust storm (Ref. II-7). The dark spot at the top is an example of several such temporary features observed when the planetary surface has been largely obscured by dust. (b) Computer-enhanced picture of Mars taken by *Mariner 7* in 1969 (7F74), showing Nix Olympica (A) with its ringed appearance and three aligned crater-like features (B, C, D) that make up part of the "W-cloud" complex. (c) Slightly enhanced picture of the same region taken by *Mariner 9* during POS 2 about 1½ days before insertion (Image Processing Laboratory Roll 147, 113230). The small south polar cap shows at the bottom of the planet's disk. A dark spot identified with Nix Olympica (A) and three aligned dark spots (B, C, D) that lie on the western part of the "W-cloud" complex are visible. The very low contrast is due to obscuration by the planet-wide dust cloud. (d) Filtered mosaic of the four dark spots, taken 1 day later, showing streaks running 100 km south of South Spot (P-12676). The bright wings on either side of each dark spot are artifacts of the filtering. (e) Filtered picture of South Spot, taken on Rev 24 about 13 days later than (d), with the streaks extending south of South Spot no longer visible (Image Processing Laboratory Roll 909, 123836). The streaks reappeared in subsequent pictures.

detail in the *Mariner 9* pictures actually has an order of magnitude *less* contrast than the weakest telescopic details seen on Mars from the Earth. Some examples may help in understanding this contrast exaggeration, as well as certain artifacts:

(1) Most filtered pictures show a prominent pattern of diffuse vertical stripes, caused by electronic noise on the spacecraft (e.g., Fig. II-11). The peak-to-peak amplitude of this noise is typically a few tenths of 1%, but it is easily visible because it has been amplified some tens of times.

(2) Reseau fiducial marks on the vidicon are about three samples across, and are almost black. When a reseau falls within the range of a running mean, it lowers the mean by about 2%. When this lowered mean is subtracted from a sample near the reseau, the sample appears to be about 2% brighter than the mean. Thus, on filtered pictures, each reseau is flanked by two bright lines (of combined length equal to the running-mean length) about 2% brighter than its surroundings. In most prints, these bright lines are almost at the white level (e.g., Fig. II-11).

(3) Both wide- and narrow-angle pictures show small circular blemishes, about 40 samples in diameter, which are the penumbral shadows of small dust specks on the vidicon faceplates. The contrast of the most prominent shadow is 5% in the wide-angle camera and 0.5% in the narrow-angle camera. These shadows are invisible on the raw pictures, but are prominent in both stretched and filtered pictures. (In filtered wide-angle pictures, they sometimes appear black; e.g., Figs. II-11 and II-12e.)

(4) A prominent feature of many pictures is a residual image of an earlier limb picture (see Fig. II-12c). This residual is about 10% in the first picture after the limb frame and decays slowly; it is about 5% on the next frame, 3% on the next, and so on (>1% for many frames). For example, the wide-angle pictures from Rev 2 showed prominent limb residuals from the last pre-orbital sequence. These residuals have about 1% peak contrast.

In many processed pictures, these artifacts—the streaks about the reseaus, the shadows of the dust specks, the limb residuals, or even the vertical noise—are more prominent than the images of real features on Mars, showing that the contrast in the scene is less than that of the artifacts. Features of such low contrast would be invisible to the human eye or on conventional photographs of Mars.

A. Atmospheric Phenomena

1. Photometric Function

The limb darkening of the planet is evident in pre-orbital data. If we assume that the limb darkening can be described by a Minnaert function (Refs. II-5, II-18), the darkening parameter, k,[2] is uniquely related to the position on the disk of maximum brightness, assuming an orthographic view (constant phase angle over the disk). This assumption is not quite met, but the angle subtended by the planet is less than 3° in the wide-angle-camera pictures taken just before orbit insertion. These pictures cover the full range of color filters in quick succession; the maximum value of k occurs on the terminator side of the subsolar point for orange, yellow, and green light, and on the limb side for blue and violet. The corresponding values of k progress regularly from 1.12 to 0.93 with decreasing wavelength, assuming a mean phase angle of 58°. The differences from a Lambertian surface ($k = 1.00$) are small, but significant: The limb is obviously bluer than the center of the disk.

Considering that surface features are, in general, hidden by the dust storm, the quasi-Lambertian limb darkening is not surprising, although data from *Mariner 4* (Ref. II-5) indicate much lower values of k (0.7 to 0.8). Lambertian surfaces can be approximated in the laboratory by powdered materials of low refractive index producing high-order multiple scattering. Thus, the present values of k near unity are consonant with an optically thick scattering atmosphere. Unlike a quasi-Lambertian sphere which exhibits elliptical isophotes centered on the subsolar point, the Martian isophotes are elongated toward the poles—consistent with a significant contribution from single scattering. Because the single scattering is nonconservative, single scattering represents an important fraction of the net albedo from multiple scattering. The weak absorption in the scattering is consistent with the scattering material being dust raised from the surface.

2. Visibility of Surface Features

The most prominent features in the POS pictures are the south polar cap and the four dark spots. The dark

[2]The darkening parameter, k, is defined in terms of the brightness, B; incidence angle, i; and emission angle, ϵ, by $B = B_0 (\cos i)^k (\cos \epsilon)^{k-1}$ in which the parameters B_0 and k are both functions of phase angle in general.

appearance of these spots is especially striking, as they are usually observed to be as bright, or brighter, than their surroundings. However, a dark feature of relatively high contrast, which may have been South Spot, was reported during the 1924 dust storm (Ref. II-6), and other temporary dark spots have been noted when the surface of Mars has been obscured by dust (Fig. II-1a). The maximum contrast[3] of the spots was 20% for Nix Olympica and 10% for South Spot, from *Mariner* 9. The contrast of the three aligned spots decreased as the spots rotated toward the early afternoon limb, but Nix Olympica lost contrast toward the limb on only one of the two POS sequences. This behavior suggests that the extinction optical depth, τ,[4] above the three aligned spots was about 1, but it may have been significantly less over Nix Olympica.

Because the south polar cap showed the highest contrast of any surface feature, and because it was observed frequently, it was a useful target for measuring variations in atmospheric extinction. It does not exhibit diurnal brightening as the spots sometimes do. Figure II-2 shows typical relative brightness profiles from narrow-angle frames across the edge of the cap. The shape of these profiles—a sharp jump in brightness with gradual variations on each side of the jump—may be due to a sharp-edge cap that appears somewhat diffuse because of atmospheric scattering of radiation reflected from both sides of the surface albedo boundary (Ref. II-8). An alternative interpretation of these brightness profile features, in terms of gradual variations in the intrinsic surface albedo on both sides of the cap edge, seems less likely. With the model of a sharp-edged cap, a contrast of 14% at the cap edge is derived on Rev 11. The normal contrast of the cap edge in yellow light is about 90%.[5] The contrast reduction of the Rev 11 narrow-angle picture suggests τ of about 1, reduced to the zenith, over the cap at that time. The contrast of the cap showed little variation during the first 2 weeks of the mission, but began to increase during the third week. By Rev 34, a narrow-angle picture showed significantly more contrast than the Rev 11 frame, and continued contrast increases have been observed on later revolutions. Evidently, τ decreased significantly during this time.

Nix Olympica, the three spots, and the south polar cap were the clearest regions on the planet; other albedo

[3]Contrast is defined here as the difference in brightness of the dark and light areas divided by the brightness of the dark area.

[4]Optical depth is the natural logarithm of the reciprocal of the atmospheric transmission factor. Extinction is the sum of attenuation caused by scattering and by absorption.

[5]Based on an average of 90% for *Mariner* 7 red and green pictures at a different season but similar illumination and a measurement of 60% in a Lowell Observatory plate at the same season and illumination. The latter value is expected to be somewhat below the true value beause of the small cap size in the image.

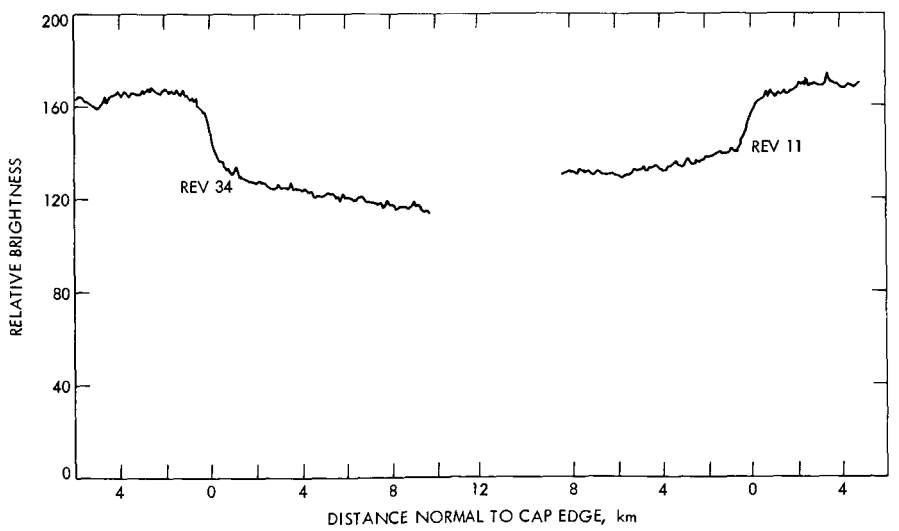

Fig. II-2. Relative brightness profiles across the polar cap edge, measured with the narrow-angle camera (yellow filter). The relatively sharp rise represents the discontinuity due to the edge of the polar cap. The gradual decrease in brightness on either side of the polar cap edge results from light scattering in the dust above the polar area.

features of large size also were faintly visible, primarily in the southern hemisphere. However, the disappearance of almost all of the classical albedo features and many craters suggests $\tau \geq 2$ over most of the planet. Craters, appearing as features of high albedo, can be seen in many pictures taken at high Sun angles. In general, craters and other albedo features were observed better in orange light than in violet. Some relatively low areas also appear bright, for example, the long, bright streaks in the regions of Ophir and Eos (e.g., Fig. II-12).

Except in Nix Olympica and the dark spots, surface relief (in contrast to surface albedo variations) could not be seen during the first 2 weeks. This can be attributed in part to very strong diffusion of incoming solar radiation by the haze so that surface illumination was nearly isotropic. During the third week, surface relief could be seen more readily, especially near the south polar cap. This observation supports the conclusion from polar cap contrast data that the haze optical thickness was diminishing during this period.

3. Structure of the Limb

Figure II-3 shows typical limb structure in overlapping narrow- and wide-angle frames. The features shown —a gradual decline in brightness at the limb, a well defined gap, and a thin elevated haze layer—were observed in most frames of the apparent limb, with typical scales of 10 km for the region of brightness decline and 15 km for the gap between the limb and the elevated layer. The scale of this decline suggests that particles scattering there are distributed with the 10-km atmospheric scale height. The narrow-angle pictures taken north of 15°N showed more complex structure, often with several layers and with horizontal variations in the layers, but all narrow-angle limb frames showed some detached layer structure. Locations of these narrow-angle pictures through Rev 35 are shown in Fig. II-4. In addition to the locations shown, four narrow-angle frames showing limb structure were taken south of 65°S. The detached layer shown in Fig. II-3 is brighter in the violet wide-angle frame than in the yellow narrow-angle frame; this is in contrast to the region of brightness decline,

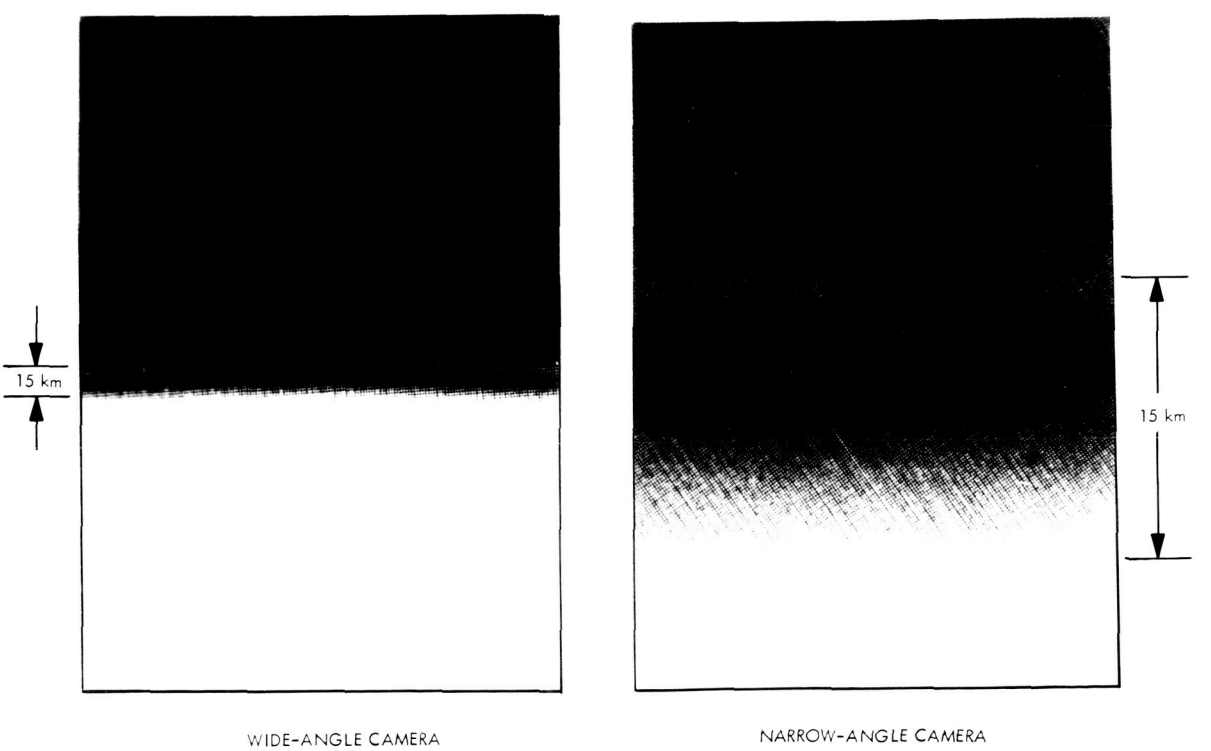

Fig. II-3. Limb views from Rev 16. Wide-angle (violet filter) view on the left (4024-13), and narrow-angle (yellow filter) view on the right (4024-10). Note the detached haze layer about 15 km above the apparent limb of the planet. The limb region is located at 20°S latitude and 102°W longitude.

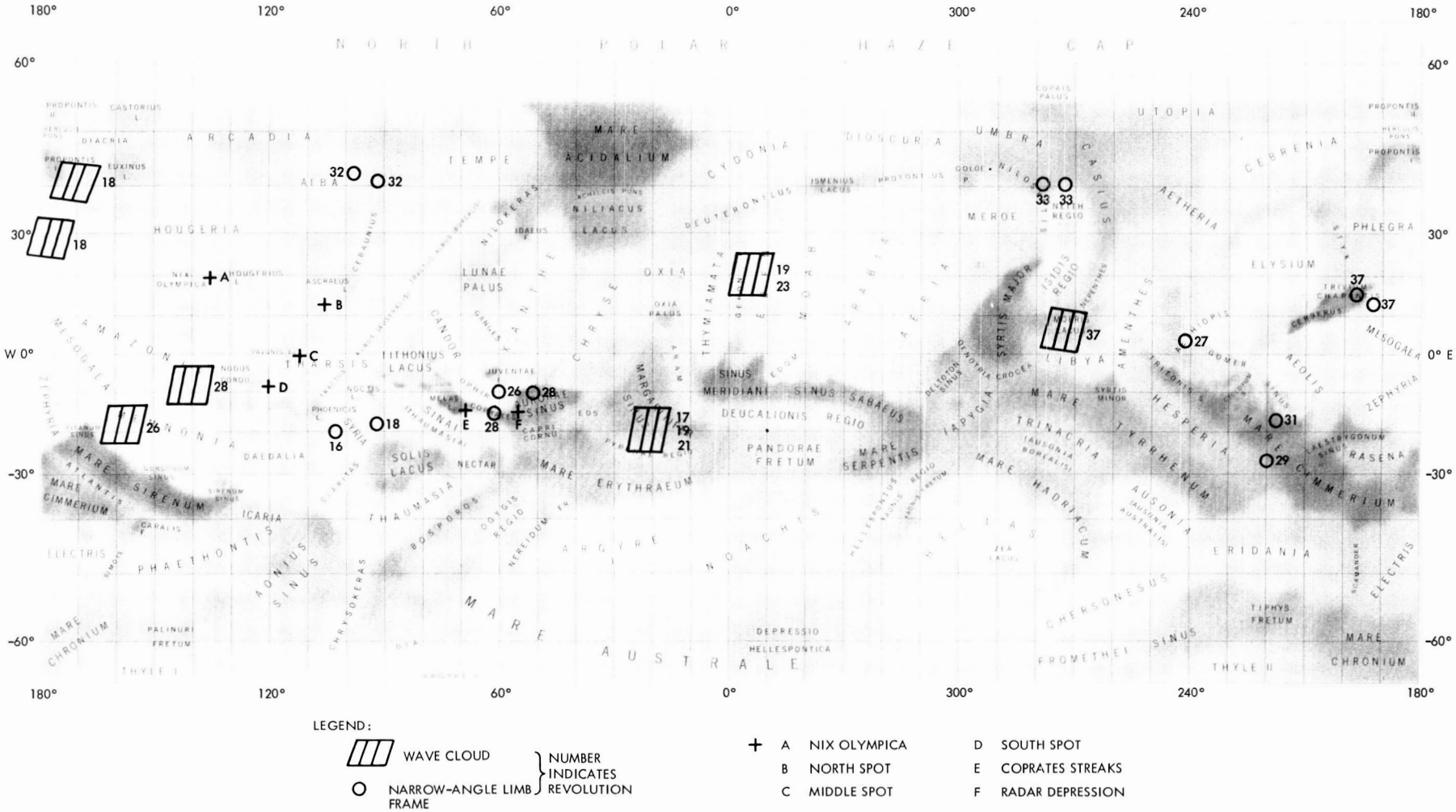

Fig. II-4. Mercator map showing the approximate locations of wave clouds visible in violet and blue frames taken with the wide-angle camera. The lines show the orientation of the wave bands. The circles show the positions of narrow-angle frames on the limb. The numbers located near the lines and circles give the revolution number on which the observation was made. The areographic features, Nix Olympica (A), the three dark spots, (B, C, D), the bright streaks in the Eos-Ophir region (E), and the radar depression near Eos (F), were observed in *Mariner* 9 pictures.

which is distinctly brighter in the yellow frame. A photometric four-color sequence containing the limb near the south polar cap showed the planet and the brightness decline regions to be about as red as the normal Mars, suggesting, along with the 10-km scale, that the lower scatterers are dust particles. The elevated haze was white or slightly blue and is evidently composed of different particles than those scattering in the region of the brightness decline. Thus, it is possible that the high particles are condensates, not dust. Thin elevated haze layers were also visible at, or just beyond, the terminator on the limb (Fig. II-5).

4. Atmospheric Waves

Figure II-6 shows apparent atmospheric wave structure near the terminator just east of Elysium. Several large wave trains (see Fig. II-4) have been seen on the

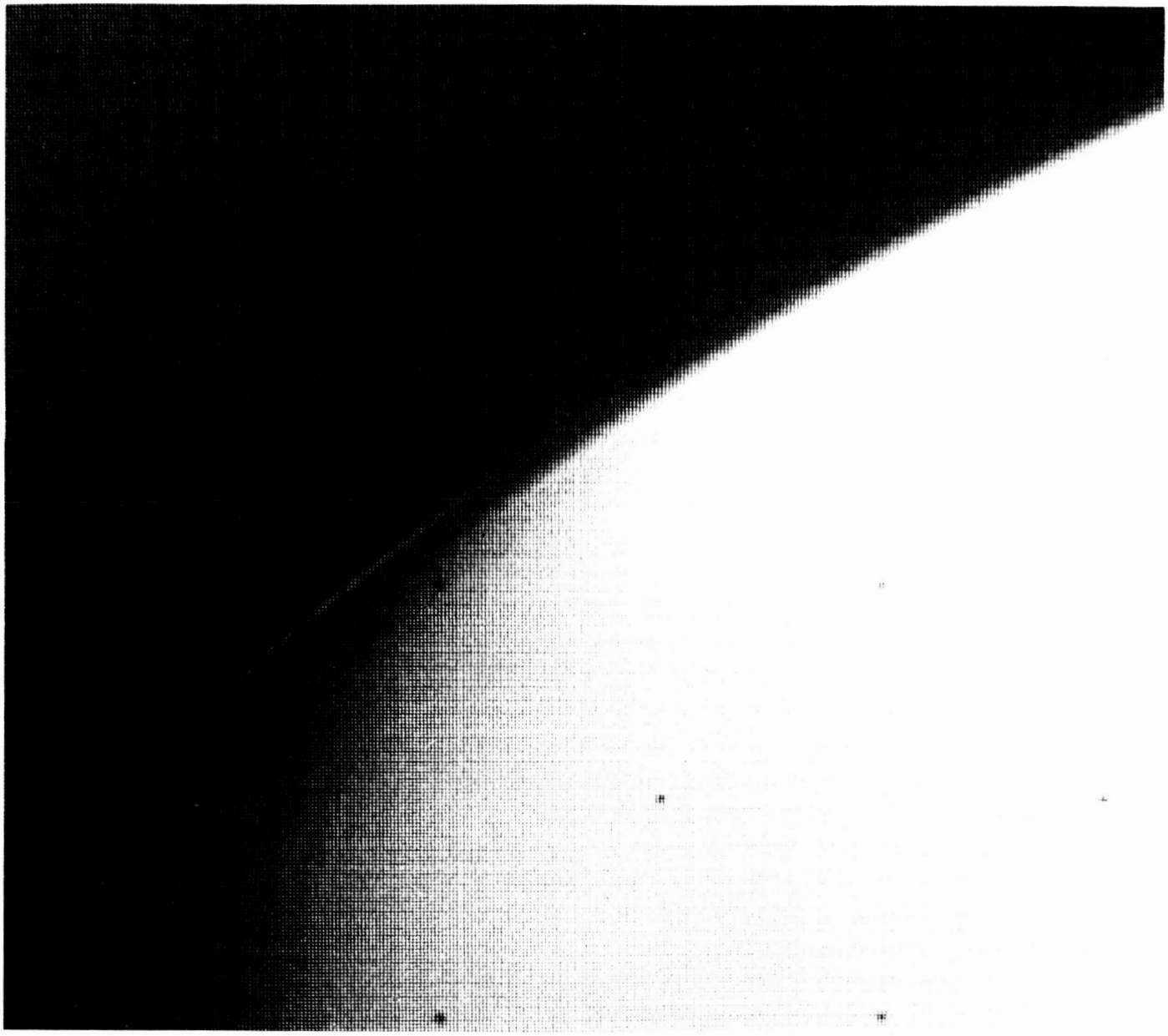

Fig. II-5. Detached haze layer located near the terminator on Rev 29. The haze layer is located at about 30°N latitude, 140°W longitude. The thin layer is about 30 km above the extrapolated apparent limb. The picture was taken by the wide-angle camera (violet filter; 4039-19).

Fig. II-6. Terminator wave clouds in violet wide-angle frame on Rev 18 (Image Processing Laboratory Roll 813, 164208). The wave crests are approximately parallel to the terminator, and the wave length is about 40 km. The location of the waves is shown in Fig. II-4.

terminator in pictures through Rev 50. Typical wave lengths are 40 km. Waves were observed in one blue-filter wide-angle frame; in all other cases, they were observed in violet light. None was apparent in orange frames, even when the overlapping violet frames showed waves in the same region on successive days. The brightness variation across a given wave and the increasing contrast near the terminator (Fig. II-6) suggest relief variations in an atmospheric scattering layer, but the waves also could be made visible by variations in optical properties of the scattering layer. Their visibility in violet but not in orange, together with the crisp detail, suggests that these waves are not seen in the top of the main atmospheric dust layer, but most likely occur in a higher, bluer layer, possibly of condensates. The occurrence of thin, bright clouds near the terminator (Fig. II-5) supports this interpretation. The preferred orientation of the wave crests, parallel to the terminator, is apparently real.

Shorter waves (5 km long) were observed in a few narrow-angle frames (yellow filter), primarily near the terminator. Some features suggestive of waves also were observed in POS narrow-angle frames. The curvilinear streaks that extend nearly 1000 km southwest from South Spot were seen at low, but not at high, Sun angles (cf. Figs. II-1b, 1c, and 1d). During a 90-min period in POS 3, these features exhibited large changes. They may be atmospheric waves in the upper part of the dust layer, controlled by the elevated topography known from Earth-based radar (Ref. II-9) to lie to the east. The wave structure seen in the yellow frames is evidence for some vertical structure in the dust, at least locally.

5. Interpretations

The three aligned dark spots are strikingly located at or near high points in Earth-based radar profiles. Crater floors are brighter objects than their relatively higher surroundings, although no widespread correlation between craters and higher albedos was noted in the 1969 data (Ref. II-10). The long depressions in the Ophir–Melas Lacus region are brighter than their rims. Thus, certain elevated regions (Ref. II-9) are relatively dark, and certain regions that are lower than their surroundings appear bright. The apparent connection between bright and dark areas and elevation differences during this dust storm raises the possibility that some classical seasonal and secular time variations of features have been due to differential obscuration of areas at different elevations (Ref. II-11). In addition, local dust storms could produce local obscuration (Ref. II-12), even when no global dust storm is in evidence.

Systematically better visibility of high areas can be explained if the dust is concentrated in widespread low-level layers through which high terrain protrudes, or because there is less atmosphere above high terrain if the dust is uniformly mixed. There is evidence for both hypotheses. The wide distribution of the surface obscuration and the apparent correlation between brightness and elevation, as well as the scale-height variation of the dust in limb frames, indicate a thorough mixing of the dust. Regional non-uniformities in obscuration are indicated by the relative clarity of the south polar region, the complex structure of northern limbs, and perhaps by the clarity of Nix Olympica, which may violate the altitude-clarity relationship. Radar data do not show this feature to be a particularly high object (Ref. II-9).

The height of features on the limb is not known because the limb of the solid planet cannot be seen. If the dust is well mixed, a height can be inferred. A well mixed dust layer with $\tau = 2$ would not show a brightness decrease on the limb below heights at which the density is about $1/40$ of the surface density. This implies that the lower part of the region of brightness decline is

between 3 and 4 scale heights (30 to 40 km) above the surface. On this basis, the thin detached layer would be near 60 km, at a pressure between 0.1 and 0.01 mb. At least some of the near-terminator wave clouds may occur in this high layer. The nearest terrestrial analogs to a scattering layer in this pressure range are noctilucent clouds, which are sometimes apparent near or beyond the terminator during the summer at high altitudes.

B. Surface Features of the South Polar Region

One objective of the *Mariner 9* television experiment is to monitor the retreating south polar cap and to compare the exposed surface features with their frost-covered appearance recorded by *Mariner 7* in 1969. These observations should provide evidence about the nature and origin of the features and terrain peculiar to the south polar region. Important problems involve the thickness of the CO_2 ice, at present and in the past; the possible presence of other frozen volatiles; the control of frost distribution and thickness by regional topography; and the geologic processes associated with polar phenomena which may have uniquely modified that topography.

C. Geology

At the time of writing, the atmosphere has been clear enough for geologic study of only a few areas, principally those at high elevations, as indicated by radar and occultation data, or at far southern latitudes.

Perhaps the most significant pictures were taken in three of the four dark spots viewed in the pre-insertion sequence. Nix Olympica, North Spot, and South Spot were photographed with high-resolution, narrow-angle-frame tetrads; each proved to contain a crater or crater complex. The Nix Olympica (Fig. II-10a) and North Spot (Fig. II-10b) features are each composed of four or five intersecting craters whose floors lie at different elevations and which appear to have formed successively. The visibility of the terrace edges indicates that the floors are not entirely obscured; the apparent smoothness of the floors may be real, or the floors may be obscured by local dust. The craters are rimless or very low rimmed; sharp edges such as those that surround the majority of lunar craters are strikingly absent. The highest-resolution pictures have been obtained of South Spot, showing features <1 km (Figs. II-10c, 10d).

South Spot is a single, approximately circular structure, about 100 km across, that in its entirety is unlike any known terrestrial or lunar crater, or any Martian craters observed on previous *Mariner* missions. The crater does resemble some large lunar craters in having a flat floor and completely terraced walls; it is distinctive in that a zone with a smooth surface broken into arcuate horsts and grabens concentric with the crater immediately surrounds the rim. Fresh, large lunar craters typically have coarse, hummocky topography immediately outside the rim crest which grades outward into radial ridges and grooves with low relief. Here the hummocky facies is absent and a radial pattern is visible only beyond one crater radius from the edge of the crater. The elements in this zone are short and lobate, unlike the narrow, gradually tapering ridges radial to lunar craters. On the rim are several small (1 to 5 km) rimless craters, some of which appear to form arcuate chains. Major valleys extend to the northeast and southwest of the main crater (perhaps more than coincidentally the direction of the North Spot–Middle Spot–South Spot alignment). These valleys consist of many coalescing irregular craterlets and sinuous or linear grooves, and are another feature not closely matched in terrestrial or lunar craters.

Owing partly to the high intrinsic contrast between the cap and adjacent ground, it has been possible to monitor frost distribution from *Mariner 9* throughout the dust storm. Correlation with the *Mariner 7* pictures shows that the residual cap lies within the region of peculiar curvilinear features previously seen (Ref. II-13) near the south pole. Figure II-7 shows the south polar cap as viewed by *Mariner 7* late in the Martian southern winter, and by *Mariner 9* during the Martian southern summer. The planimetric similarity of the curvilinear patterns in both the 1969 and 1971 views is evident. However, in the 1969 picture, the streaks are bright, being highlighted by frost, whereas they are dark in the *Mariner 9* pictures. It is now evident that these curvilinear patterns are permanent topographic forms that control the outline of the residual cap as it retreats. It was observed in 1969 that local topography, principally craters, strongly controlled the detailed form of the margin of the retreating cap near 60°S latitude. Parts of the boundary and interior of the retreating cap, as observed in the *Mariner 9* pictures, are remarkably regular and uniform. Those places, therefore, appear to contain few craters. The topography seems limited primarily to curvilinear ridges and/or troughs, perhaps of highly subdued character.

Figure II-8 presents selected high-resolution pictures to show the variety of patterns displayed in the subliming cap. The low-resolution view gives the impression of a roughly circular pattern of conformal curvilinear features; the high-resolution images show a much more

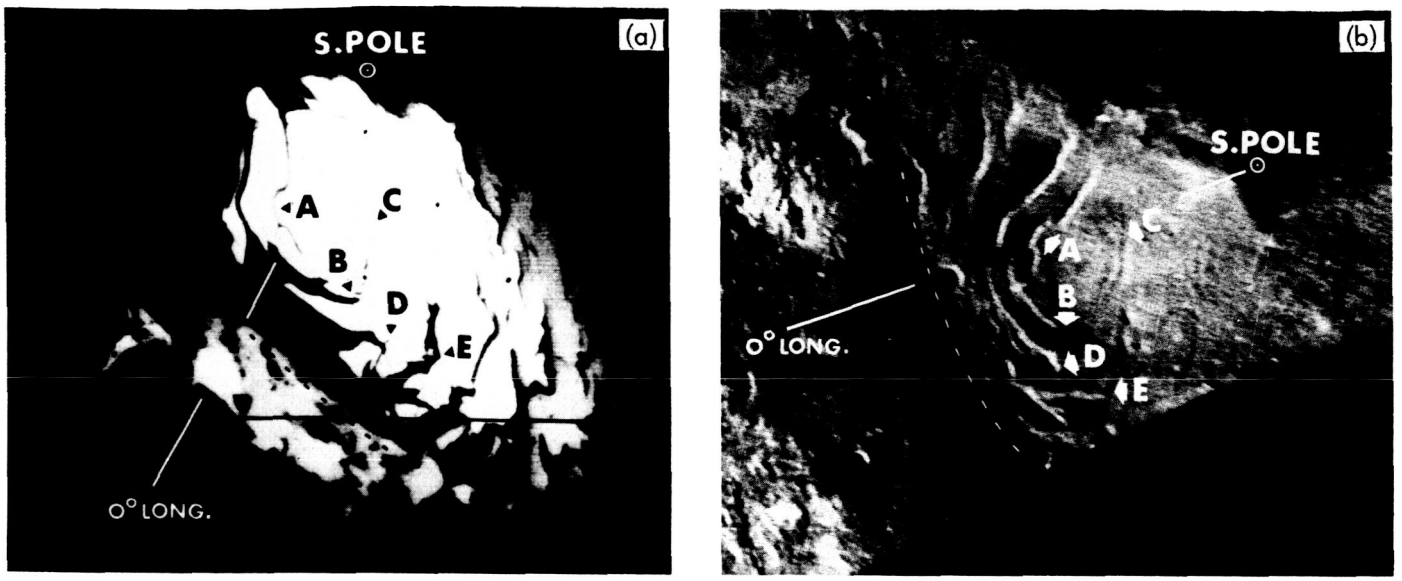

Fig. II-7. (a) *Mariner* 9 (4019-25) and (b) *Mariner* 7 (7N17) views of the south polar cap. Correlation of dark markings in *Mariner* 9 wide-angle view of cap with light markings on narrow-angle frame from *Mariner* 7. The *Mariner* 7 image has been rectified and then enhanced. Although this version shows strong contrast, the entire area actually was covered by frost.

irregular pattern, although the individual dark streaks are quite uniform in width. One ring-shaped feature, probably a frost-free crater rim (see Fig. II-8b), suggests that positive relief may have defrosted there more rapidly than in adjacent areas. If this relationship is general, a complex of low relief ridges would seem the most likely explanation of the curvilinear streaks. However, shallow scarps or troughs cannot be excluded by the available data.

The two wide-angle frames in Fig. II-9 show a significant disappearance of frost between Revs 11 and 44 (a 16.5-day interval). Two high-resolution views in Fig. II-9 show details of the disappearance over an 11.5-day interval. As only a few centimeters of solid CO_2 could possibly sublime in this time, a very thin deposit covering a surface of extremely low relief is indicated in the areas that are clearing. It is still possible that thicker deposits exist elsewhere in the residual cap. The high-resolution frame acquired on Rev 34 suggests topographic control of the sublimation along small, shallow, irregular curvilinear features paralleling the main dark band.

At present, there is no way to determine if the unusual topography now recognized at the site of the residual south polar cap is in some way related to thick ice deposits, past or present. Continued monitoring to record changes of detail combined with quantitative processing and manipulation of all relevant picture data may permit at least some intelligent speculations as to the history of this unique portion of the Martian surface.

The morphology of the craters in the three spots indicates subsidence. The most prominent, large subsidence features on Earth are volcanic calderas, caused by withdrawal of magma, principally by eruption (Ref. II-14). Some calderas lie on the summits of broad volcanic shields and are accompanied by rimless pit craters on the upper flanks and lava flows on the lower slopes and show multiple arcuate faults similar to those of South Spot, though rarely as well developed. The largest terrestrial calderas are irregular, multiple structures with outlines and dimensions comparable to those of the Nix Olympica and North Spot features. A single, symmetrical caldera as large as the South Spot feature would, however, be extraordinary on the Earth. An alternative hypothesis, that these craters are solely of impact origin, is difficult to reconcile with the absence of walls between the component craters, the different levels of their floors in Nix Olympica and North Spot, and with the lack of markedly elevated rims and hummocky rim deposits. Nevertheless, the continuing debate on the origin of many craters on the Moon, where atmospheric processes neither cause surface modification nor degrade the viewing, indicates the advisability of caution in this preliminary interpretation, particularly because what has been seen may be

Fig. II-8. Details of the south polar cap. Various patterns in the subliming frost cap are recorded in the five narrow-angle frames. Locations are indexed in the accompanying wide-angle frame. The maximum dimension of the narrow-angle frames is about 100 km on the surface of Mars. Frames A (4056-65) and E (4056-62) are from Rev 46, C (4045-71) and D (4048-65) from Rev 38, and B (4033-45) from Rev 25. The wide-angle frame (4056-65) is from Rev 46; a residual image of the polar cap is faintly visible, displaced toward the upper-right corner.

Fig. II-9. *Mariner* 9 pictures displaying the gradual disappearance of the residual polar cap. The top two images are *Mariner* 9 wide-angle pictures of the polar cap acquired about 9 days apart on Revs 11 (left) and 29 (right) (Image Processing Laboratory Roll 805; Roll 853, 045715). These two images have been rectified to a polar stereographic projection. The relative distortion between the two projections is due to uncertainties in the preliminary pointing data. The cap is about 450 km in diameter in the earlier image. White arrows indicate common areas which have suffered significant defrosting over the 9-day period. A residual image of the cap can be seen to the right of the cap, in the left-hand picture. The bottom two images are *Mariner* 9 narrow-angle frames from Revs 11 (left) and 34 (right) showing changes in the cap over 11½ days (4044-62, 4019-28). The area of the narrow-angle frames is indicated by black arrows in the wide-angle frames. Certain fine details can be seen in both images, showing that the difference in the appearance is real and not resulting solely from varying obscuration. Detailed patterns parallel to the main frost-free corridor are emerging in the later version.

only small parts of large structures. The fact that these features are elevated to a level of visibility when the rest of the planet is obscured suggests that they may not be typical of Mars as a whole. If the sharpness of the features and the smoothness of the surrounding terrain is not an effect of the conditions of viewing or image processing, these spots may be geologically young features, compared with the heavily cratered areas observed in 1969 (Ref. II-15).

As the dust cleared elsewhere, some terrain became visible which exhibits more linear structural patterns than recognized in the 1969 pictures. For example, west of Solis Lacus the surface is broken by irregular, subparallel scarps (Fig. II-11). The pattern is suggestive of terrestrial block faulting; its true nature may become more apparent as broader areas become visible.

A pattern of light streaks in the region from Eos to Ophir, observed continuously since the POS sequences, is shown in Fig. II-12. The brightest knot corresponds to a bright yellow cloud first viewed in Earth-based photographs on September 27 and 28, only a few days after the 1971 dust storm began; a similar cloud was seen in the same location during the 1956 dust storm (Fig. II-12a). Radar data show that in this region the dark areas (e.g., Aurorae Sinus) stand high, while the bright regions are lower. The bright knot lies near a deep depression, 6 km lower than the mean terrain. (Fig. II-12b; Fig. II-4, point F). Comparison of 1971 and 1969 *Mariner* pictures reveals that the bright markings obscure the normally visible dark markings in the region (Figs. II-12c, 12d). These data suggest that the marking is an effect produced by a greater amount of dust in or above a system of valleys. It is not clear whether the cloud is a true concentration of dust or merely an apparent effect of increased path length through a more uniformly dust-laden atmosphere. Figure II-12e shows a narrow-angle tetrad of part of the streak, indicating scalloped, sharp boundaries. Figure II-12f shows that the east end of the cloud complex lies in the valley system containing the chaotic terrain discovered in 1969.

Fig. II-10. Narrow-angle views of craters in the dark spots, rectified on the basis of preliminary orbital data. (a) Crater complex in Nix Olympica. Arcuate scarps continuous with the scallops on the wall indicate that the floor is not fully obscured. Smaller craters to the east and south may be superposed, unrelated features (Image Processing Laboratory Roll 882, 025127). (b) Crater complex of North Spot. The central crater with terraced walls apparently truncates several subsidiary craters (Image Processing Laboratory Roll 882, 030159). (c) The South Spot crater photographed on Rev 28 (Image Processing Laboratory Roll 882, 022534 and 023951). A concentrically fractured zone extends about one crater radius out from the crater edge; the surface beyond has a complex subradial texture. Several rimless craters in the smooth zone appear to be aligned along the arcuate fractures. Troughs composed of numerous coalescing craterlets and grooves extend to the NNE and SSW of the main crater. Small rimmed craters to the west may be impact craters unrelated to the regional structure. (d) South Spot viewed on Rev 32, 48 hours after the previous view (Image Processing Laboratory Roll 882, 033019 and 033901). Differences are due either to real changes in the dust cloud, or in the lighting and view paths through the dust. The disappearance of the radial facies on the northwest rim suggests that other apparently smooth areas, such as the crater floor, actually may be concealed as atmospheric dust.

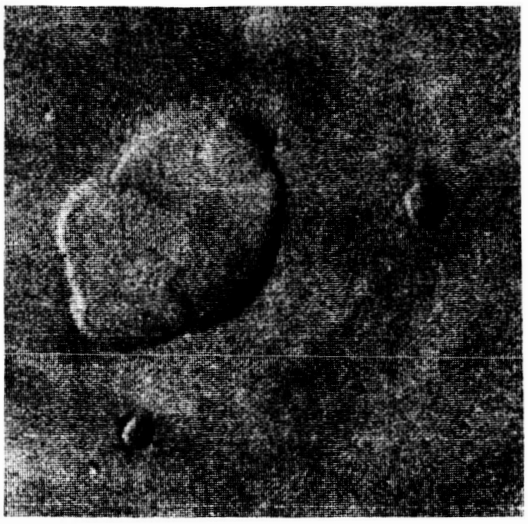

(a)

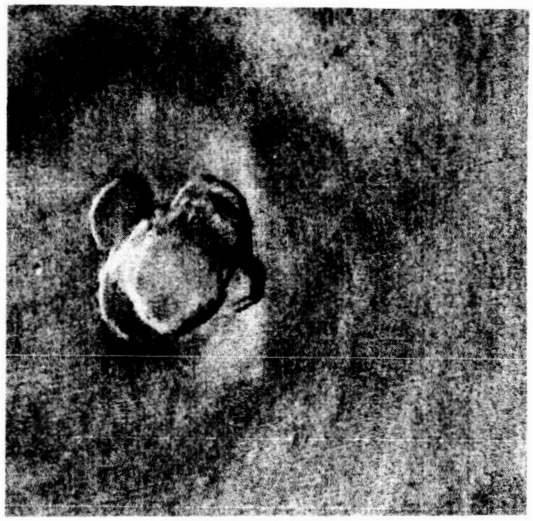

(b)

(c)

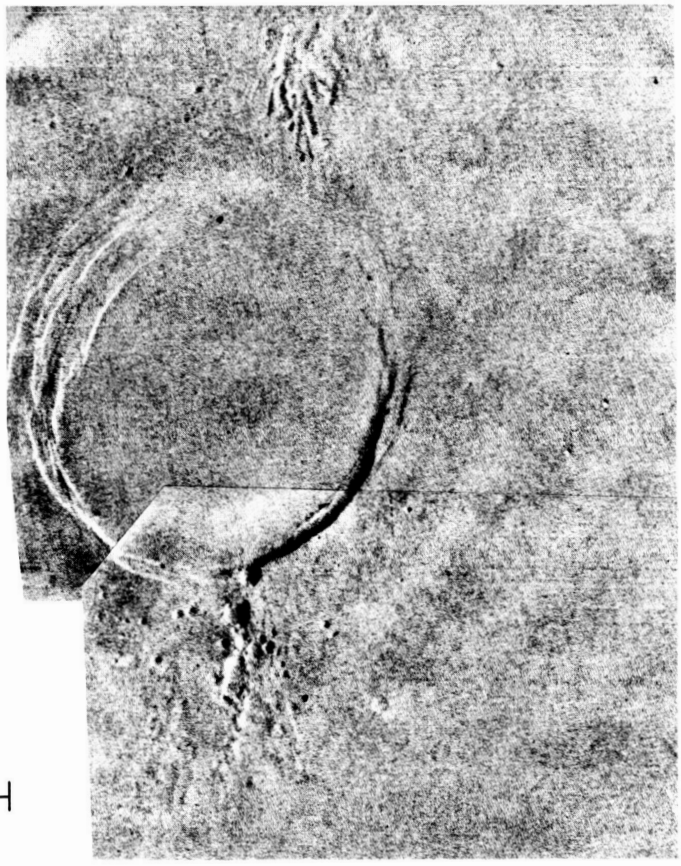

(d)

50 km

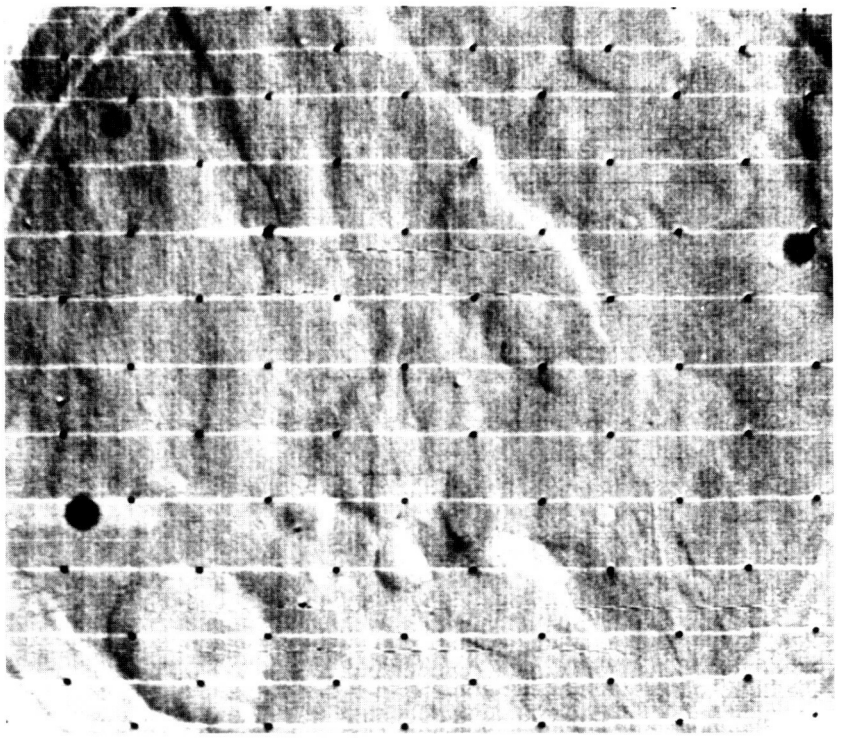

Fig. II-11. Narrow-angle picture from Rev 42 showing linear scarps, possibly a product of block faulting, west of Solis Lacus. As in almost all *Mariner* 9 pictures, crater floors appear featureless. The three dark circular spots are shadows of dust specks on the vidicon faceplate (4055-75).

Fig. II-12. Evidence of topographic control of atmospheric features. (a) The *Aurorae Sinus* region (center) displayed a discrete bright cloud during the 1956 dust storm. A similar discrete cloud appeared over Eos during the early stages of the 1971 dust storm (Ref. II-1). (b) Radar elevation contours (in kilometers) in the Eos region show that the brightest knot in the cloud lies near the deepest depression. The area shown corresponds with Figs. II-12c, 12d. (c) Eos-Ophir cloud complex as observed by *Mariner* 9 during POS 3 on November 13. Background is entirely obscured by atmospheric dust. The arcs are residual images of the limb from previous frames. The area shown corresponds with the box in Fig. II-12a (Image Processing Laboratory Roll 529, 252424). (d) Rectified *Mariner* 7 photo-map of the same region as (c), showing the normally visible dark markings. (e) Narrow-angle mosaic of the western part of the cloud, showing sharp boundaries, photographed on December 2. Some surface detail can be seen outside the cloud boundaries. The area shown corresponds with the left-hand box in Fig. II-12c (Image Processing Laboratory Roll 905: 201-449, 202-414, 203-341, 204-508). (f) *Mariner* 7 frame (6N7) showing scarp-bounded valleys that delimit the eastern end of the cloud in the Eos region. These valleys contain the chaotic terrain discovered in 1969. The area shown corresponds with the right-hand box in Fig. II-12c and the box in Fig. II-12d.

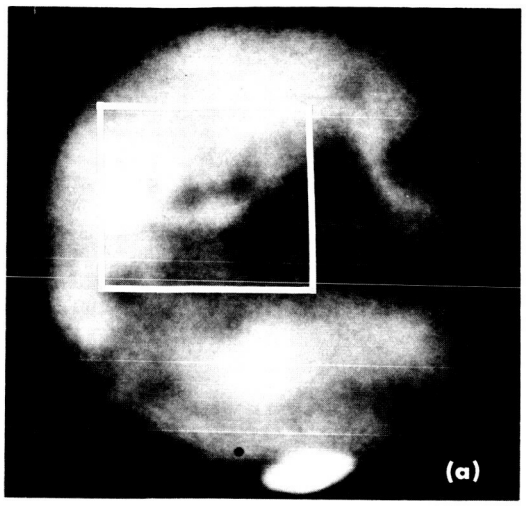
(a)

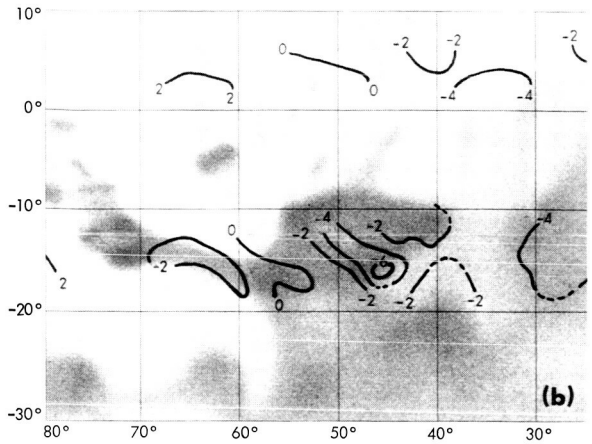
10°
0°
-10°
-20°
-30°
80°
70°
60°
50°
40°
30°
(b)

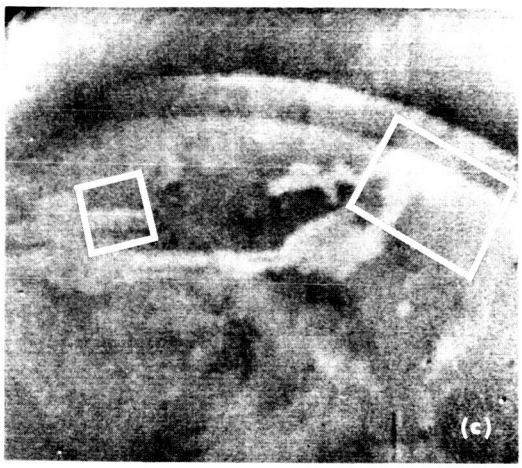
(c)

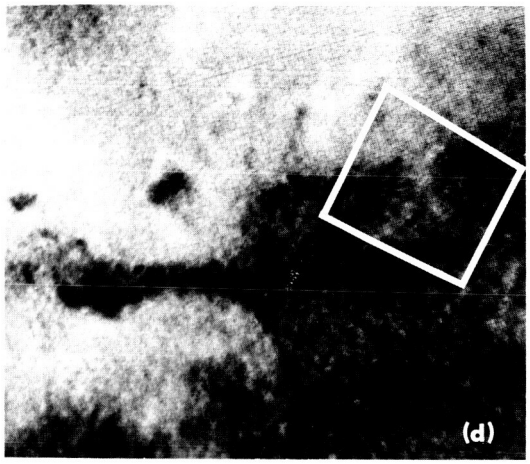
(d)

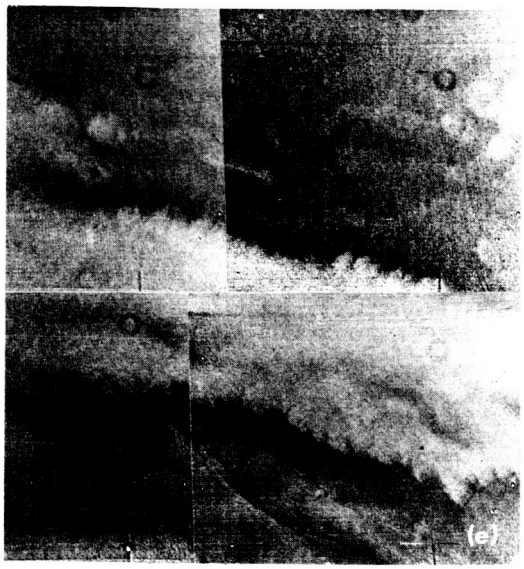
(e)

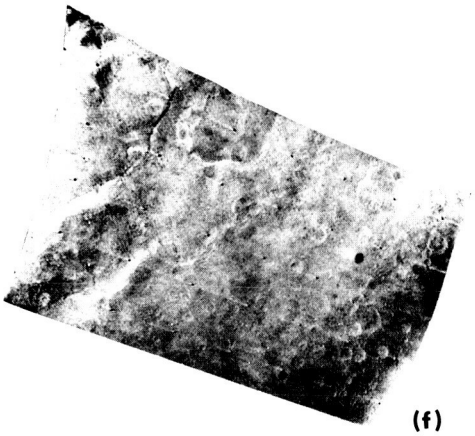
(f)

As in 1969, the south polar region presented features of types not seen in lower latitudes. One of the more notable of these is a field of sinuous markings trending approximately north–south (Fig. II-13). The identity of the pattern in views taken days apart shows that they are fixed features and not cloud or dust billows. One feature extends without deflection over what appears to be the rim of a crater, suggesting that they have been produced by material transported over the surface with only slight control by underlying topography.

D. Satellite Astronomy

Pictures of the Martian satellites, Phobos and Deimos, obtained during POS sequences and from orbit, have provided new information about the satellites' orbits, shapes, sizes, albedos, and surface morphologies. To photograph Phobos and Deimos at close range, it was necessary to obtain improved orbits. The first corrections to orbital data were based on 21 pictures taken during the POS sequences that contain Phobos or Deimos together with stars. The ephemerides are being improved by incorporating pictures taken in orbit. A first-order analytic theory including zonal harmonics up to fourth order is used to model the motion of Phobos and Deimos (Ref. II-16). Initial conditions were obtained by fitting data obtained from Wilkins' theory (Ref. II-17). After processing the television data up to November 28, the position of Deimos was determined with a standard deviation of 20 km. With only five Phobos pictures, its position was obtained only to 100 km. Corrections to the mean orbital elements indicate that Phobos is about 2° ahead of its expected mean anomaly, while Deimos is about 1° behind. The inclinations of the orbital planes of Phobos and Deimos relative to the Earth's equatorial plane differ by 0.5° from those expected.

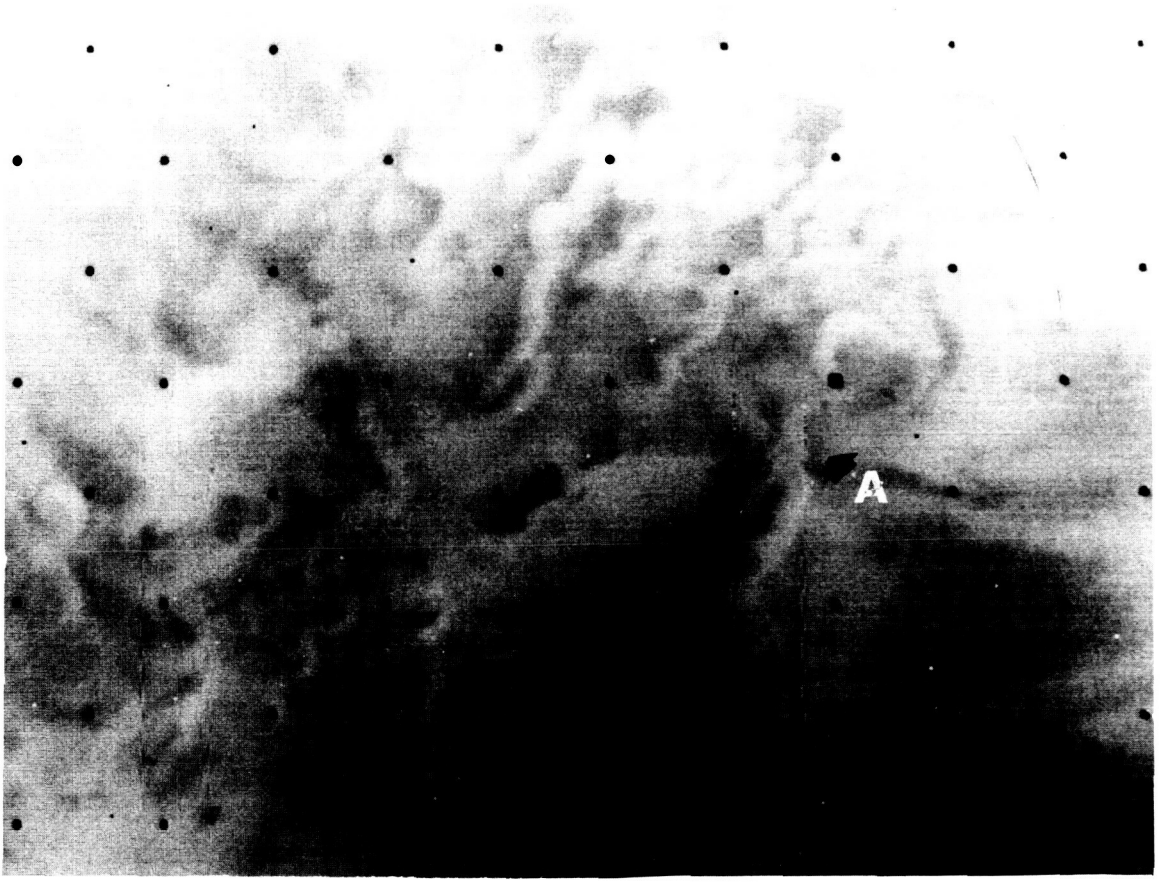

Fig. II-13. Field of sinuous features near the south pole. One feature apparently transects the rim of the crater (A) suggesting that they were formed by superficial processes. Wide-angle picture from Rev 16 (4024-20).

Figures II-14 and II-15 show the first close-up views ever obtained of these satellites. Both are irregular in shape, as expected for bodies too small for their gravitational fields to impose a spherical shape. The bottom side of Deimos displays an interesting indentation. Similarly, an indentation appears on the right side of Phobos in Fig. II-15b. Phobos is estimated to be 25 ± 5 km long (east–west), 21 ± 1 km wide (north–south); Deimos is 13.5 ± 2 km long, 12.0 ± 0.5 km wide. The nominal values are based upon the correction appropriate for a spherical object viewed at the observed phase angle. The larger error bars for the length measurements reflect the uncertainty in allowing for the unilluminated portions of the body.

Combining the above dimensions with Kuiper's Earth-based visual magnitude observations of the satellites (Ref. II-18), a geometric albedo of 0.05 has been inferred for both satellites, with a formal uncertainty of about 25%. Such a low albedo puts these two satellites among the darkest objects in the solar system, equivalent to the darkest parts of the lunar maria.

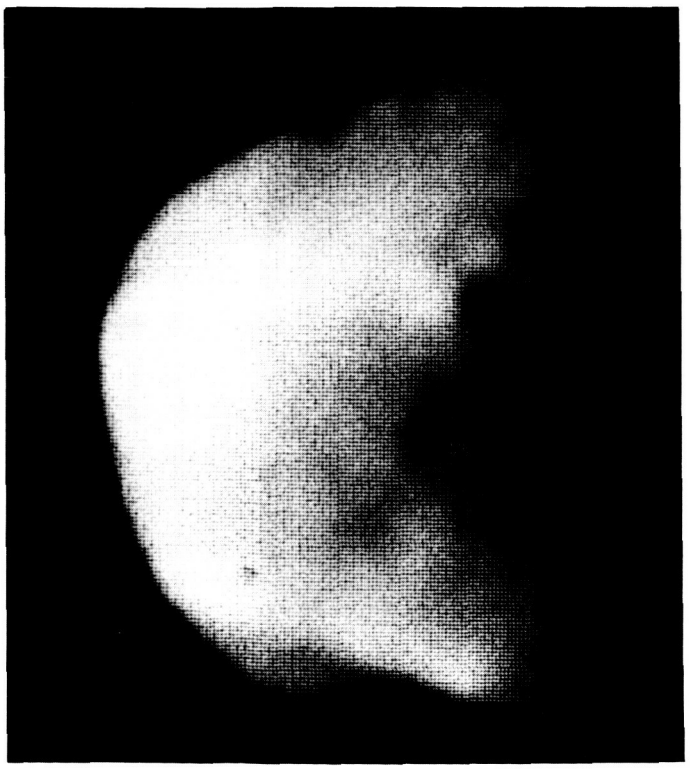

Fig. II-14. Computer-enhanced picture of Deimos obtained on Rev 25 at a distance of 8830 km and a phase angle of 68° (Image Processing Laboratory Roll 752, 144007).

The picture of Deimos (Fig. II-14) reveals two clear crater-like depressions near the terminator and a third dusky spot, which may be a crater. These craters are about 1.4 km in diameter. The topography of the two most clearly defined craters can be inferred from a study of the brightness pattern near and in the craters. Figure II-16 shows a brightness profile through each crater in the direction from the limb to the terminator. The ordinate is a monotonic function of brightness, but not necessarily linear, as the pictures have not been photometrically decalibrated. To cancel partially the falloff of light toward the terminator, the data were normalized to the values on a parallel line across the smooth surface between the two craters. The shadowed, depressed interior for each crater is shown, and each crater has a bright outer rim on the terminator side. The presence of an outer rim is consistent with an impact origin for the craters. In the negligible gravity field of the satellites, little of the fragmental ejecta would settle near the crater, so that the rims correspond to the raised bedrock rims of terrestrial craters. These rims indicate some degree of plastic response. A more brittle response, which could depend upon the velocity of impact as well as the material of the satellite, would cause spalling of the outer shells of the satellite over a broad zone around the crater, around the antipodal point, and possibly over the entire surface (Ref. II-19). While extensive spalling is not evident, some of the angular irregularities may have originated through such a process.

Many craters also appear on the pictures of Phobos. Particularly striking is the 5.3-km crater near the bottom (south pole) on Fig. II-15a and near the center on Fig. II-15b. The impact that produced this crater is close to the largest impact Phobos could have sustained without fracture and disruption.

Preliminary measurements indicate that the crater density on the two satellites is within about a factor of three of that necessary to saturate the surface with craters. On the surface of Mars itself, the density of similar sized craters is about two orders of magnitude less. Thus, Phobos and Deimos serve as "control surfaces" for Mars, and indicate that substantial erosive processes have acted to remove ancient Martian craters. Phobos and Deimos can be regarded as old, relative to the age of kilometer-scale Martian surface structures.

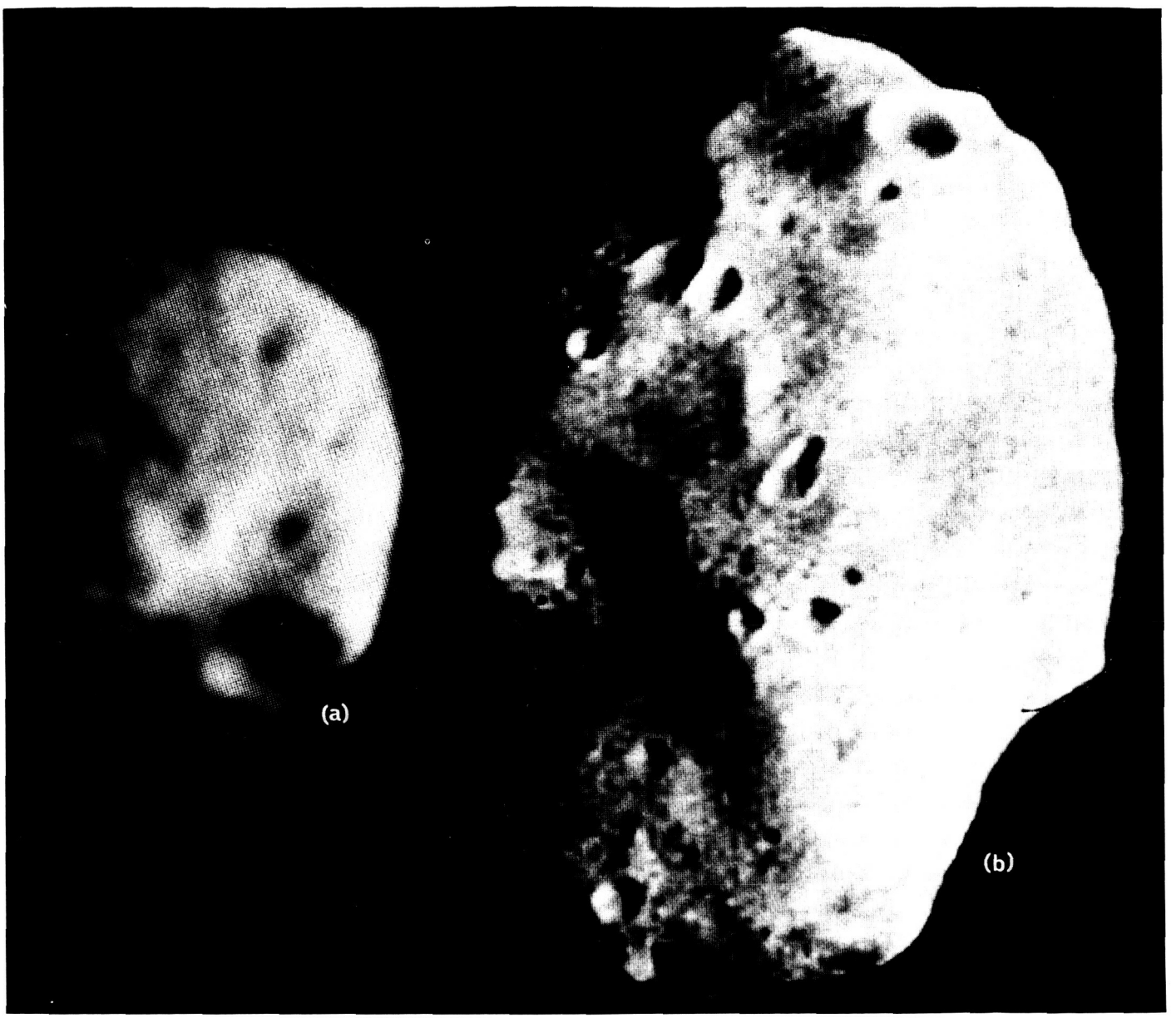

Fig. II-15. Computer-enhanced pictures of Phobos. (a) View obtained on Rev 31 at a distance of 14,440 km and a phase angle of 77° (Image Processing Laboratory Roll 792, 220312). (b) View obtained on Rev 34 at a distance of 5550 km and a phase angle of 56° (Image Processing Laboratory Roll 820, 002025).

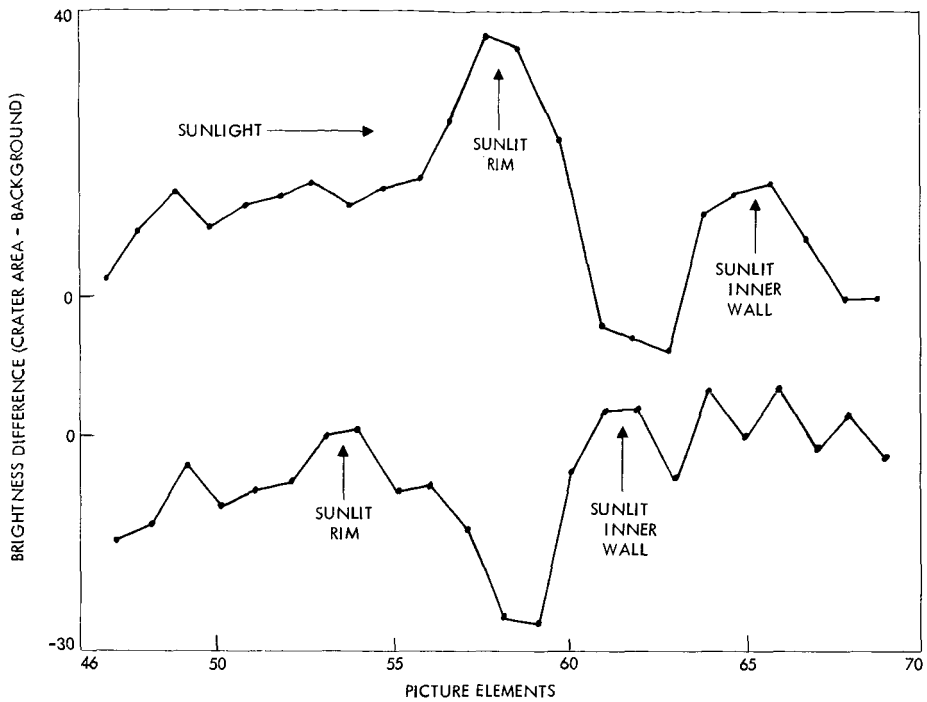

Fig. II-16. Brightness traces across the two prominent craters on Deimos (see Fig. II-14). From left to right, the trace progresses from near the sunlight limb to near the terminator. The ordinate is the difference in brightness between a trace across one of the craters and that across an uncratered part of Deimos. The image used to obtain the brightness values was not photometrically decalibrated.

References

II-1. Kirby, T. B., and Robinson, J. C., *Sky and Telescope,* Vol. 42, p. 264, 1971.

II-2. Pettit, E., and Richardson, R. S., *Publ. Astron. Soc. Pacific,* Vol. 67, p. 62, 1955.

II-3. Masursky, H., Batson, R., Borgeson, W., Carr, M., McCauley, J., Milton, D., Wildey, R., Wilhelms, D., Murray, B., Horowitz, N., Leighton, R., Sharp, R., Thompson, W., Briggs, G., Chandeysson, P., Shipley, E., Sagan, C., Pollack, J., Lederberg, J., Levinthal, E., Hartmann, W., McCord, T., Smith, B., Davies, M., de Vaucouleurs, G., and Leovy, C., *Icarus,* Vol. 12, p. 10, 1970.

II-4. Mikhailov, A. A., in *The Moon,* Z. Kopal and Z. K. Mikhailov, Ed., Academic Press, New York, 1962.

II-5. Young, A. T., *Icarus,* Vol. 11, p. 1, 1969.

II-6. Antoniadi, E. M., *La Planete Mars 1659–1929,* Librarie Scientifique Hermann et Cie, Paris, 1930.

References (contd)

II-7. Slipher, E. C., *The Photographic Story of Mars*, p. 142, Northland Press, Flagstaff, Arizona, 1962.

II-8. Van Blerkom, D. J., *Icarus*, Vol. 14, p. 235, 1971.

II-9. Pettengill, G. H., Counselman, C. C., Rainville, L. P., and Shapiro, I. I., *Astron. J.*, Vol. 74, p. 461, 1969. Rogers, A. E. E., Ash, M. E., Counselman, C. C., Shapiro, I. I., and Pettengill, G. H., *Radio Science*, Vol. 5, p. 465, 1970. Goldstein, R. M., Melbourne, W. G., Morris, G. A., Downs, G. S., and O'Handley, D. A., *Radio Science*, Vol. 5, p. 475, 1970. Pettengill, G. H., Rogers, A. E. E., and Shapiro, I. I., *Science*, Vol. 174, p. 1321, 1971. Downs, G. S., Goldstein, R. M., Green, R. R., and Morris, G. A., *Science*, Vol. 174, p. 1324, 1971.

II-10. Cutts, J. A., Soderblom, L. A., Sharp, R. P., Smith, B. A., and Murray, B. C., *J. Geophys. Res.*, Vol. 76, p. 343, 1971.

II-11. Sagan, C., and Pollack, J. B., *Nature*, Vol. 223, p. 791, 1969.

II-12. Sagan, C., Veverka, J., and Gierasch, P., *Icarus*, Vol. 15, p. 253, 1971. Gierasch, P., and Sagan, C., *Icarus*, Vol. 14, p. 312, 1971.

II-13. Sharp, R. P., Murray, B. C., Leighton, R. B., Soderblom, L. A., and Cutts, J. A., *J. Geophys. Res.*, Vol 76, p. 357, 1971.

II-14. Williams, H., *Calderas and Their Origins*, Vol. 25, p. 239, Bull. Dept. Geological Sciences, University of California, 1941.

II-15. Murray, B. C., Soderblom, L. A., and Cutts, J. A., *J. Geophys. Res.*, Vol. 76, p. 313, 1971.

II-16. Aksnes, K., *On the Use of Hill Variables in Satellite Theory*, 8th Annual Seminar on Problems in Celestial Mechanics, University of Texas, Austin, 1970.

II-17. Wilkins, G. A., in *Mantles of the Earth and Terrestrial Planets*, p. 77, NATO Advanced Study Institute, University of Newcastle upon Tyne, 1966; Interscience Publishers, London, 1967.

II-18. Harris, D. L., in *Planets and Satellites*, p. 289, G. P. Kuiper and B. M. Middlehurst, Ed., University of Chicago Press, 1961.

II-19. Gault, D. E., and Wedekind, J. A., *J. Geophys. Res.*, Vol. 74, p. 6780, 1969.

Acknowledgment

Appreciation is extended to E. M. Shoemaker and A. P. Ingersoll for reviewing the manuscript; and to R. Tyner and S. Reed for mosaicking pictures during mission operations.

III. Infrared Spectroscopy Experiment

R. A. Hanel, B. J. Conrath, W. A. Hovis, V. G. Kunde, P. D. Lowman, J. C. Pearl, C. Prabhakara, and B. Schlachman
Goddard Space Flight Center, Greenbelt, Maryland

G. V. Levin
Biospherics Incorporated, Rockville, Maryland

The infrared spectroscopy experiment on *Mariner 9* was designed to provide information on atmospheric and surface properties by recording a major portion of the thermal emission spectrum of Mars. The original intent was to derive vertical temperature profiles, surface temperature, atmospheric pressure at the surface, and information related to the surface composition. The experiment also was to search for minor atmospheric constituents, including water vapor and isotopic components of carbon dioxide (Ref. III-1). The biological implications of the Martian environment were to be studied. Although the Martian dust storm has complicated the task of attaining the scientific objectives originally formulated for a dust-free atmosphere, unexpected information may be obtained on the dust composition and on the general circulation associated with the storm.

The Michelson infrared interferometer spectrometer (IRIS-M) records the spectral interval from 200 cm^{-1} (50 μm) to about 2000 cm^{-1} (5 μm) with a nominal spectral resolution of 2.4 cm^{-1} in the apodized mode of data reduction. A noise equivalent radiance of about 5×10^{-8} W cm^{-2} $sterad^{-1}/cm^{-1}$ has been achieved. The field of view is almost circular with a half cone angle of 2.25°. Wave number calibration is provided by a fringe control interferometer that uses the 0.6929-μm line of a neon discharge source as a standard. Intensity calibration is achieved by scaling Martian spectra to calibration spectra recorded periodically while observing alternately deep space and a 296.4 K on-board blackbody. After Fourier transformation and scaling of the raw spectra in an Earth-based digital computer, the individual calibrated spectra are displayed in absolute radiometric units as a function of wave number.

On a planetary scale, the Martian spectra obtained so far exhibit a fair degree of uniformity in comparison with similar spectra obtained from the *Nimbus* satellites

for the Earth (Ref. III-2). The major exception in the appearance of the Martian spectra occurs in the vicinity of the south polar cap. Examples of non-polar and polar spectra are shown in Figs. III-1a and 1b, respectively.

Major features common to all spectra are the two broad regions at 400 to 600 cm^{-1} and 850 to 1250 cm^{-1} which appear in absorption in the non-polar spectra and in emission in the polar spectra; and the molecular absorption by CO_2 in the range of 540 to 800 cm^{-1}. The difference in appearance of the spectra may be qualitatively ascribed to differences in the atmospheric temperature profile, the underlying lower boundary surface, and the amount of dust in the atmosphere. In most of the non-polar spectra, all of the molecular bands of CO_2 appear in absorption, indicating that the atmospheric temperatures decrease with height on a gross scale. In the polar spectra, the parts of the spectrum from 550 to 625 cm^{-1} and 700 to 800 cm^{-1} appear in emission, indicating that the lower atmospheric region in which this radiation originates is at a warmer temperature than the underlying surface.

The most striking result of the experiment thus far is the strong effect of the atmospheric dust on the emission spectra. The entire spectrum, with the exception of the strongly absorbing part of the 667-cm^{-1} (15-μm) CO_2 molecular band, apparently is influenced to varying degrees by the opacity of the dust in the atmosphere. A rigorous treatment of spectra from a dust-laden atmosphere must be based on a radiative transfer model which incorporates absorption and scattering by the dust along with molecular CO_2 absorption. Until that can be accomplished, more simplified methods must suffice.

The diffuse features appearing near the 470- and 1075-cm^{-1} absorption in non-polar and emission in polar spectra are attributed to dust particles in the atmosphere. The features are characteristic of the SiO_2 bands in silicate-bearing minerals. Lyon (Ref. III-3), Hovis (Ref. III-4). Aronson, et al. (Ref. III-5), Conel (Ref. III-6), and Salisbury, et al. (Ref. III-7) have shown that the spectral position of absorption and reflection peaks depends on the silica content; acidic minerals (70 to 75% SiO_2) suspended in powder form absorb most strongly at 1100 cm^{-1}, while ultra-basic materials (less than 45% SiO_2) show absorption peaks near 950 cm^{-1}. A preliminary comparison of the emission features measured over the south polar region with the absorption spectra of fine dust measured by Lyon shows generally good agreement with minerals and rocks whose SiO_2 content is in the intermediate range (55 to 65%), but poor agreement with highly acidic (greater than 65%) as well as basic (45 to 55%) and ultra-basic (less than 45%) material. Silicates are also indicated in non-polar areas. If this result is substantiated by continuing analysis (additional laboratory measurements of emission and absorption spectra of various dust samples, radiative transfer calculations for a scattering and absorbing atmosphere, analysis of additional spectra), its implications are of great planetological significance.

There is at this time no agreement on whether Mars is differentiated (e.g., Ref. III-8). The SiO_2 content of planetary surfaces is probably the best gross geochemical indicator of the degree of differentiation. Thus, the relatively high SiO_2 content indicated by these preliminary results, if representative of the Martian surface, would show that Mars has undergone at least as much differentiation as the Moon (Ref. III-9), and perhaps as much as the Earth. The above discussion assumes that the suspended dust has the same bulk composition as the surface rocks. This assumption is based on the probable absence of extensive chemical weathering on Mars.

The fact that the silicate features associated with the dust appear in emission in the polar spectra confirm that the absorption is produced by dust suspended in the atmosphere rather than the surface itself. The strength of the dust features in the spectra indicate a fairly substantial optical depth for the dust, especially in the regions away from the south polar cap or away from high plateaus.

Observation of the Martian surface has so far been possible only in the region of the south polar cap, and perhaps over highlands, where the atmospheric dust is sufficiently thin. For quantitative interpretation, it is first necessary to establish the radiance originating from the planetary surface. This, in general, depends on the emissivity of the surface material, the degree of homogeneity of the surface within the field of view in terms of temperature and composition, and the opacity of the dust-filled atmosphere. From a working model, a background radiance curve for the average south polar spectrum shown in Fig. III-1b has been calculated and is included in the figure. The model assumes that an unknown fraction of the field of view is filled with a blackbody emitter at one temperature, while the rest of the field of view is filled with a blackbody at a second temperature. The model is based on the fact that the apparent size of the cap is slightly smaller than the IRIS field of view and is heterogeneous in structure. By using measured radiances at 295 cm^{-1}, 840 cm^{-1}, and 1330 cm^{-1}, and by

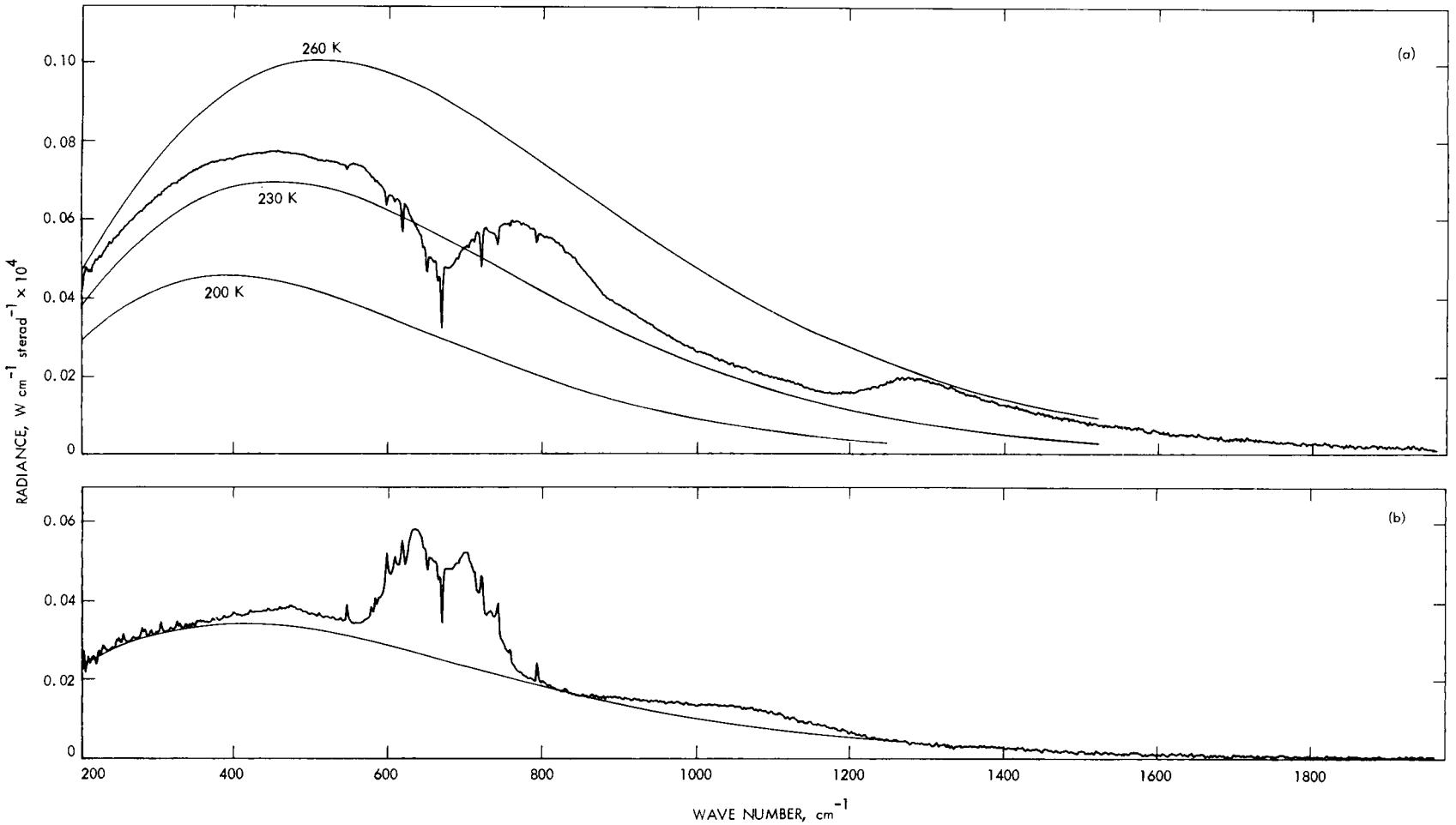

Fig III-1. (a) Example of non-polar thermal emission spectra. The spectrum is the average of six spectra obtained from Rev 8 in the region of 18°S latitude and 13°W longitude at about 12:00 local time. Blackbody curves are included for comparison. (b) Example of polar thermal emission spectra with south polar cap in IRIS field of view. This spectrum is the average of six individual spectra obtained from Revs 29 and 30. The smooth curve is the composite of two blackbody spectra, as described in the text.

assuming that they are unaffected by the atmosphere and by the dust in it, a fit was obtained with 65 ±5% of the field containing an emitter at 140 ±10 K and the remainder of the field filled with an emitter at 235 ±10 K. The result is consistent with a frozen CO_2 cap, in agreement with previous work (Refs. III-10 through III-12).

Estimates of the vertical temperature structure of the atmosphere can be obtained from measurements in the 667-cm^{-1} CO_2 absorption band by inversion of the integral equation of radiative transfer. If the atmospheric transmittance is known, temperature as a function of atmospheric pressure level can be derived. Preliminary retrievals of temperature profiles have been made assuming an atmosphere consisting of 100% CO_2, and neglecting possible additional opacity due to dust. A knowledge of surface pressure is also required for an accurate specification of temperature in the lower atmospheric levels. The apparently near-isothermal structure of the lower atmosphere and the effects of dust opacity have prevented determination of surface pressure from the spectral data. Therefore, use has been made of surface pressure estimates from Earth-based measurements and from *Mariner 6* and 7 data in regions where such data exist.

Examples of retrieved profiles are shown in Fig. III-2. The profiles over Hellas and Sinai are typical of those obtained from spectra similar to the non-polar cases of Fig. III-1a. Surface pressure was estimated for Hellas from *Mariner 7* ultraviolet spectrometer (UVS) measurements (Ref. III-13) and for Sinai from Earth-based radar measurements (Ref. III-14), which were normalized at coincident points to *Mariner 6* UVS pressure estimates. The lower lapse rates below 2 mb may be real. However,

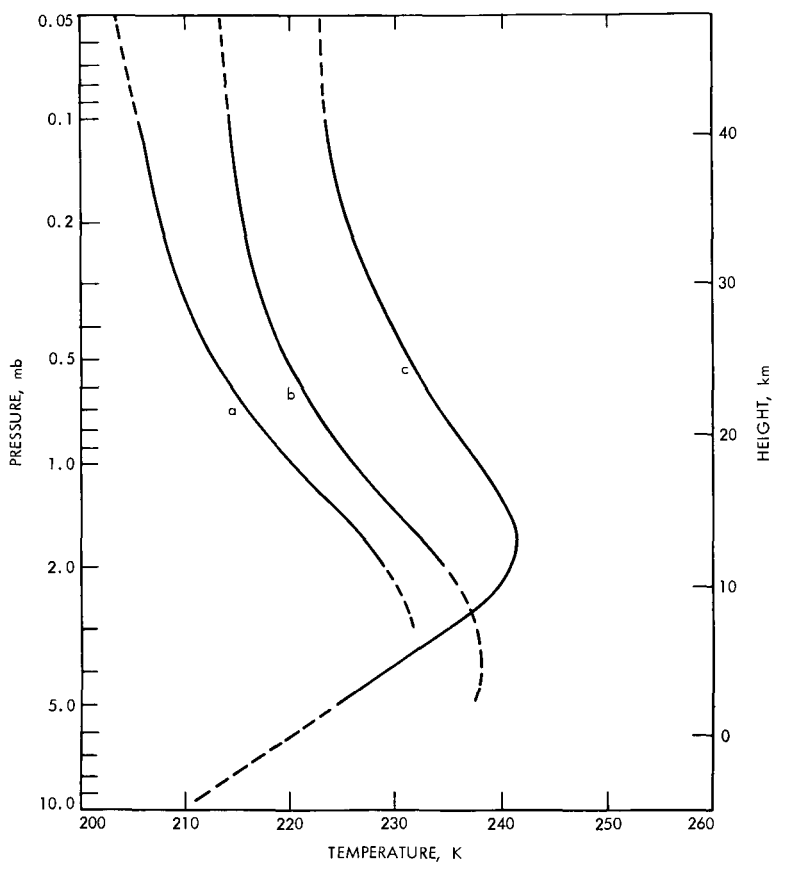

Fig. III-2. Temperature as a function of atmospheric pressure level for three Martian locations: 15.0°S, 64.2°W (Sinai) at 19:00 local time (a); 38.0°S, 282.8°W (Hellas) at 19:00 local time (b); 86.6°S, 342.2°W (south polar region) at 13:00 local time (c). Dashed parts of the curves are regarded as uncertain. An approximate height scale is included, using the triple-point pressure of water (6.1 mb) as a reference level.

if the dust has approximately unity optical depth in the 15-μm band at this level, a similar effect will result regardless of the true thermal structure in this region. When the optical depth of the dust is less than unity, the temperature retrieval will be essentially unaffected by the presence of the dust. As the optical properties of the dust become better understood, the lower portions of the profiles therefore may be subject to revision. The temperatures above 2 mb are generally warmer than either those predicted theoretically for a dust-free atmosphere (Ref. III-15) or those obtained from the *Mariner* 6 and 7 occultation experiments (Refs. III-16, III-17).

A profile obtained over the south polar cap is included in Fig. III-2. Here, the most outstanding feature is the pronounced temperature inversion; this is responsible for the CO_2 bands being seen partly in emission as in the polar spectrum shown in Fig. III-1b. Surface pressure estimates are not yet available in this region, but the basic behavior of the profile was essentially unaffected as the surface pressure was varied from 5 to 20 mb. Only the profile obtained using the 10-mb surface pressure is shown. Figure III-3 shows isotherms for a vertical cross section along a single scan pass down onto the cap and back off of the cap again. The lower part of the diagram is uncertain because of the neglect of dust in the analysis and lack of knowledge of the surface pressure. The cross section shows a highly localized region of warm air at about 1 to 2 mb in the vicinity of the cap. The substantial solar illumination during the south polar summer, the reflection of solar energy by the cap, and atmospheric dynamical effects are all possible mechanisms for producing this effect.

The polar spectra also show rotational lines of water vapor in the region between 200 and 350 cm^{-1}. This portion of the IRIS spectrum from Fig. III-1b has been expanded in Fig. III-4. Consistent with atmospheric temperatures warmer than surface temperatures, the water

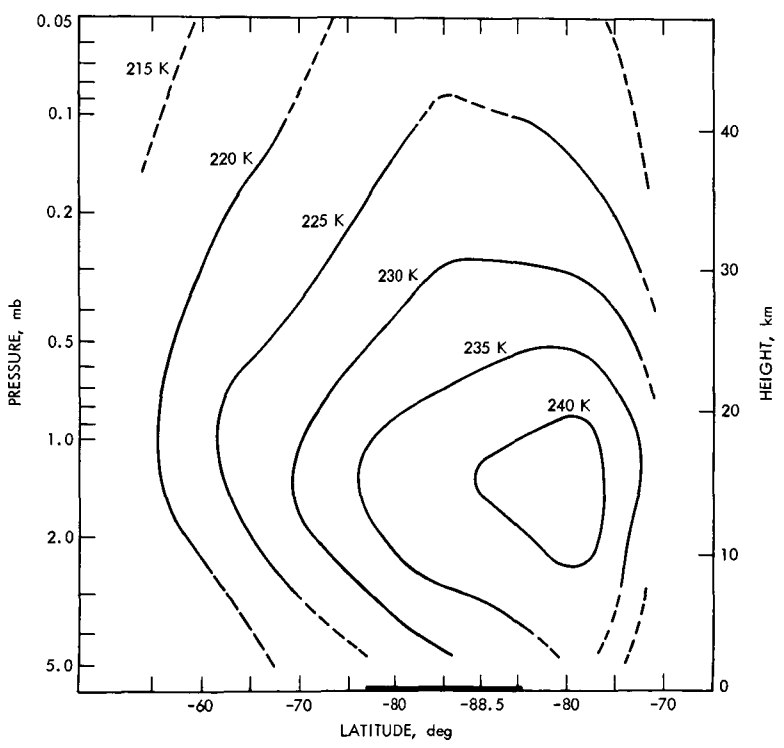

Fig. III-3. Isotherms for a cross section obtained from a single pass in the south polar region. The abscissa indicates the latitude of the center of the instrument's field of view as it approached the pole then moved away from it. Atmospheric pressure level is given along the ordinate with an approximate height scale similar to that of Fig. III-2. Dashed parts of the contours are uncertain. The heavy line at the bottom of the figure represents the extent of parts of the polar cap observed by the instrument.

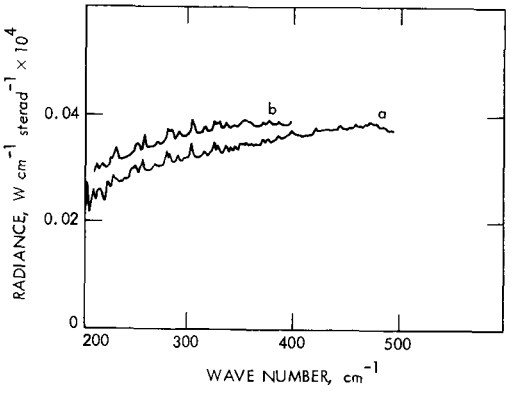

Fig. III-4. The 200- to 500-cm^{-1} portion of the south polar cap spectrum of Fig. III-1b is shown on an expanded scale (a). The numerous spectral lines appearing in emission are due to rotational water vapor lines in the lower Martian atmosphere. A synthetic water vapor spectrum (b) is included for comparison; the spectrum has been shifted upward by 0.005 radiance units.

vapor lines appear in emission. Also shown in Fig. III-4 is a synthetic slant path spectrum composed using the two-surface temperature model described. The excellent spectral correspondence verifies the existence of atmospheric water vapor in the south polar region. Water vapor spectral features appear more weakly over other regions of the planet. Possible reasons why water vapor is not more prominent there may be sought in the near-isothermal nature of the temperature profiles, the shielding effect of the dust, or possibly a lower water vapor concentration away from the south pole.

In summary, this experiment has been successful in providing information on the nature of the Martian atmosphere and surface. However, the conclusions appearing in this report must be regarded as preliminary. Additional efforts will be devoted to a more rigorous analysis of the data. A search for minor constituents will be carried out on spectral averages using statistical techniques. Components of intrinsic biological interest will be sought. A better understanding of the optical properties of suspended dust requires laboratory transmission measurements as well as the development of applicable radiative transfer models. These models are expected to improve estimates of surface pressures, temperatures in the lower atmosphere, and of the amount of atmospheric water vapor. The results obtained by the IRIS show the strength and versatility of high-resolution infrared spectroscopy as a tool for planetary exploration.

References

III-1. Hanel, R. A., Conrath, B. J., Hovis, W. A., Kunde, V., Lowman, P. D., Prabhakara, C., Schlachman, B., and Levin, G. V., *Icarus*, Vol. 12, p. 48, 1970.

III-2. Conrath, B. J., Hanel, R. A., Kunde, V. G., and Prabhakara, C., *J. Geophys. Res.*, Vol. 75, p. 5831, 1970.

III-3. Lyon, R. J. P., Technical Note D-1871, NASA, Washington, D.C., 1964. Lyon, R. J. P., Contractor Report CR-100, NASA, Washington, D.C., 1964.

III-4. Hovis, W. A., *Appl. Opt.*, Vol. 5, p. 245, 1966.

III-5. Aronson, J. R., Emslie, A. G., Allen, R. V., and McLinden, H. G., *J. Geophys. Res.*, Vol. 72, p. 687, 1967.

III-6. Salisbury, J. W., Vincent, R. K., Logan, L. M., and Hunt, G. R., *J. Geophys. Res.*, Vol. 75, p. 2671, 1970.

III-7. Conel, J. E., *J. Geophys.* Res., Vol. 74, p. 1614, 1969.

III-8. Hanks, T. C., and Anderson, D. L., *Phys. Earth Planet. Interiors*, Vol. 2, p. 19, 1969. Ringwood, A. E., and Clark, S. P., *Nature*, Vol. 234, p. 89, 1971.

References (contd)

III-9. Lowman, P. D., Jr., *J. Geology* (to be published).

III-10. Leighton, R. B., and Murray, B. C., *Science*, Vol. 153, p. 136, 1966.

III-11. Neugebauer, G., Münch, G., Kieffer, H., Chase, S. C., and Miner, E., *Astron. J.*, Vol. 76, p. 719, 1971.

III-12. Herr, K. C., and Pimentel, G. C., *Mariner Mars 1969: A Preliminary Report*, NASA SP-225, p. 83, Washington, D.C., 1969.

III-13. Hord, C. W., *Icarus* (to be published).

III-14. Pettengill, G. H., Rogers, A. E. E., and Shapiro, I. I., *Science* (to be published).

III-15. Gierasch, P., and Goody, R., *Planet. Space Sci.*, Vol. 16, p. 615, 1968.

III-16. Rasool, S. I., and Stewart, R. W., *J. Atm. Sci.*, Vol. 28, p. 869, 1971.

III-17. Kliore, A. J., Fjeldbo, G., and Seidel, B. L., *Space Research XI*, p. 165, Akademie Verlag, Berlin, 1971.

Acknowledgment

The following people contributed substantially to the success of the IRIS experiment on *Mariner 9*: D. Crosby, R. Gerace, W. Maguire, W. Miller, L. Purves, and N. Spencer of Goddard Space Flight Center; T. Burke, H. Eyerly, and J. Taylor of the Jet Propulsion Laboratory; E. Breihan, R. Bywaters, D. Rodgers, D. Vanous, and L. Watson of Texas Instruments, Inc.; W. Andrews, R. Bevacqua, and R. Long of Consultants and Designers, Inc.; Patricia Straat of Biospherics Incorporated.

IV. Infrared Radiometry Experiment

S. C. Chase, Jr. and H. Hatzenbeler[1]
Santa Barbara Research Center, Goleta, California

H. H. Kieffer
University of California, Los Angeles

E. Miner
Jet Propulsion Laboratory, Pasadena, California

G. Münch and G. Neugebauer
California Institute of Technology, Pasadena

A two-channel infrared radiometer similar to that carried on *Mariners 6* and *7* was included on *Mariner 9* in order to extend and improve the surface coverage and spatial resolution obtained on the earlier flights (Ref. IV-1). The radiometer measures the 10- and 20-μm radiation over an area coaxial with, and equal to about two-thirds of, that covered by the high-resolution television camera. At periapsis, the linear scale resolved by the radiometer approaches 20 km. The temperature resolution is on the order of 0.5 K. The radiometer has operated in orbit as expected.

In this section, preliminary results provided by the radiometer are presented, particularly those related to the dust storm prevalent on Mars during these observations. This discussion is qualitative because geometry data and local times have not been available for the majority of the orbits.

[1]Deceased.

In 1969, radiometric measurements of the largely dust-free planet could be explained in terms of simple thermal models with no appreciable influence by the Martian atmosphere. In 1971, in contrast, the general features of the observed thermal variations do not follow such simple models. The most striking difference is exhibited by the amplitude of the diurnal variations. On the basis of a typical 1969 model (thermal inertia = 0.006 cal cm^{-2} $sec^{-1/2}$ K^{-1}; albedo = 0.3), the surface temperatures at a latitude of about $-30°$ were expected to range from 185 K near the morning terminator to a peak of 290 K near the local noon. In fact, the observed brightness temperatures at this latitude have ranged only from 195 K just before sunrise to a maximum of 225 K. The maximum temperatures measured (around 250 K) occur at latitudes close to $-65°$. This observed thermal behavior cannot be explained by a simple conductive model without invoking unreasonable values of the thermal inertia. On the other hand, qualitative agreement with the observations can be obtained using simple models

that incorporate an atmospheric dust layer with modest visual absorption and reflectivity, with infrared emissivity and absorption coefficients of about 0.5, and with a heat capacity corresponding to that of the lower scale height of the atmosphere. The properties of the dust layer must be latitude dependent in the sense that its optical thickness must decrease toward the southern polar region.

The television experiment on *Mariner 9* has shown that the southern polar region, as well as certain other isolated areas of Mars, are relatively clear of obscuration by the dust. The residual polar cap is the most well defined feature observed in the thermal scans of Mars, and typically appears 35 K colder than the surrounding terrain.

At the surface of Mars, solid CO_2 must be at its saturated-vapor equilibrium temperature of 148 K. This temperature was observed by *Mariner 7* for the south polar cap during the early Martian spring, indicating that the bright deposit was predominantly frozen CO_2 at that time. In contrast, the minimum brightness temperature observed by the *Mariner 9* radiometer over the shrinking south polar cap, slightly after Martian southern mid-summer, is at least 25 K above the temperature that would correspond to frozen CO_2. From television images obtained simultaneously with the radiometer measurements, the observations correspond to an area at least 95% covered with a high albedo deposit.

If the cap is frozen CO_2, these data can be taken to indicate significant emission from the dusty atmosphere. The infrared optical thickness cannot, however, exceed unity as temperature variations have been observed which correlate with sharp features seen in visual images. The net amount of particulate matter required to produce the needed opacity is on the order of 1 mg cm^{-2} if its absorption coefficient is typical of silicates in the 10-μm range (Ref. IV-2). The possibility that some or all of the residual deposit is now frozen water cannot be excluded on the basis of these data alone.

The southernmost dark feature in Tharsis, at latitude $\sim 11°$, longitude $\sim 119°$W, also revealed on television images (see Section II of this report), was recognized by the radiometer as a region of about 300 km in length with a temperature about 8 K warmer than its surroundings. A straightforward interpretation of this phenomenon is that locally the atmosphere is more transparent, allowing increased energy to be absorbed by a darker surface. It is of interest to note that near this point radar topographic mapping (Ref. IV-3) shows an apparent ridge about 8 km higher than the mean elevation of Mars at this latitude. This provides a measure of the height of the effective dust layer.

Additional analysis of the data is now in progress to substantiate these preliminary interpretations.

References

IV-1. Neugebauer, G., Münch, G., Kieffer, H., Chase, S. C., Jr., and Miner, E., *Astron. J.*, Vol. 76, p. 719, 1971. Chase, S., Jr., Miner, E., Münch, G., and Neugebauer, G., *Icarus*, Vol. 12, p. 46, 1970.

IV-2. Hunt, J. M., Wisherd, M. P., and Bonham, L. C., *Analytical Chemistry*, Vol. 22, p. 1478, 1950. Wentink, T., and Planet, W. G., *J.O.S.A.*, Vol. 51, p. 595, 1961.

IV-3. Pettengill, G. H., Rogers, A. E. E., and Shapiro, I. I., *Science*, Vol. 174, p. 1321, 1971. Downs, G. S., Goldstein, R. M., Green, R. R., and Morris, G. A., *Science*, Vol. 174, p. 1324, 1971.

Acknowledgment

Appreciation is extended to the personnel of the entire *Mariner 9* project for their substantial efforts in our behalf, and to the staff of Santa Barbara Research Center for assistance during construction and calibration of the instrument. Appreciation also is extended to Judith Bennett, A. Law, B. Eenigenburg, R. Newell, J. Otte, M. Sander, and D. Schofield for their work with this experiment; and to R. B. Leighton for his discussion of this paper.

V. Ultraviolet Spectrometer Experiment

C. A. Barth, C. W. Hord, and A. I. Stewart
University of Colorado, Boulder

A. L. Lane
Jet Propulsion Laboratory, Pasadena, California

Two major objectives of the ultraviolet spectrometer experiment are: (1) measurement of the structure and composition of the upper atmosphere and (2) photometric and spectral mapping of the lower atmosphere and surface of Mars (Ref. V-1). The upper atmosphere measurements are performed by observing the sunlit limb of the planet as the spacecraft motion causes the field of view of the instrument to pass through successively lower levels of the atmosphere. Measurements of the lower atmosphere are obtained by pointing the instrument directly at the area of the planetary disk that is being mapped. The *Mariner 9* spectrometer is similar to those used on *Mariners 6* and *7* and *OGO-4* (Ref. V-2). During the first 30 days of the mission, the ultraviolet spectrometer measured the temperature and density of the upper atmosphere of Mars and discovered that this atmosphere, like the Earth's, responds to changes in solar activity. The spectrometer also measured the spectral and photometric properties of the atmosphere during the protracted dust storm of 1971.

A. Upper Atmosphere

During the first 30 days, observations of the airglow above the bright limb of Mars made on 14 orbits were of quality sufficient to provide good altitude profiles. The principal spectral emissions observed during these limb crossings were those first measured in 1969 by the ultraviolet spectrometers on *Mariners 6* and *7* (Ref. V-3): the atomic hydrogen 1216 Å Lyman alpha line; the atomic oxygen 1304, 1356, and 2972 Å lines; the atomic carbon 1561 and 1657 Å lines; the carbon monoxide A-X fourth positive and a-X Cameron bands; the ionized carbon monoxide B-X first negative bands; and the ionized carbon dioxide B-X and A-X bands. This Martian airglow is produced by the action of solar ultraviolet radiation on the atoms and molecules in the upper atmosphere of Mars.

The airglow spectrum of Mars in the 1910 to 2460 Å range shown in Fig. V-1 contains the intense CO a-X

bands and the weaker CO^+ B-X bands. Figure V-2 demonstrates that the CO A-X bands contribute most of the intensity in the 1420 to 1760 Å region, while the atomic carbon lines make a substantial contribution. Because

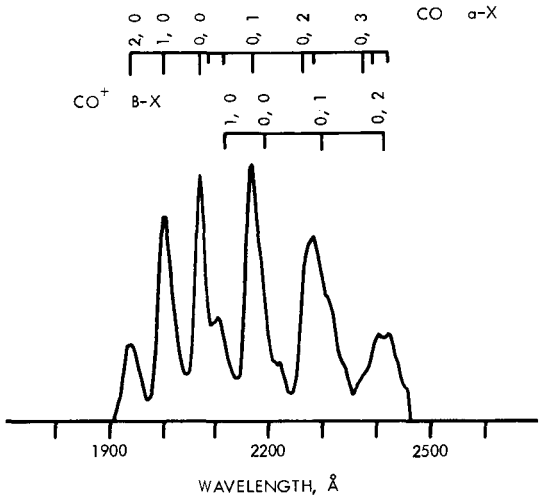

Fig. V-1. Airglow spectrum of Mars between 1910 and 2460 Å. This wavelength interval, which contains the CO a-X Cameron bands and the CO^+ B-X first negative bands, was used to obtain the emission rates shown in Fig. V-3. This calibrated spectrum was obtained by summing 20 individual spectral observations, as was the spectrum in Fig. V-2.

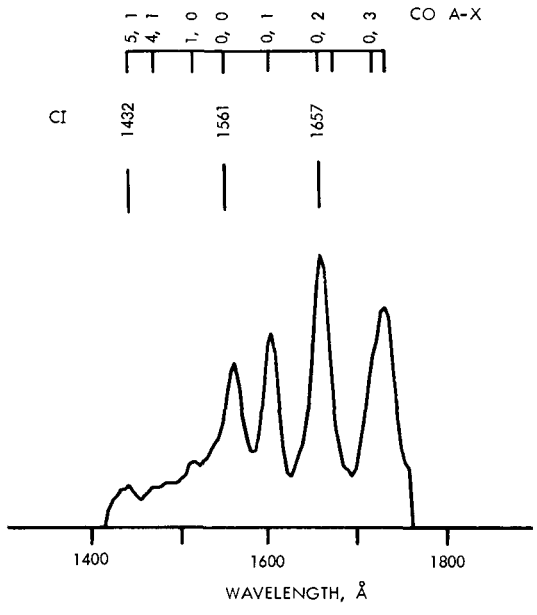

Fig. V-2. Airglow spectrum of Mars between 1420 and 1760 Å. This wavelength interval, which contains the CO A-X fourth positive bands and the CI atomic carbon lines, was used to obtain the emission rates in Fig. V-3.

the analysis of the *Mariner 6* and *7* data showed that the most probable source of excitation of the carbon monoxide A-X and a-X bands is the electron and photon impact-induced dissociative excitation of carbon dioxide, the intensity of these bands as a function of altitude is used to determine the density distribution of carbon dioxide in the upper atmosphere of Mars (Ref. V-4). In turn, the scale height of these emissions is used to deduce the temperature of the upper atmosphere. The emission rate of these two band systems as a function of altitude is presented in Fig. V-3 for a limb observation that was made on Rev 34 on December 1, 1971, and is typical of the quality of the limb measurements made during the first 30 days.

An indicator of the amount of atomic oxygen in the atmosphere is the 1304 Å resonance line of atomic oxygen that appears in the airglow. The apparent emission rate of this line on pass 34 is plotted in Fig. V-4. Because this emission line is optically thick in the Mars' atmosphere, multiple scattering occurs and a radiative transfer analysis has to be performed to determine the atomic oxygen density (Ref. V-5).

The Lyman alpha airglow line, which is a measure of the atomic hydrogen density in the atmosphere of Mars, extends to great altitudes above the planet. The apparent emission rate of this line on Rev 34 was determined as a function of altitude and also is plotted in Fig. V-4. Individual measurements were fitted with a straight line as shown in the figure. This emission line is also optically thick, although not as thick as the atomic oxygen line. To determine the exospheric temperature and density distribution of atomic hydrogen, it is necessary to analyze this emission along the entire orbit, which extends to an altitude of 17,000 km (Ref. V-6).

Parameters describing the limb crossings, relevant solar indices, and a summary of some preliminary results obtained from the limb data for the first 30 days are presented in Table V-1. The solar indices are the Ottawa 10.7-cm flux index, and the Zurich sunspot number; an approximate time adjustment has been made to allow for the non-zero angle between Mars, the Sun, and the Earth (Ref. V-7). The atmospheric quantities included in the table are the scale height of the CO a-X bands and intensity of Lyman alpha. The scale height is calculated in the 160- to 220-km region (Ref. V-4), and the 2σ error is on the order of ± 3 km.

Variations in the scale height are of particular importance because they are of sufficient magnitude to be

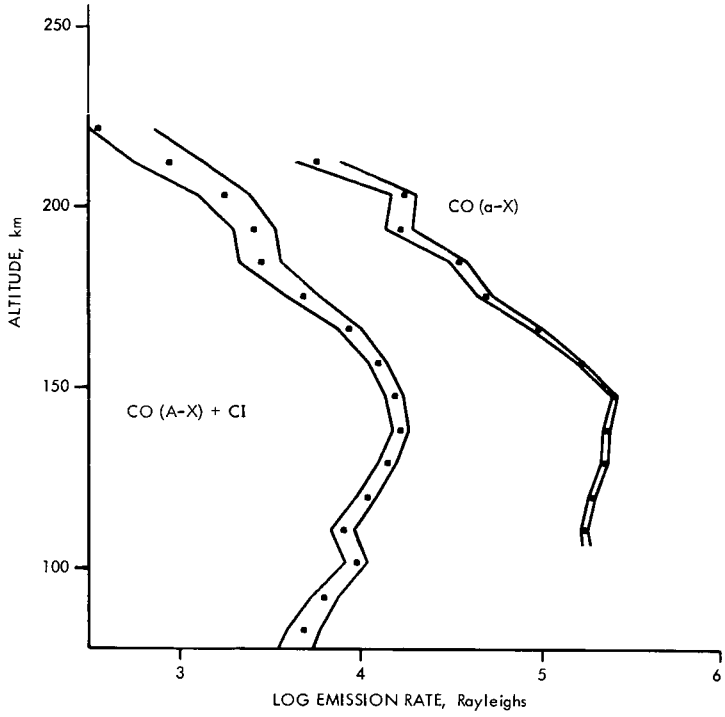

Fig. V-3. Emission rates of the CO a-X Cameron bands and the sum of the CO A-X fourth positive bands and the atomic carbon lines as a function of altitude. The wavelength intervals used to obtain these two airglow profiles are shown in Figs. V-1 and V-2. Data points are dots; the envelopes represent ±2 standard deviation error bars derived from counting statistics.

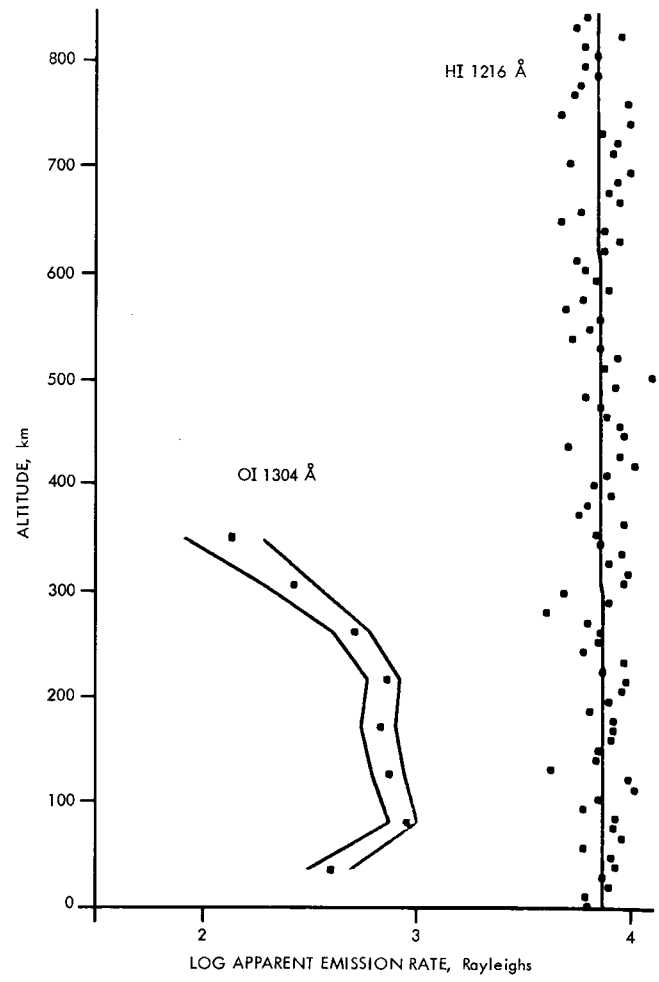

Fig. V-4. Apparent emission rates of the atomic hydrogen 1216 Å line and the atomic oxygen 1304 Å line as a function of altitude. Data points are dots; the envelope around the 1304 Å data represents the $\pm 2\sigma$ error bars derived from counting statistics. The line through the 1216 Å data is a straight line fitted by a least-squares method.

Table V-1. Airglow observations above the bright limb

Rev	Limb crossing time (GMT)	Limb crossing		cos χ[b]	ΔZ,[c] km	Scale height,[d] km	10.7-cm flux[e]	Lyman alpha intensity,[f] kR	R_Z[g]
		Latitude,[a] °S	Longitude,[a] °W						
2	Nov. 15, 01:24	24	212	0.98	7.6	22	107	7.7	45
28	Nov. 28, 01:54	46	105	0.84	9.3	22	122	7.4	64
30	Nov. 29, 01:51	48	92	0.85	9.3	22	115	6.4	69
32	Nov. 30, 01:48	45	85	0.84	9.3	20	113	6.6	80
34	Dec. 1, 01:45	47	69	0.85	9.3	18	109	7.1	63
36	Dec. 2, 01:41	46	62	0.85	9.2	17	117	6.4	70
38	Dec. 3, 01:39	47	51	0.85	9.1	24	115	6.9	92
40	Dec. 4, 01:37	47	40	0.85	9.1	26	117	6.9	107
42	Dec. 5, 01:30	12	0	0.99	3.7	18	118	7.2	83
44	Dec. 6, 01:34	47	19	0.85	9.1	19	125	7.4	108
46	Dec. 7, 01:31	46	8	0.85	9.1	19	128	7.2	122
54	Dec. 11, 01:16	46	325	0.86	8.8	19	124	7.2	85
56	Dec. 12, 01:12	45	315	0.85	8.8	17	127	7.2	98
58	Dec. 13, 01:07	45	303	0.86	8.8	22	122	7.7	80

[a]Approximate.

[b]Cosine of the solar zenith angle at the limb crossing.

[c]Altitude interval between successive spectra.

[d]Determined from the CO a-X emissions.

[e]Provisional Ottawa solar 10.7-cm flux index.

[f]At an altitude of 150 km.

[g]Provisional Zurich sunspot number. The authors are indebted to Professor M. Waldmeier of the Swiss Federal Observatory, Zurich, for providing provisional sunspot numbers in advance of publication. On November 30, due to the relative positions of Mars, Earth, and the Sun, solar features lying on the sub-Earth meridian had lain on the sub-Mars meridian 3.0 days earlier. The position of the solar indices in the table take account of this 3-day correction. More precise corrections, 2.4 days for the Ottawa 10.7-cm flux index and 2.8 days for the Zurich sunspot number, would take account also of the different GMT appropriate to the limb crossing (0200), the Ottawa index (1700), and the Zurich number (0600-0900). The corrections increase by about 1 day per month.

statistically significant. They occur during a time of changes in the solar 10.7-cm flux, which is an indicator of the intensity of the solar radiations that ionize and heat the Earth's upper atmosphere. It seems likely that the temperature of the upper atmosphere of Mars is responding to changes in solar activity, but that it also is affected by atmospheric processes not necessarily connected with changes on the Sun. The Lyman alpha intensities seem to be correlated with the Zurich sunspot number, which has been shown to be an indicator of the intensity of the solar Lyman alpha radiation (Ref. V-6). However, the variation in these intensities may reflect actual changes in atomic hydrogen densities in the Martian atmosphere.

These two observations demonstrate a curious result of space exploration. The Martian atmosphere is responding to changes in solar activity, and the *Mariner 9* ultraviolet spectrometer is detecting this response 3 days before the effects of the changes are felt in the Earth's atmosphere.

B. Lower Atmosphere

Over the entire disk of Mars, except at the polar cap, the reflected spectrum is produced by the scattering of sunlight by molecules and particles in the atmosphere. In contrast to the spectra obtained by the *Mariner 6* and 7 ultraviolet spectrometers in 1969, the spectral

shape of the *Mariner 9* reflectance depends on what particular location on the planet is being observed. While the details in the spectra of Mars originate in the solar spectrum, the overall spectral shape is determined by the relative amount of molecular or large particle scattering taking place. Two examples of Mars spectra are shown in Figs. V-5 and V-6 together with the reflectance as a function of wavelength. Reflectance as used in this report is defined as ¼ times the ratio of the intensity (photons cm^{-2} sec^{-1} $Å^{-1}$) of the region of Mars being observed to the solar flux (photons cm^{-2} sec^{-1} $Å^{-1}$).

The occurrence of the protracted dust storm on Mars has changed the characteristics of the ultraviolet reflectance from those observed by *Mariners 6* and *7* in 1969. The magnitude of the reflectances is smaller than in 1969. When the measurements obtained by *Mariners 6* and *7* and *Mariner 9* at phase angles varying from 15

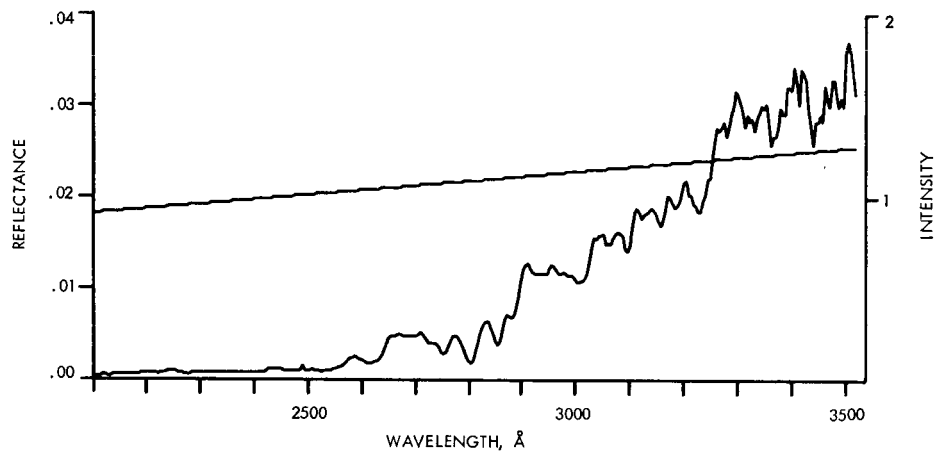

Fig. V-5. Ultraviolet reflectance in dusty region. The intensity of the ultraviolet spectrum observed on Mars near latitude 45°S on the revolution described in Fig. V-7 when the illumination angle was 52°, the viewing angle 36°, and the phase angle 79°. [Units on the right-hand ordinate are 10^{13} photons cm^{-2} sec^{-1} $(15\ Å)^{-1}$].

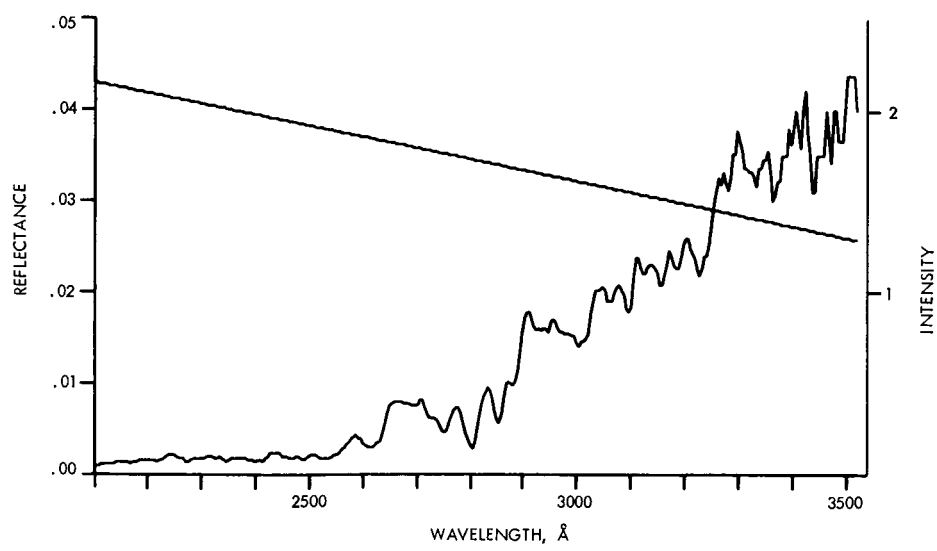

Fig. V-6. Ultraviolet reflectance in polar region. The intensity and reflectance of Mars obtained near latitude 86°S on the revolution shown in Fig. V-7 when the illumination angle was 65°, the viewing angle 59°, and the phase angle 38°.

to 84° are extrapolated to 0° phase angle, the geometric albedo of Mars at 3050 Å in 1971 is 0.025 compared with 0.035 in 1969. This result indicates that the dust, which is dominating the ultraviolet light scattered from the disk of Mars, is a strong absorber in the ultraviolet.

A model to explain the observed variation of reflectance across the planet has been constructed using the following information: the low value of reflectance and lack of small-scale variations imply that the single scattering albedo of the dust particles, $\tilde{\omega}_0$, is small and that the optical depth, τ, is greater than 1. Marked deviations from this model for the reflectance and color ratios occur only near the south polar cap. Figure V-7 demonstrates this result from data obtained on Rev 48. The increase in reflectance seen on the left side of Fig. V-7 occurred when the spectrometer field of view crossed the south polar cap of Mars, indicating that the atmosphere is sufficiently clear for ultraviolet light to penetrate to the surface. During this orbit, a contiguous swath of reflectance data was obtained when the field of view crossed the polar cap and then moved northward. It may be seen in the figure that the model adequately explains the reflectance except in the south polar region where the reflected light intensity is larger than the model predicts. At this same location, the blue color ratio is high and the red color ratio low. These results indicate that there is an enhancement in the Rayleigh scattering contribution to the reflectance at this location and, hence, a decrease in the amount of dust in the atmosphere as compared to the rest of the planet. The increase in intensity in the south polar region is equivalent to a clear atmosphere of 1.4-mb pressure above the effective ultraviolet absorption level.

C. Phobos

Several ultraviolet spectra of Phobos were obtained on Rev 48 during the spacecraft sequence that also produced two television pictures of Mars' inner satellite. One of these spectra in the wavelength region between 2550 and 3450 Å is shown in Fig. V-8. The absolute values of both the intensity and reflectance in the figure are lower limits set by assuming that Phobos was fully within the field of view of the spectrometer. The current best estimate of the actual reflectance would double the scale given in Fig. V-8. Its magnitude is still significantly less than that of Mars. The reflectance of Phobos de-

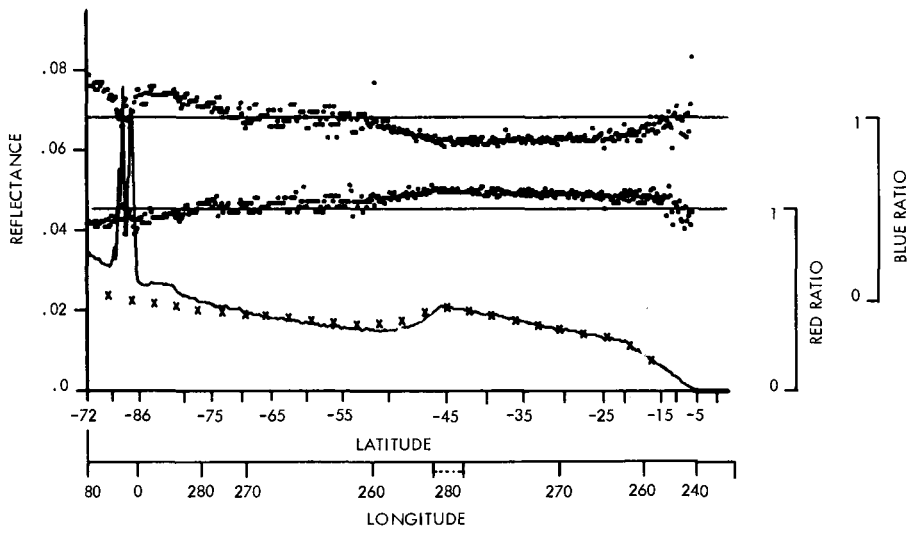

Fig. V-7. Reflectance at 3050 Å and blue and red color ratios for Rev 48 observations. The solid curve represents the reflectance measured in a 100 Å wide band centered at 3050 Å. Results of calculations with the model that has $\tilde{\omega}_0 \angle\angle 1$ and $\tau \gtrsim 1$ are indicated by the x symbols. The color ratios are plotted as dots for each spectral observation on the planet. The blue ratio is defined as the ratio of the reflectance measured at 2580 Å to that at 3050 Å, and the red ratio is the 3380 Å reflectance relative to the 3050 Å value. A value of 1 for the blue and red ratios is equivalent to the color of the Sun. Note that the blue ratio scale is displaced upward.

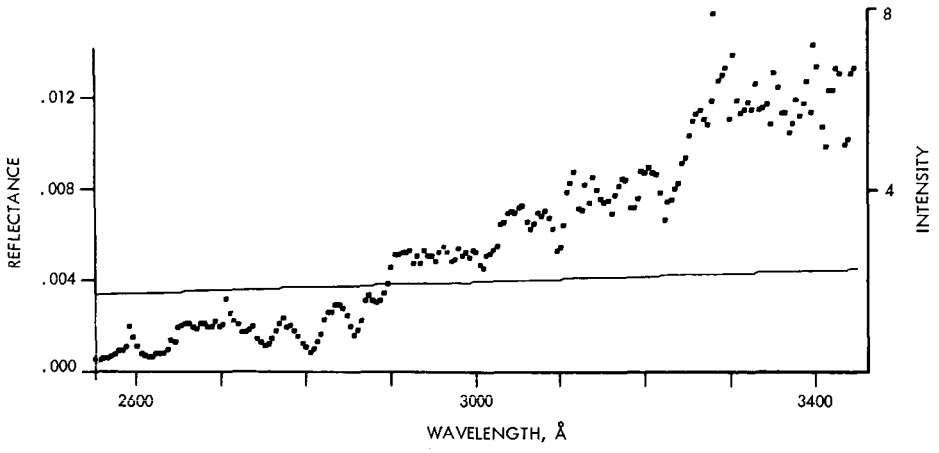

Fig. V-8. Phobos ultraviolet reflectance. The relative spectral intensity and reflectance of Phobos obtained on Rev 48. Values of reflectance and intensity are lower limits. [Units on the right-hand ordinate are 10^{12} photons cm^{-2} sec^{-1} $(15\ Å)^{-1}$]. At the time of the observation, the Sun–Phobos–instrument angle was 49°.

creases as the wavelength decreases from 3450 to 2550 Å. The reflected light has essentially the same color as Martian dust (Fig. V-5).

D. Summary

In 30 days of orbital observations, the ultraviolet spectrometer measured the density distribution of the upper atmosphere of Mars and obtained the first observations of variations in this distribution as a function of solar activity. During this same period, the atomic hydrogen and atomic oxygen airglows were present during each limb observation. Airglow intensities observed in this experiment are comparable to those observed in the *Mariner 6* and *7* experiment in 1969.

In sharp contrast to the upper atmosphere observations, the lower atmosphere of Mars is different in 1971 than it was in 1969. *Mariners 6* and *7* found a clear atmosphere in which molecular scattering determined the ultraviolet reflectance. The ultraviolet reflectance measured by *Mariner 9* is dominated by particle scattering. The atmosphere above the polar region is clearer than that over the rest of the planet.

References

V-1. Hord, C. W., Barth, C. A., and Pearce, J. B., *Icarus*, Vol. 12, p. 63, 1970.

V-2. Barth, C. A., and Mackey, E. F., *IEEE Transactions on Geoscience Electronics GE-7*, p. 114, 1969. Pearce, J. B., Gause, K. A., Mackey, E. F., Kelly, K. K., Fastie, W. G., and Barth, C. A., *Appl. Optics*, Vol. 10, p. 805, 1971.

V-3. Barth, C. A., Fastie, W. G., Hord, C. W., Pearce, J. B., Kelly, K. K., Stewart, A. I., Thomas, G. E., Anderson, G. P., and Raper, O. F., *Science*, Vol. 165, p. 1004, 1969. Barth, C. A., Hord, C. W., Pearce, J. B., Kelly, K. K., Anderson, G. P., and Stewart, A. I., *J. Geophys. Res.*, Vol. 76, p. 2213, 1971.

References (contd)

V-4. Stewart, A. I., *J. Geophys. Res.*, Vol. 77, p. 54, 1972.

V-5. Thomas, G. E., *J. Atmos. Sci.*, Vol. 28, p. 859, 1971. Strickland, D. J., Thomas, G. E., and Sparks, P. R. (to be submitted to *J. Geophys. Res.*).

V-6. Anderson, D. E., Jr., and Hord, C. W., *J. Geophys. Res.*, Vol. 76, p. 6666, 1971.

V-7. Barth, C A., and Hord, C. W., *Science*, Vol. 173, p. 197, 1971. Hord, C. W., *Icarus* (to be published).

Acknowledgement

In addition to the authors, the ultraviolet spectrometer team consists of R. C. Bohlin, R. L. Davis, M. L. Dick, L. R. Dorman, P. E. Evans, R. A. Goettge, K. K. Kelly, A. H. Lineberger, G. G. McNutt, K. D. Pang, J. B. Pranke, L. H. Parmelee, S. Schaffner, K. E. Simmons, D. M. Stern, and D. J. Strickland at the University of Colorado; and J. M. Ajello, J. W. Farrar, and R. F. Ebbett at the Jet Propulsion Laboratory.

VI. S-Band Occultation Experiment: Atmosphere, Ionosphere, and Topography of Mars

A. J. Kliore, D. L. Cain, G. Fjeldbo, and B. L. Seidel
Jet Propulsion Laboratory, Pasadena, California

S. I. Rasool
NASA Headquarters, Washington, D.C.

In 1965 and again in 1969, the radio occultation technique was used to explore the atmosphere of Mars (Refs. VI-1 through VI-4). The 1965 experiment disclosed the existence of a very low atmospheric pressure at the surface of Mars, a finding which was later supported by the results from the two *Mariner* flybys in 1969, which also provided information on the shape of Mars. In each case, only one set of entry and exit occultation measurements was obtained by each spacecraft for a total of six separate measurements. In contrast, the *Mariner 9* spacecraft is occulted by Mars twice in each 24 hr, thus equaling in 1 day the total radio occultation information output of *Mariners 6* and *7* in 1969. The occultations will continue for a period of about 40 days from orbital insertion; about 160 separate occultation measurements will be made.

Fifteen radio occultation measurements were taken during the first 9 days in orbit when the spacecraft entered occultation, beginning with Rev 1 on November 14 and ending with Rev 17 on November 22, 1971. Although data were also taken when the spacecraft exited occultation, these data are more time-consuming to analyze and will be reported later, as well as the data from the remaining revolutions. The data used in this analysis were provided by the closed-loop receivers at the Deep Space Stations at Goldstone, California; Woomera, Australia; and Cebreros, Spain.

The data were analyzed using trajectory information provided by the *Mariner 9* Navigation Team, applying the technique of integral inversion (Refs. VI-2 and VI-5) to obtain a vertical profile of refractivity in the ionosphere and atmosphere of Mars. For the purposes of profile inversion, the atmosphere of Mars was assumed to be spherically symmetric and it was postulated to consist solely of carbon dioxide. The boundary temperature for inversion was chosen as 150 K at about 3440 km.

Locations of points at which the measurements described in this article were made are shown in Fig. VI-1. Because of the 12-hr orbital period of *Mariner 9*, successive occultation points fall about 180° apart in longitude; successive measurements in the same region are

made every 24 hr and lie about 9° apart in longitude. The even-numbered occultations, observed from Goldstone, occurred in a region stretching from Mare Sirenum to Solis Lacus at latitudes from about 40° to about 33° south. The odd-numbered occultations, observed from Australia and Spain, corresponded to measurements extending from Yaonis Regio to Trinacria, crossing the classical bright area of Hellas.

Temperature profiles obtained from the data from Revs 1 through 9 are shown in Fig. VI-2. (Revs 4 and 5 were plagued with bad data.) The irregular appearance of the profiles, caused by phase jitter noise in the doppler data, and the scatter in temperature values, most likely caused by residual bias, are indicative of the current uncertainties in these measurements. It must be emphasized that a large portion of this systematic uncertainty can be removed through additional analysis. As shown in Fig. VI-2, the temperature remains approximately constant in most profiles from the surface to about the level of 3405 km, and lapses with altitude at about 2 K/km above that height. The near-isothermal nature of the lower atmosphere is not too surprising a Martian phenomenon because a similar condition was observed during the entry of *Mariner 4* into occultation (Ref. VI-2). However, the *Mariner 4* and 9 measurements were made at different local times and solar illumination conditions. If measurements from *Mariner 9* are compared with *Mariner 6* and 7 entry data obtained for similar solar zenith angles and local times, a significant change is found in the thermal state of the atmosphere. The 1969 data yielded temperature profiles with somewhat subadiabatic lapse rates (3 K/km; Ref. VI-3), which were still lower than those predicted by theory for a clean atmosphere (Ref. VI-6). The fact that most *Mariner 9* temperature profiles show this isothermal regime near the surface is significant, and indicates that the mechanism causing this phenomenon is global in extent, at least for the latitudes and local times of measurement. One possible explanation lies in the extensive dust storm that had been obscuring the surface in the visible and near-visible wavelengths during the time of the occultation measurements. It is probable that the isothermal effect is caused by solar radiation being absorbed by the fine dust suspended in the atmosphere, thus raising the temperature of the dust particles and in turn heating the atmosphere. This hypothesis suggests that dust exists in the atmosphere of Mars to altitudes of at least 15 to 20 km.

Additional temperature profiles from data taken during Revs 10 through 17 are shown in Fig. VI-3. The appearance of the profiles is similar to Fig. VI-2; however, there is the suggestion that the profiles for the latest Revs (16 and 17) are less isothermal.

A summary of the 15 measurements appears in Table VI-1. The present uncertainties associated with the radius, surface pressure, and surface temperature, respectively, are about ±2.5 km in radius, 0.5 mb in pressure, and 15 K in temperature. Immediately apparent from Table VI-1 is the large variation between measurements in the distance from the center of mass (hereafter called radius), amounting to about 13 km, with an accompanying variation in the surface pressure from 2.9 to 8.3 mb. These large excursions, in both radius and surface pressure, are not surprising, as the topographical measurements of the surface of Mars made with Earth-based planetary radars had indicated surface relief of precisely that magnitude (Ref. VI-7).

The measured surface pressures are plotted versus the radius in Fig. VI-4. The measurements of radius and surface pressure by means of the radio occultation technique are almost entirely independent of one another. The first depends primarily on the distance of the radio beam from the center of Mars at the time of interruption of signal; the second depends on the total refractive effect upon the propagation velocity and direction of the radio waves. From Fig. VI-4, it is obvious that the surface pressure is well correlated with the measured radius. In fact, the variation of surface pressure with radius is almost totally consistent with the 12-km scale height implied by the temperature measurements.

The dashed line in Fig. VI-4 is a theoretical pressure profile assuming a pressure of 8.3 mb at a radius of 3384 km and a scale height of 12 km. Even with this crude approximation, the fit is excellent, in agreement with the observed isothermal temperature structure in the lower atmosphere. The individual deviations of the measured points from the computed curve probably are due to differences in temperature between the measurements. The vertical lines in Fig. VI-4 indicate the bounds of the mean radius of Mars computed on the basis of a model for the physical shape of Mars that consists of an ellipsoid with an equatorial radius of 3394 km and a flattening of 0.0057. This model was computed from Mars radius measurements by *Mariners 4, 6,* and 7 (Ref. VI-8). Because the latitude at the point of the measurement changes from about 40°S for Rev 1 to about 33°S for Rev 17, the mean radius also increases by about 2 km. It can readily be seen from Fig. VI-4 that most of the measurements were made in regions that lie above the mean radius and only a few of the points lie below the

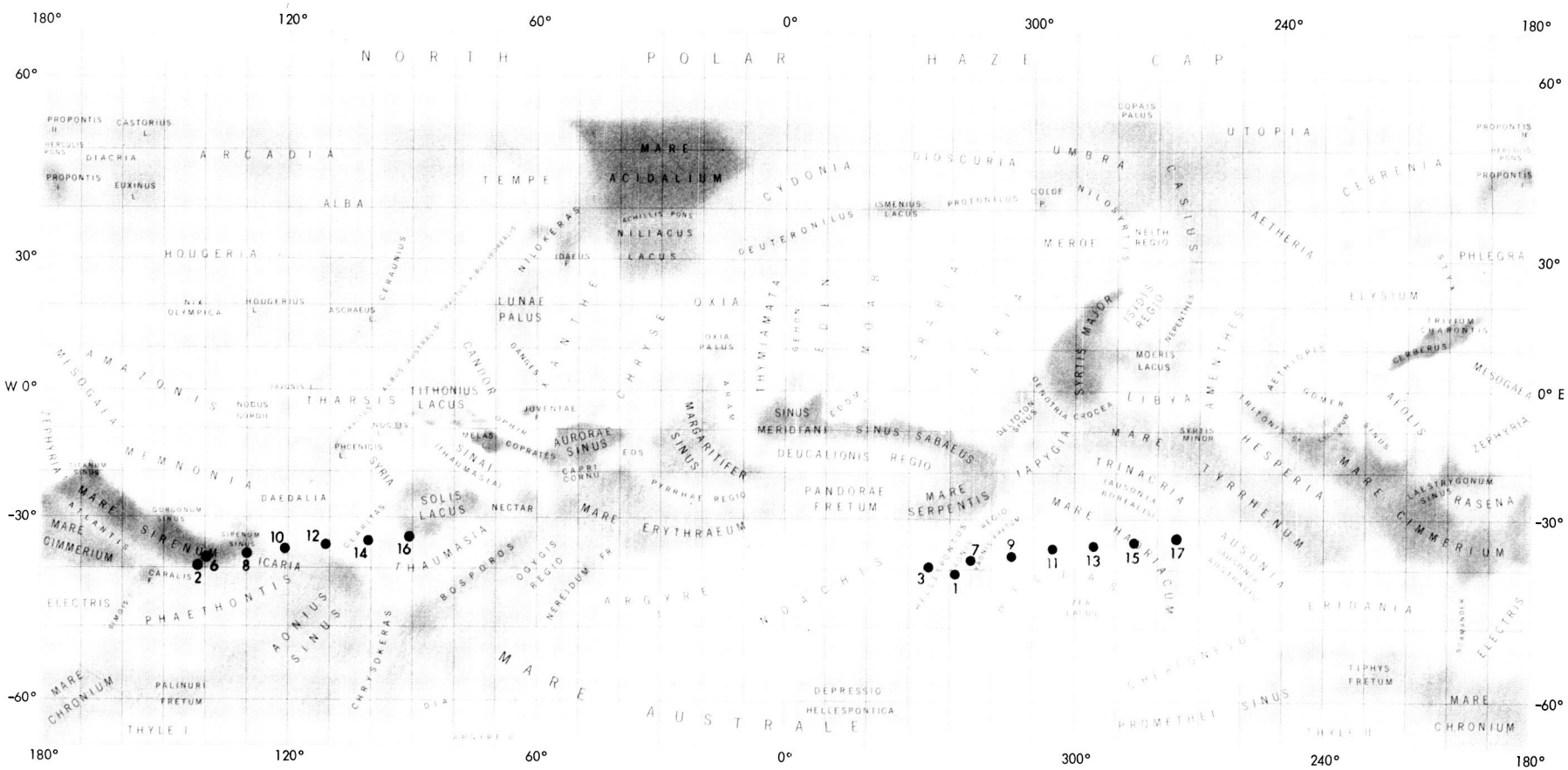

Fig. VI-1. Locations of occultation measurement points on the surface of Mars. The map was prepared under the direction of Dr. Gerard de Vaucouleurs of the University of Texas.

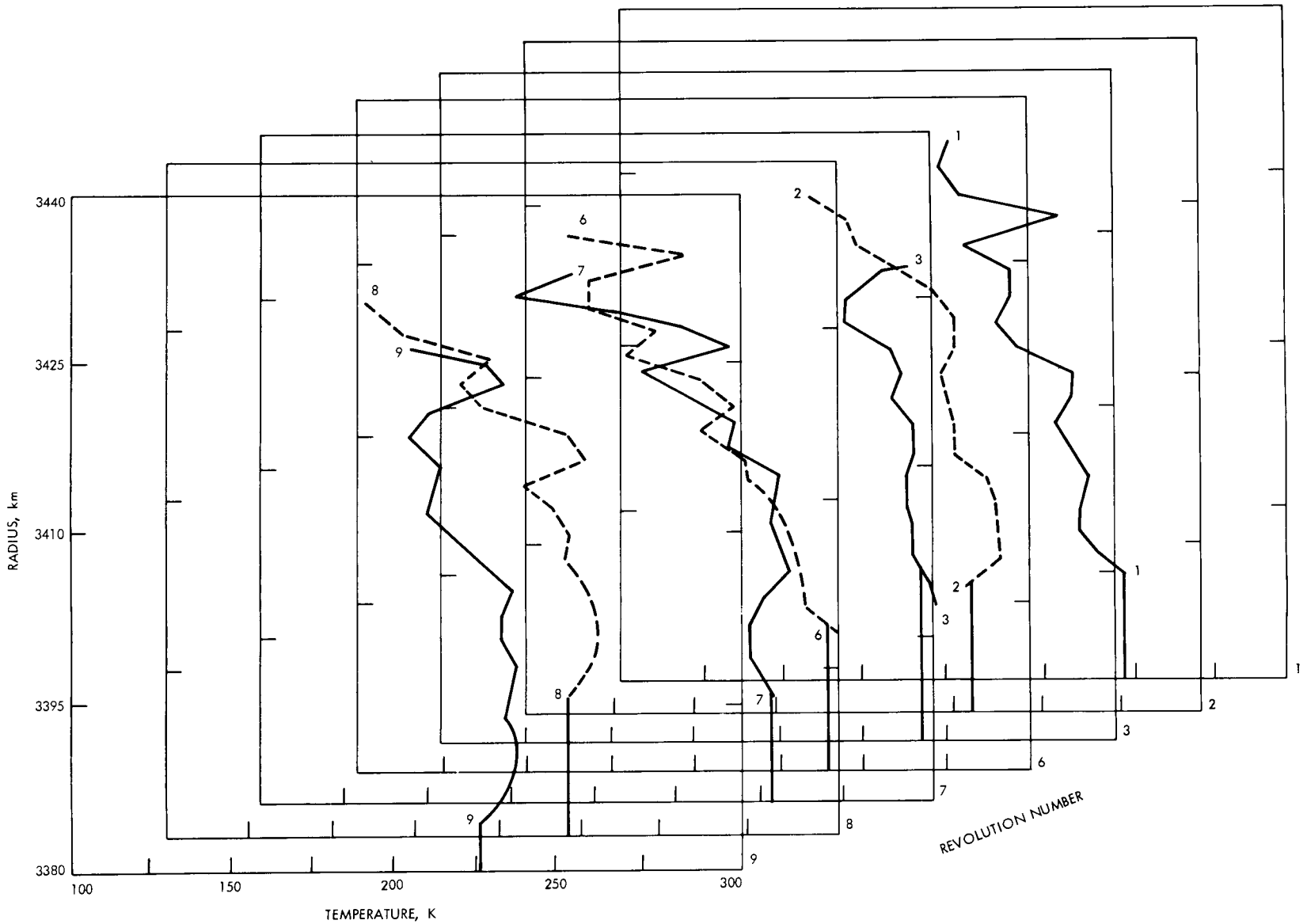

Fig. VI-2. Atmospheric temperature profiles for Revs 1 through 9. The uneven appearance of the profiles and the scatter of temperature values are indicative of the uncertainties associated with the measurement.

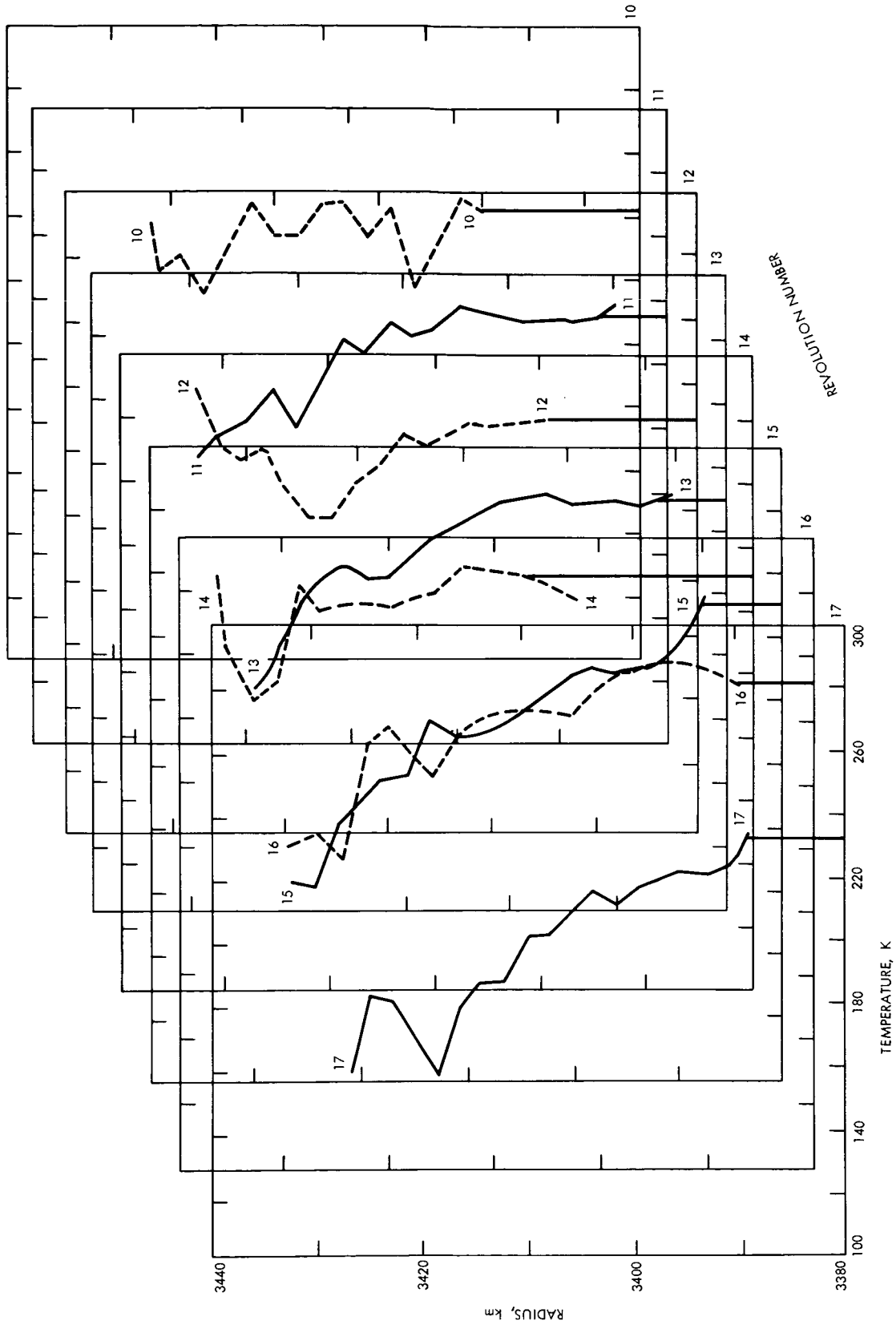

Fig. VI-3. Atmospheric temperature profiles for Revs 10 through 17.

Table VI-1. Occultation measurements

Rev	Latitude, °S	Longitude, °W	Location	Radius, km	Surface pressure, mb	Surface temperature, K
1	40.3	319	Yaonis Regio	3388.1	4.7	251
2	39.9	142	Mare Sirenum	3391.2	4.1	230
3	39.4	326	Hellespontus	3391.9	4.0	248
6	38.2	140	Mare Sirenum	3392.1	3.9	244
7	37.7	315	Yaonis Fretum	3389.6	5.2	255
8	37.3	130	Sirenum Sinus	3392.3	3.9	222
9	36.8	305	Hellas	3383.5	8.3	222
10	36.3	121	Icaria	3394.6	3.4	241
11	35.9	296	Hellas	3384.4	8.1	239
12	35.4	111	Daedalia	3393.3	3.7	228
13	35.0	286	Hellas	3384.6	8.2	232
14	34.5	101	Claritas	3396.7	2.9	224
15	34.0	276	Mare Hadriacum	3387.2	7.1	256
16	33.5	91	Solis Lacus	3395.6	3.4	250
17	33.0	266	Trinacria	3388.7	5.9	237

mean radius. This can be amplified with reference to Figs. VI-5 and VI-6. Figure VI-5 shows the variation of the radius and surface pressure with longitude in the Hellas region. The value of the mean radius is shown as an unequally dashed line. It is immediately obvious that all of Hellas lies substantially below the mean radius, and that the atmospheric pressure at its surface is higher than the average. In a cross section extending for about 30° of longitude (corresponding to approximately 1200 km at the latitude in question), the surface of Hellas lies about 4 km below the mean radius. Its western rim, in the regions of Hellespontus and Yaonis Fretum, lies about 2 km above the mean radius; thus, there is a drop in altitude of 6 km in a horizontal distance of approximately 550 km, corresponding to a slope on the scale of 550 km of about 0.6° in the region.

During the flyby of *Mariner* 7 in 1969, Hellas was the subject of a pressure mapping experiment by the ultraviolet spectrometer (UVS) utilizing the observed amount of Rayleigh scattering (Ref. VI-9). Because the latitudes at which the *Mariner* 7 UVS viewed Hellas are almost equal, at least at the western edge of Hellas, to those measured during the *Mariner* 9 occultations, it is interesting to compare the results. The pressure measurements obtained in the *Mariner* 7 UVS experiment are plotted as open circles in Fig. VI-4. The corresponding values of altitude (relative to the mean radius) are plotted at the corresponding latitudes of measurement as open squares. Although in general the agreement is good, toward the eastern edge of Hellas the altitude measured by UVS mapping rises much more sharply than that obtained from the occultation radius measurements, and the pressure seems to drop more sharply. Also, the maximum depth at the western edge of Hellas is about 1 km less in the UVS determinations than it is in the *Mariner* 9 occultation results. The most probable explanation for these discrepancies is the divergence in latitudes of the occultation and UVS swaths toward the eastern edge of Hellas. (The latitudes differ by about 5° over Mare Hadriacum.) However, the differences also could be caused by a permanent obscuration in Hellas caused by aeolian phenomena (Ref. VI-10) similar to those that are causing a global obscuration of the surface of Mars during this mission. In that case, the UVS instrument would be able to observe the atmosphere only to the tops of the dust clouds, and possibly the lower 1 or 2 km of the Hellas basin were not mapped by the UVS in 1969.

The area was also mapped in 1969 by the *Mariner* 7 infrared spectrometer (IRS) by means of carbon dioxide absorption measurements (Ref. VI-11). The values of pressure obtained by the IRS mapping in Hellas are shown as black circles, and the corresponding altitude

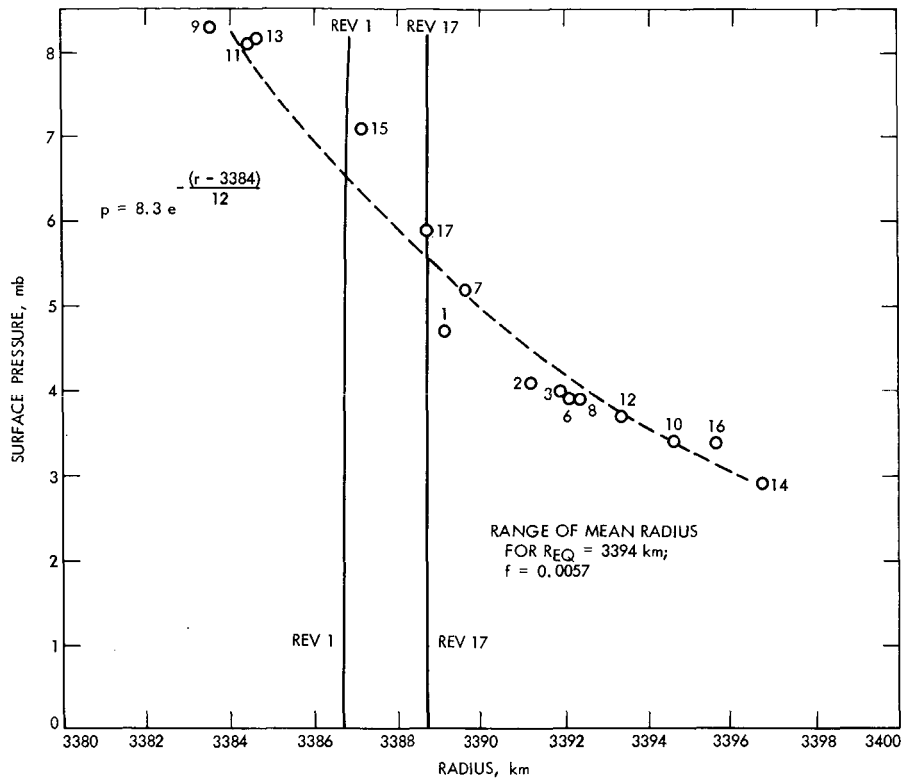

Fig. VI-4. Surface pressure and distance from the center of mass (radius) for the initial measurements. The numerals refer to the number of the revolution. The two vertical lines indicate the values of the mean radius of Mars (assuming an equatorial radius of 3394 km and a flattening of 0.0057) corresponding to the latitudes of the measurements made during Revs 1 and 17.

points, referred to the mean radius at the latitudes of the IRS measurements, are shown as black squares. Because of the relatively high scatter of these data, it is difficult to draw conclusions. However, in the western part of Hellas, the IRS measurements indicate a somewhat higher pressure and lower altitude than the UVS, a result more closely matching the current occultation measurements, and consistent with the dust obscuration hypothesis. Toward the eastern edge of Hellas both the UVS and IRS estimates diverge from the occultation observations, most likely because of differing latitudes and the effects of oblique viewing on the accuracy of the spectral measurements.

Figure VI-6 shows the variation of the radius and pressure with longitude for the points lying in the Mare Sirenum–Solis Lacus region. It can be seen immediately that, in this region, the measured radii lie substantially above the mean radius, and this is reflected in the much lower values of the surface pressure. In the range from 140° to about 90°W longitude, the measured radii lie from 5 to about 8 km above the mean radius. Although there is no Earth-based radar or carbon dioxide absorption mapping coverage in this latitude region, the general high aspect of this area is in good agreement with planetary radar profiles obtained at 14.7°S latitude (represented by triangles in Fig. VI-6).

By relating the measured surface pressure and topographical variations with the average measured temperature in the lower atmosphere, we can estimate the atmospheric pressure at the mean surface of Mars corresponding to the mean ellipsoid with an equatorial radius of 3394 km and a flattening of 0.0057. This value can be estimated as about 5.5 mb, which is in good agreement with the results obtained from *Mariners 6* and 7 (Ref. VI-3).

Data also have been obtained on the vertical distribution of ionization in the upper atmosphere. A typical

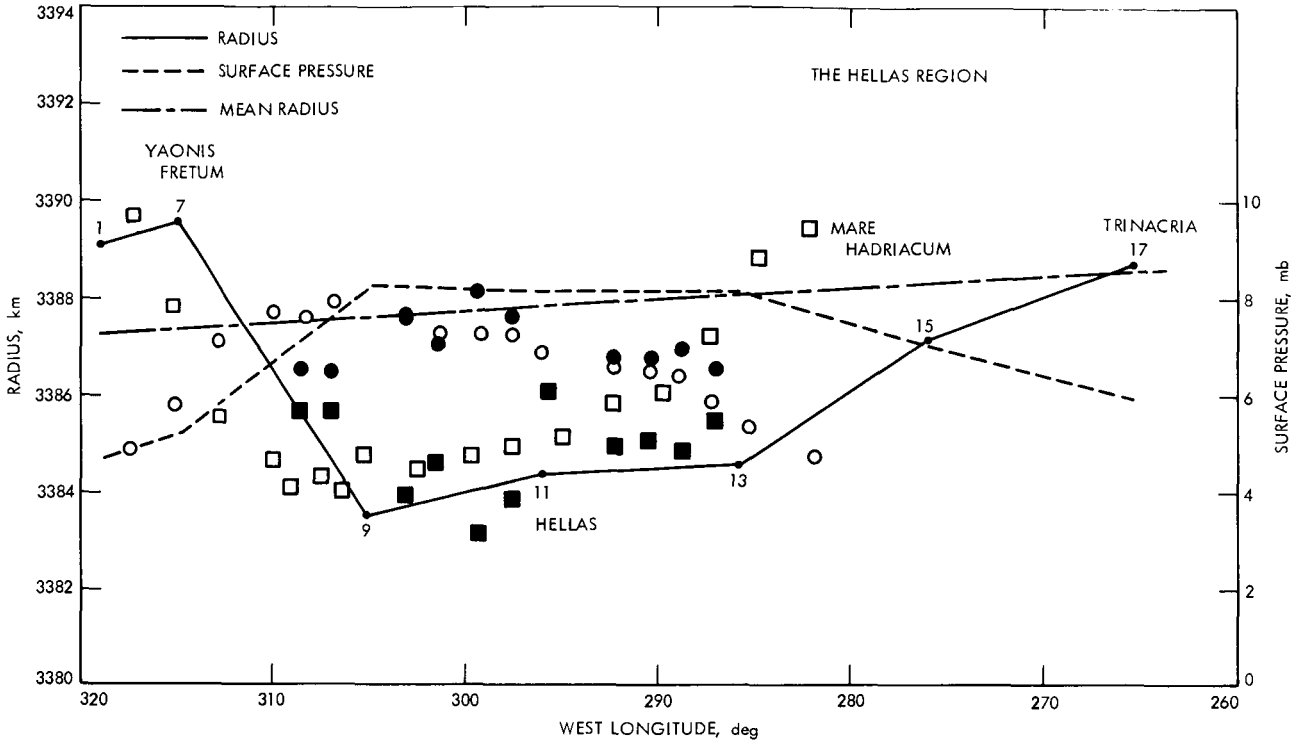

Fig. VI-5. Variation of radius and surface pressure with longitude in the Hellas region. Most of Hellas lies about 4 km below the mean radius. The plotted symbols refer to the pressure mapping results from the *Mariner 7* UVS (open circles) and IRS (solid circles).

altitude profile is presented in Fig. VI-7. These data were obtained during entry into occultation on the day side of Mars near 142.8°W longitude and 39.9°S latitude. The local time was 16.7 hr; the solar zenith angle was 56.2°. The data presented in Fig. VI-7 show that the electron density reached a maximum of about 1.5×10^5 electrons/cm^3 near 145-km altitude. The topside plasma scale height was 38 km. No clear signature of a nighttime ionosphere has been observed.

Ionospheric data processed so far cover local times from 15.9 to 16.7 hr and solar zenith angles from 54.5 to 56.6°. The results show the measurements to be remarkably reproducible from one pass to the next. For example, values obtained for the peak electron density and the topside scale height differ by less than 5%. The altitude of the ionization peak changes somewhat from one pass to another, but this effect is due primarily to elevation differences on the surface.

The results reported here show that the density and temperature of the Martian ionosphere have been reduced since 1969 (Ref. VI-4), but are higher than during the quiet solar conditions prevailing at the time of the *Mariner 4* mission to Mars in 1965. However, the most notable difference between measurements from *Mariner 9* and those from earlier spacecraft is the increased altitude of the ionization peak, which shows that the atmospheric regions below 145 km are warmer than before. This observation is consistent with the measured temperatures in the lower atmosphere.

The analysis of a small part of the expected amount of data has already produced interesting and significant results. Continuing analysis of these and other data not only will provide many more measurements of the atmosphere, ionosphere, and topography in the mid-latitudes of Mars, but some measurements of these quantities at high northern latitudes will also provide information for a precise determination of the physical shape of Mars. Many measurements of the ionosphere at varying solar illumination angles also will lead to a better understanding of the photochemical processes in the upper atmosphere of Mars.

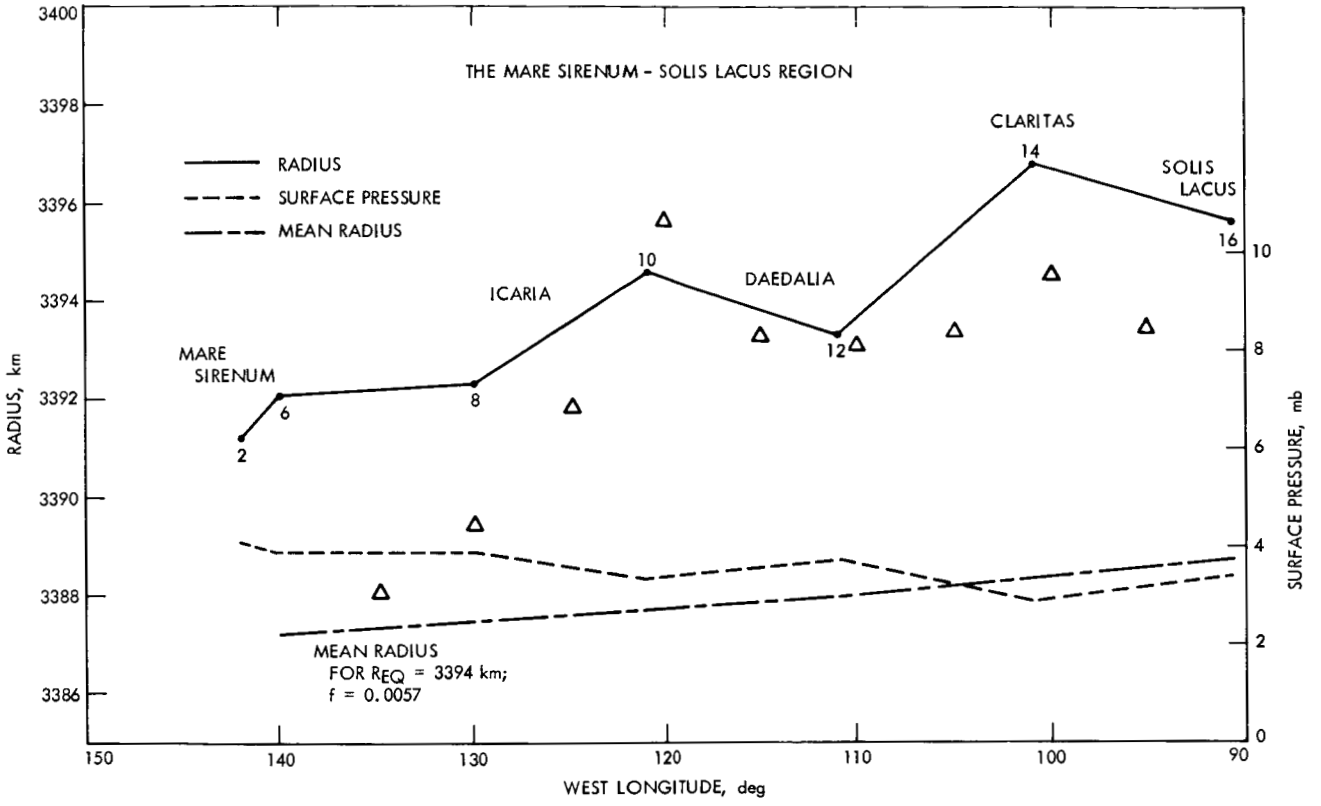

Fig. VI-6. Variation of radius and surface pressure with longitude in the Mare Sirenum–Solis Lacus region. This area is elevated above the mean radius by 4 to 8 km. The triangles indicate elevations measured to the planetary ranging radar at 14.7°S latitude.

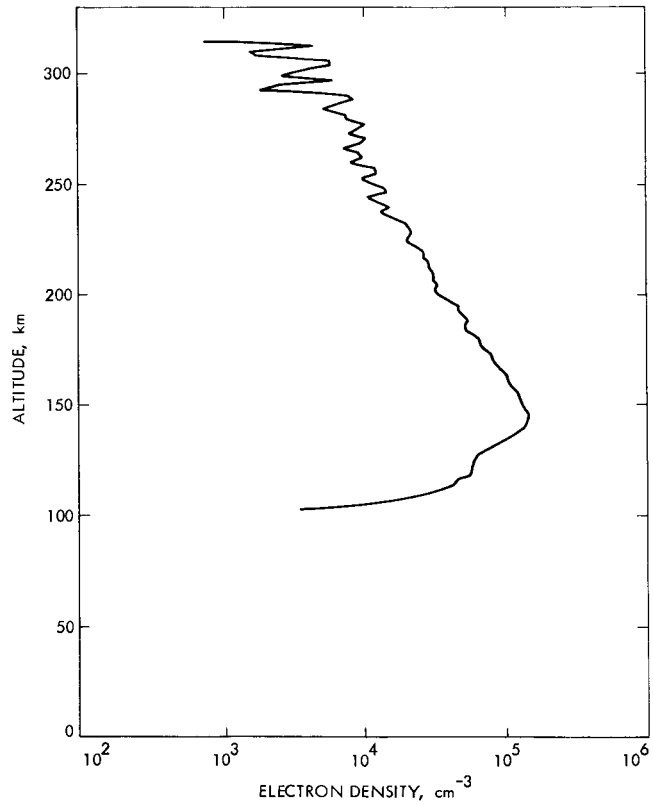

Fig. VI-7. Electron density in the ionosphere of Mars versus altitude. This measurement was made on the day side of Mars during Rev 2.

References

VI-1. Kliore, A. J., Cain, D. L., and Levy, G. S., in *Moon and Planets, Space Research VI*, p. 226, Amsterdam, 1967.

VI-2. Fjeldbo, G., and Eshleman, V. R., *Planet. Space Sci.*, Vol. 16, p. 1035, 1968.

VI-3. Kliore, A. J., Fjeldbo, G., and Seidel, B. L., in *Space Research XI*, p. 165, Akademie-Verlag, Berlin, 1971.

VI-4. Fjeldbo, G., Kliore, A. J., and Seidel, B. L., *Radio Science*, Vol. 5, p. 381, 1970.

VI-5. Kliore, A. J., *Proceedings of the Workshop on the Mathematics of Profile Inversion*, Ames Research Center, Moffett Field, Calif. (to be published). Fjeldbo, G., and Eshleman, V. R., Op. cit.

VI-6. Gierasch, P., and Goody, R., *Planet. Space Sci.*, Vol. 16, p. 615, 1968.

VI-7. Rogers, A. E. E., Ash, M. E., Counselman, C. C., Shapiro, I. I., and Pettengill, G. H., *Radio Science*, Vol. 5, p. 465, 1970. Goldstein, R. M., Melbourne, W. G., Morris, G. A., Downs, G. S., and O'Handley, D. A., *Radio Science*, Vol. 5, p. 475, 1970. Pettengill, G. H., Rogers, A. E. E., and Shapiro, I. I., *Science*, Vol. 174, p. 1321, 1971.

VI-8. Kliore, A., *Bull. Am. Astron. Soc.*, Vol. 2, p. 202, 1970.

VI-9. Barth, C. A., and Hord, C. W., *Science*, Vol 173, p. 197, 1971. Hord, C. W., *Icarus* (to be published).

VI-10. Sagan, C., Veverka, J., and Gierasch, P., *Icarus*, Vol. 15, p. 253, 1971.

VI-11. Herr, K. C., Horn, D., McAffee, J. M., and Pimentel, G. C., *Astron. J.*, Vol. 75, p. 833, 1970.

Acknowledgement

Appreciation is extended to the personnel of the Mariner Mars 1971 Project and the Deep Space Network at JPL for their competence in data delivery. Appreciation also is extended to M. J. Sykes for his contribution to data analysis and to J. W. Zielenbach for supplying excellent navigation data.

VII. Celestial Mechanics Experiment: Gravity Field and Pole Direction of Mars

J. Lorell, G. H. Born, E. J. Christensen, J. F. Jordan, P. A. Laing, W. L. Martin, and W. L. Sjogren
Jet Propulsion Laboratory, Pasadena, California

I. I. Shapiro, R. D. Reasenberg, and G. L. Slater
Massachusetts Institute of Technology, Cambridge

The preliminary results on the gravity field of Mars and the direction of its spin axis obtained from the *Mariner 9* radio tracking data provide the basis for this report. These data consist primarily of counted doppler (changes in the round-trip phase delay of the radio signal), converted to values averaged over 1-min count times.[1] The observations span two periods[2]: (1) from orbit insertion on November 14 to the orbit trim on November 16, 1971; and (2) from November 16 to December 3, 1971. The first period consists of almost four complete revolutions; the second consists of 33. The characteristics of the orbit before and after the trim are given in Table VII-1.

[1]These data were obtained primarily at Deep Space Stations at Goldstone, California (Stations 12 and 14); Madrid, Spain (62); and Woomera, Australia (41). Apoapsis data were compressed to values averaged over 10 min.

[2]Tracking data obtained before orbit insertion also have been analyzed for science information. In particular, S. K. Wong and S. J. Reinbold have processed a 3-month arc, obtaining one of the best determinations to date of the Earth–Moon ratio. This new value is 81.3007 ±0.0003, consistent with previous spacecraft results (see Ref. VII-1); the uncertainty is due primarily to that of the Earth–Moon distance.

The doppler data are affected noticeably by the inhomogeneities in Mars' gravity field and thus by its rotation vector. To estimate the parameters associated with these characteristics, the data were compared with precise theoretical computations based on double-precision numerical integration of the equations of motion

Table VII-1. Characteristics of the *Mariner 9* orbit

Parameter	Pre-trim	Post-trim
Epoch (UT)	Nov. 14, 00:42	Nov. 16, 02:58
Semi-major axis, km	13,046	12,636
Eccentricity	0.63282	0.62173
Inclination to Mars equator, deg	64.35	64.37
Latitude of periapsis, deg	−22.7	−22.1
West longitude of initial periapsis, deg	102.3	117.2
Periapsis altitude, km	1397	1387
Anomalistic orbital period, hr	12.567	11.980

of the spacecraft with respect to Mars. These equations included the perturbing accelerations due to the gravity field of Mars, the Sun and planets, direct sunlight pressure, and gas leakages. The Earth–Mars orbit was fixed in accord with determinations based on inner-planet radar data.[3] Tracking station locations were based on determinations from past *Mariner* missions with the rotational motions of the Earth modeled in the standard manner. To account for the effects of the propagation medium, semi-empirical models of the atmosphere and ionosphere were used. The relevant variational equations were integrated numerically in double precision; the parameters estimated in the first solution were: the six initial conditions, or state vector, for the spacecraft's orbit; 35 coefficients in the gravity model; and the right ascension, α, and declination, δ, of Mar's rotation axis. The gravity-field potential was represented by a spherical harmonic expansion:

$$U = -\frac{GM_{♂}}{r}\left[1 - \sum_{n=2}^{\infty} J_n \left(\frac{R}{r}\right)^n P_{n0}(\sin\theta) + \sum_{n=2}^{\infty}\sum_{m=1}^{n}\left(\frac{R}{r}\right)^n P_{nm}(\sin\theta)\,(C_{nm}\cos m\lambda + S_{nm}\sin m\lambda)\right]$$

where G is the constant of gravitation; $M_{♂}$ is the mass of Mars, fixed at the value obtained from the *Mariner 4* flyby[4]; R is the equatorial radius of Mars, taken as 3394 km; r is the radial distance of *Mariner 9* from Mars; and P_{nm} denotes the associated Legendre polynomials, with θ the latitude and λ the longitude on Mars. All coefficients through the fifth degree plus the even-order sixth degree were included for this solution except for S_{21} and C_{21}, which were omitted because of the presence of the pole angles α and δ as parameters.[5] The result for the pole position is given in Table VII-2 and is compared with the accepted value based on optical observations from the Earth (Ref. VII-4). Also listed are two other determinations based on pictures taken by the *Mariner* television camera. The first of these (from S. N. Mohan), obtained by tracking features on the surface of Mars from a series of far-encounter pictures, is in agreement with the accepted value and is of comparable accuracy. The second (from T. C. Duxbury), based on pictures of Phobos and Deimos and on the assumption that the orbital inclinations of these satellites to the Martian equator were known to within 0.2°, also gives a result for the pole direction consistent with both the nominal and that deduced from the radio tracking data, but has an uncertainty of about 0.5° in both coordinates. To test the significance of the pole direction correction implied by the radio data, several solutions were made from disjoint data sets with the pole direction alternately fixed at the radio and optical values and with S_{21} and C_{21} added to the parameter set. In all cases, the "radio" pole yielded substantially smaller values for S_{21} and C_{21}, which tends to support the radio value. Ultimately, *Mariner 9* should yield a pole direction with an uncertainty no greater than about 0.1°.

Table VII-2. Direction of the pole of Mars[a]

Angle	Nominal (Ref. VII-3)	Orbit-phase radio tracking data	Far-encounter television pictures of landmarks	Far-encounter television pictures of Martian satellites
Right ascension, α, deg	316.9	317.3 ±0.3	317.5 ±0.9	317.2 ±0.5
Declination, δ, deg	53.0	52.6 ±0.2	52.9 ±0.9	52.9 ±0.3

[a]Pole given for epoch 1971.9 and referred to mean equinox and equator of 1950.0.

Of greater direct scientific interest is the solution for the gravity field itself. In view of the *Mariner 9* periapsis altitude, which corresponds to about 1/15 of the circumference of Mars, the tracking data will yield some information on harmonics up to the 15th degree and order. However, a meaningful, complete solution of this extent will probably not be obtained from *Mariner 9*; its large orbital eccentricity, near-critical inclination[6], and near-resonant period imply that only for a small portion of

[3]Effects on the doppler data due to drifts in these ephemerides were estimated to be no more than a few milliHertz during the month after the insertion of *Mariner 9* into orbit.

[4]This value (3,098,708 ±9 in units of inverse solar masses) was determined by G. W. Null (see Ref. VII-2).

[5]It is assumed that the rotation axis coincides with the principal axis of the maximum moment of inertia, which in turn defines our body-fixed Z-coordinate axis. If the direction of this axis in our inertial frame is known precisely, then estimates of C_{21} and S_{21} should tend to zero as these coefficients will be proportional to off-diagonal terms of the moment of inertia tensor which vanish identically in this coordinate system. If the pole direction were not estimated and if it were in error, then non-zero values would in general be obtained for C_{21} and S_{21}. For a quantitative assessment, see Ref. VII-3).

[6]At an inclination of about 63° (where $\cos^2\theta = 0.2$) the first-order long-period motion of periapsis due to J_2 vanishes.

the planet near the periapsis latitude of $-22°$ will the tracking data be sensitive to gravity anomalies of this order. Further, the estimates of the coefficients of the terms of intermediate degree and order will be highly correlated with one another. For the limited span of observations presently available, solutions for the individual terms are considered reliable only through the second degree; these are shown in Table VII-3. The uncertainties given are based on the above facts and on comparisons of results from three almost complete sixth-degree solutions that utilized disjoint data sets bounded by periapsis passages. The first contained data from Orbital Revolutions (Revs) 4 to 10, the second from Revs 19 to 25, and the third from Revs 31 to 37. The value for J_2 is in excellent agreement with Wilkins' value, which was based primarily on Earth-based telescopic observations of Phobos between 1877 and 1928 (Ref. VII-5). The values for C_{22} and S_{22} imply that the fractional difference, $(B - A)/M_\sigma R^2$, in the equatorial principal moments of inertia is $(2.5 \pm 0.5) \times 10^{-4}$ and that the axis of minimum moment of inertia passes approximately through 105°W longitude.

Although the other individual terms for the sixth-degree solutions are not too meaningful, the ensemble is perhaps more reliable. The contours of constant equivalent surface heights are similar for the three solutions; the contours for the first solution, omitting the effect of J_2, are shown in Fig. VII-1. The deviations from a spheroid are seen to vary from about $-2\frac{1}{2}$ to $+3$ km. These variations imply substantial stresses and, if confirmed by further analysis, will establish Mars as gravitationally much "rougher" than either the Earth or the Moon. Scaling the variations with the square of the surface accelerations of gravity,[7] the comparative results shown in Table VII-3 are obtained for the three bodies for equivalent surface resolution.

The gravity solutions were limited to data covering six orbital revolutions, and thus do not extract all of the gravity information inherent in the complete set of observations. This assertion is supported by the results from predictions which exhibit gradually increasing residuals to about 10 Hz after several revolutions. The post-fit residuals for the data used in the solutions nowhere exceed about 0.05 Hz, as compared with the observed noise level of 0.005 Hz. With more data, the gravity solution at least near the periapsis latitude will be of finer resolution. Even with the present limited data set, short-arc fits covering the periapsis region can be used for local determinations. Residuals obtained from several short-arc solutions near periapsis in which only the spacecraft state vector was estimated are displayed in Fig. VII-2. Consistency between solutions for arcs with almost the same periapsis point on the Martian surface is evident, as is the disparity for periapsis corresponding to positions on opposite sides of Mar. Analysis of these residuals to estimate the high-frequency gravity variations, which may possibly reveal the presence of mascons, has not been completed. Later in the mission, when the orbit geometry improves and Earth occultations end, the data will be much more favorable for this type of analysis.

[7]This scaling law follows from the assumption that gravity anomalies are equivalent if corresponding surface mass anomalies produce equal stresses (see, for example, Ref. VII-6).

Table VII-3. Coefficients for second-degree harmonics of gravity field[a]

Coefficient	Nominal (Ref. VII-5)	*Mariner 9*	Moon[b]		Earth (Ref. VII-11)	
			Unscaled	Scaled to Mars (see text footnote 7)	Unscaled	Scaled to Mars (see text footnote 7)
J_2	$(1.986 \pm 0.006) \times 10^{-3}$	$(1.96 \pm 0.01) \times 10^{-3}$	$(0.200 \pm 0.002) \times 10^{-3}$	—	1.083×10^{-3}	—
C_{21}	0	$<3 \times 10^{-6}$	—	—	—	—
S_{21}	0	$<3 \times 10^{-6}$	—	—	—	—
C_{22}	—[c]	$-(5 \pm 1) \times 10^{-5}$	$(2.4 \pm 0.5) \times 10^{-5}$	0.5×10^{-5}	0.16×10^{-5}	1.0×10^{-5}
S_{22}	—[c]	$(3 \pm 1) \times 10^{-5}$	$(0.5 \pm 0.6) \times 10^{-5}$	0.1×10^{-5}	-0.09×10^{-5}	-0.6×10^{-5}

[a]Referred to radius of 3394 km.

[b]Moon gravity models, as obtained from *Lunar Orbiter* data, are still subject to large uncertainty (see Ref. VII-9). Perhaps the best model is that obtained by P. A. Laing and A. S. Liu (see Ref. VII-10), whose values are used in this table.

[c]No value available before *Mariner 9* missions.

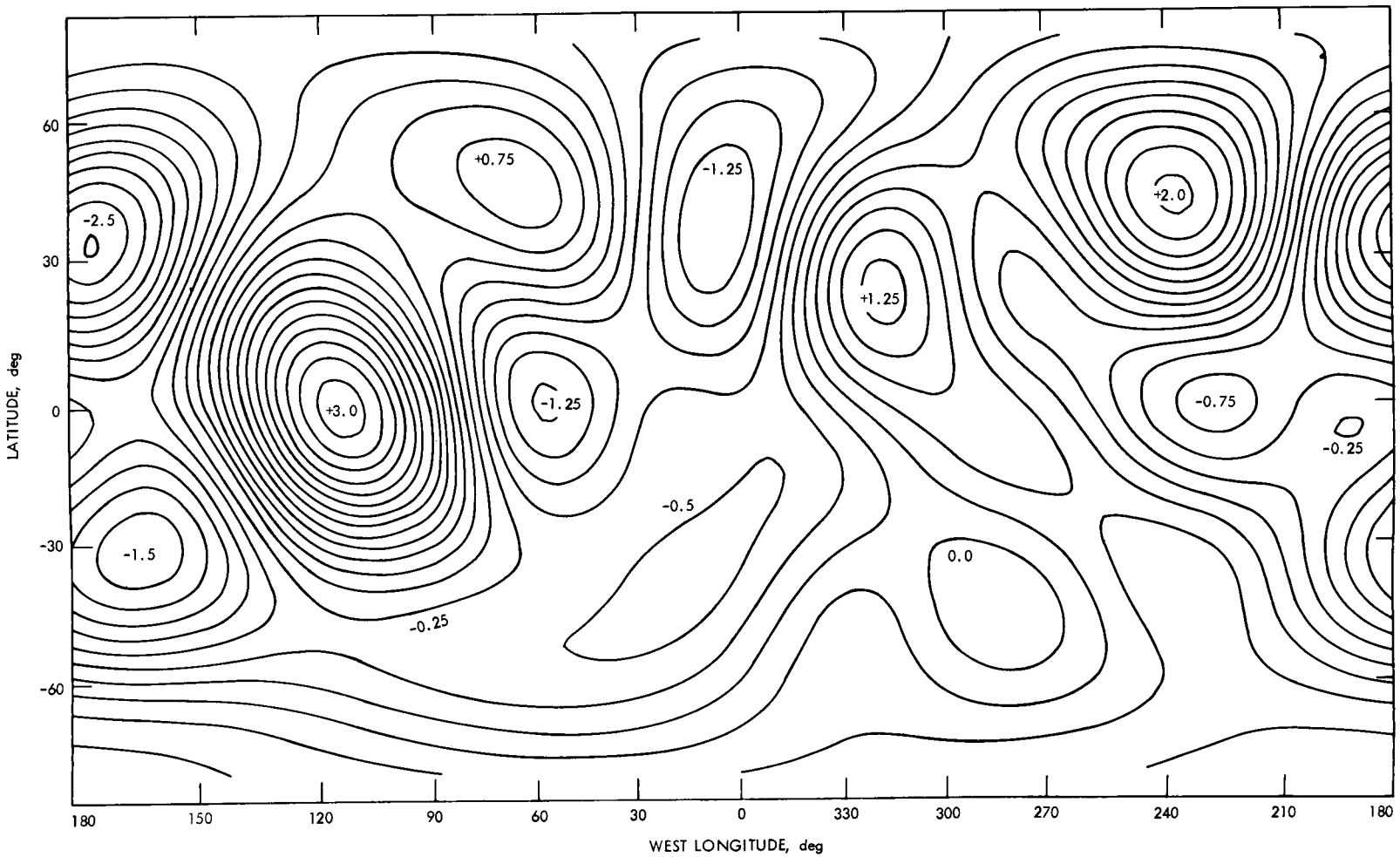

Fig. VII-1. Contours of equivalent surface heights deduced from a sixth-degree solution for the Martian gravity field. These contours represent the deviations from sphericity of a uniformly dense body with external potential given by the first sixth-degree solution, omitting the effect of J_2. Contours are labeled in kilometers; the contour interval is 250 m.

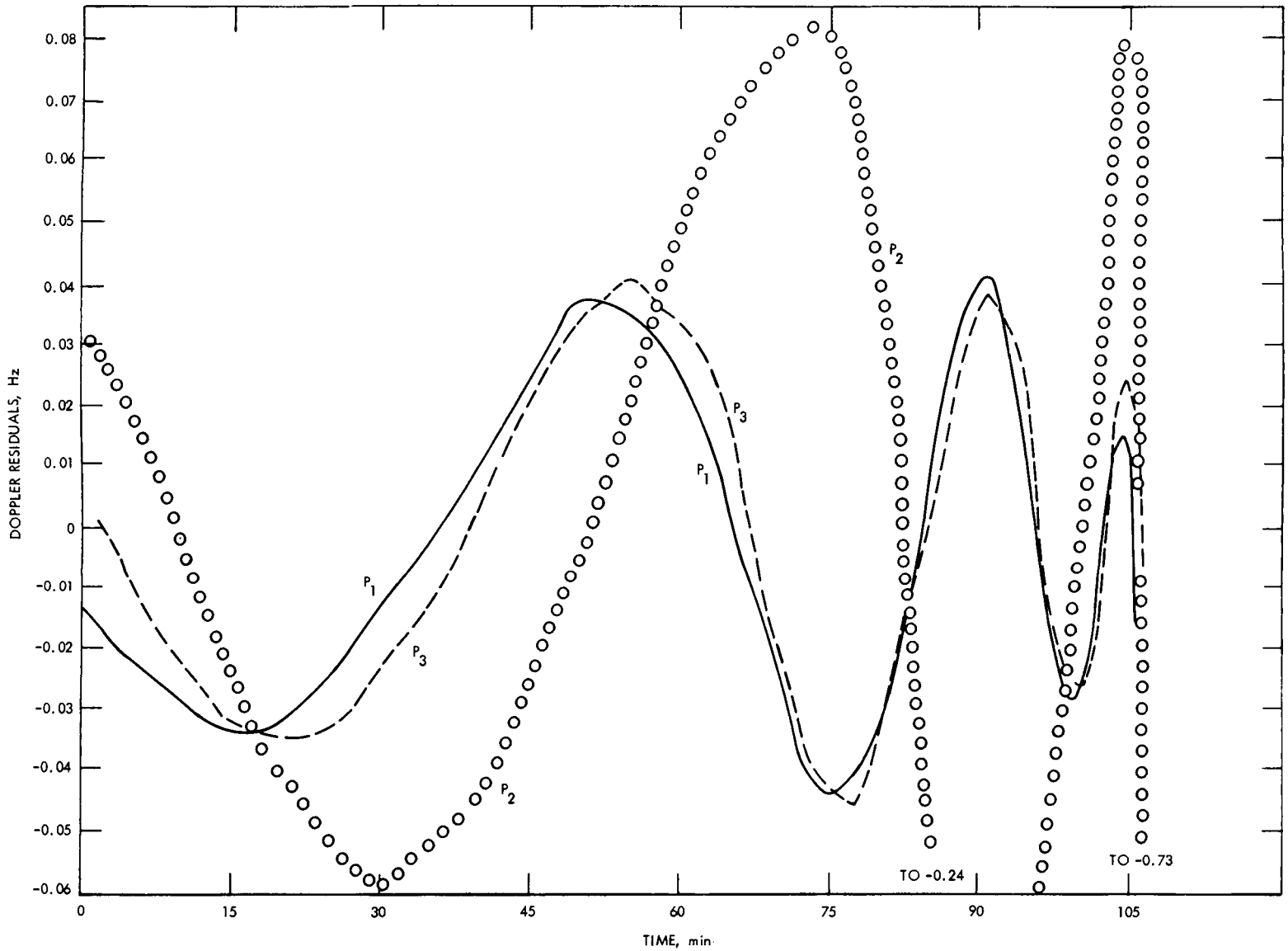

Fig. VII-2. Residuals from short-arc fits near the first three periapsis passages of *Mariner* 9. Only the state vector was estimated; the residuals represent the effects of the Martian gravity field. The results for the first and third passages, P_1 and P_2, are similar because the orbital period was almost half of the spin period of Mars (see Table VII-1). For the radio frequency of about 2300 MHz, 1 mm/sec $\cong$ 0.015 Hz. Near periapsis passage, which occurred at about $t = 102$ min, the speed of *Mariner* 9 was about 4 km/sec. Earth occultation precluded extension of the data past periapsis.

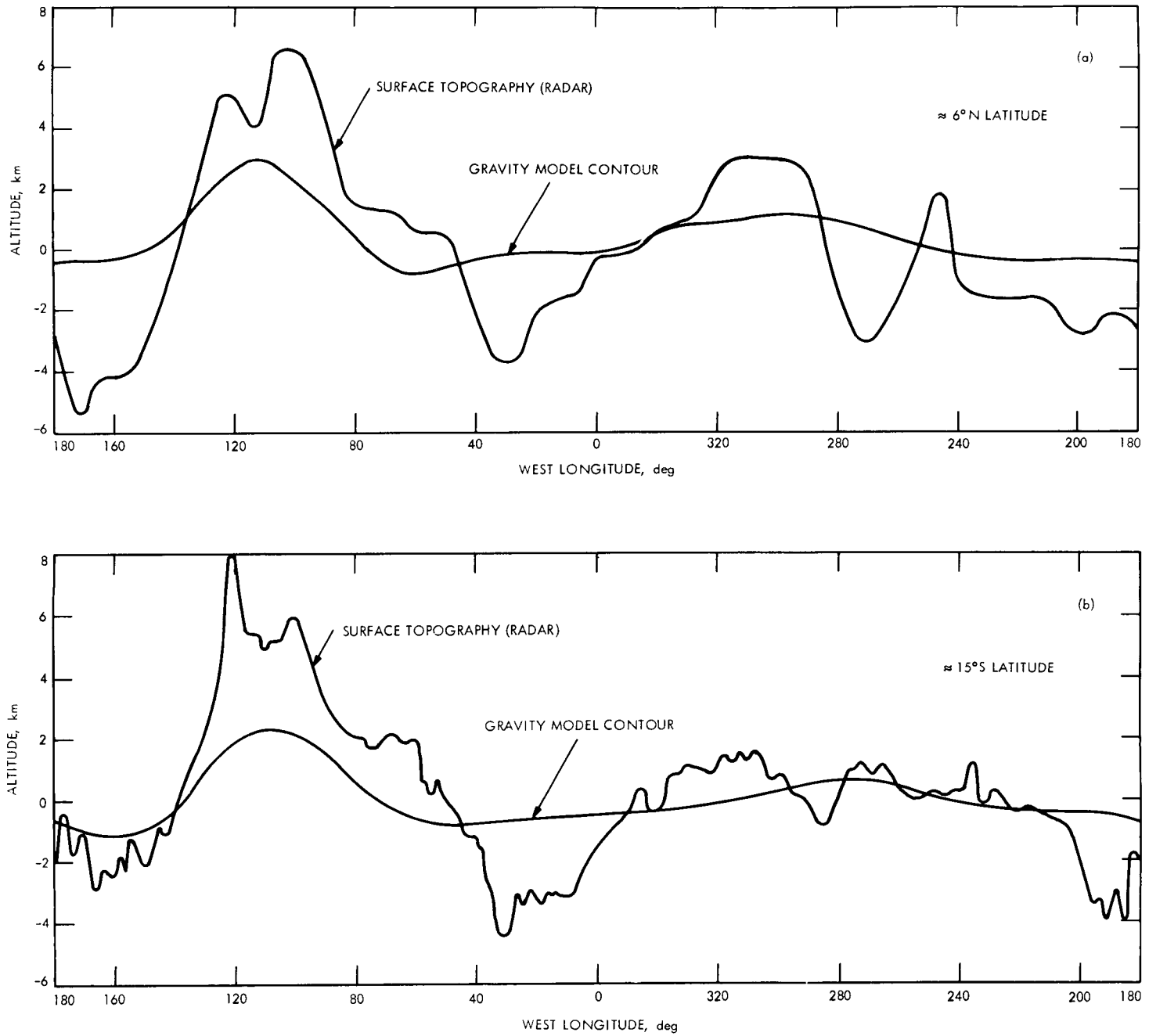

Fig. VII-3. Comparison of surface contours deduced from sixth-degree gravity model (see Fig. VII-1) with radar measurements (Ref. VII-7) of surface-height variations near the Martian equator. The 1971 radar data (b) are of substantially higher resolution than the 1969 data (a).

Comparison of the gravity contours exhibited in Fig. VII-1 with surface heights determined from Earth-based radar observations (Ref. VII-7) is instructive. The radar data are confined to the equatorial region ($\pm 20°$ in latitude); therefore, Fig. VII-3 shows surface heights for two representative latitudes as compared with the corresponding gravity-potential contours. The low-frequency components of the surface-height variations correlate well with those of the gravity-potential contours. In particular, the gravity contours peak within about 20° of the surface-height maxima. In some places the amplitudes of the variations in surface heights are several-fold larger than those in the gravity contours. Such disparities are probably attributable to the averaging effect of the low-resolution gravity model and to isostatic compensation. A quantitative apportionment must await the development of a better gravity model.

Measurements of surface pressure from other experiments[8] (see Sections III, V, and VI of this document), when combined with the gravity contours, also can be used to infer surface-height variations. Comparisons with the radar determinations, where they exist, will then allow important closure tests to be made. Only low-frequency components of the topography can be inferred because of the restricted surface resolution of the gravity data.

[8]S-band occultation data also determine the radius of Mars at the point of occultation and can therefore be used to deduce gravity-field variations independently.

No useful upper bound on the density of the Martian exosphere at the periapsis altitude has been obtained as yet. This density affects the doppler tracking data through the drag on the spacecraft, which in turn manifests itself most sensitively through secular changes in the orbital mean anomaly. The gravity-field variations, which also affect the mean anomaly, are periodic, thus affording a method of separation. Several rotations of Mars with respect to the spacecraft's position at periapsis probably are required for separation. Each such rotation takes about 20 days. The present analysis allows us to conclude only that the air density at periapsis is no greater than about 10^{-15} g/cm^3; most likely, it is far less.

In addition to doppler observations, ranging or group-delay measurements have been made regularly since orbit insertion. These latter data will be used to test the predicted general relativistic effect of solar gravity on the round-trip delays (see, for example, Ref. VII-8) and, concomitantly, to improve the determination of the orbits of Earth and Mars. The data now extend over too small an arc for any scientific conclusions to be drawn. Continuation well past the superior conjunction of September 1972 is required for an accurate relativity test. Corresponding improvements in the orbits of Earth and Mars will then be sufficient to allow radar echo-delay data to be interpreted directly in terms of surface heights. Substantial improvements will also be possible in the interpretations of the Earth–Mercury and Earth–Venus radar observations.

References

VII-1. Anderson, J. D., Efron, L., and Wong, S. K., *Science*, Vol. 167, p. 277, 1970.

VII-2. Null, G. W., *Bull. Am. Astron. Soc.*, Vol. 1, p. 356, 1969.

VII-3. Lorell, J., *J. Astronaut. Sci.* (to be published).

VII-4. de Vaucouleurs, G., *Icarus*, Vol. 3, p. 236, 1964.

VII-5. Wilkins. G., in *Mantles of the Earth and Terrestrial Planets*, p. 77, S. Runcorn, Ed., Interscience Publishers, London, 1967.

VII-6. Kaula, W. M., in *Trajectories of Artificial Celestial Bodies*, J. Kovalevsky, Ed., Springer-Verlag, Berlin, 1966.

References (contd)

VII-7. Pettengill, G. H., Counselman, C. C., Rainville, L. P., and Shapiro, I. I., *Astron. J.*, Vol. 74, p. 461, 1969. Rogers, A. E. E., Ash, M. E., Counselman, C. C., Shapiro, I. I., and Pettengill, G. H., *Radio Science*, Vol. 5, p. 465, 1970. Goldstein, R. M., Melbourne, W. G., Morris, G. A., Downs, G. S., and O'Handley, D. A., *Radio Science*, Vol. 5, p. 475, 1970. Pettengill, G. H., Rogers, A. E. E., and Shapiro, I. I., *Science*, Vol. 174, p. 1321, 1971. Downs, G. S., Goldstein, R. M., Green, R. R., and Morris, G. A., *Science*, Vol. 174, p. 1324, 1971.

VII-8. Anderson, J. D., Esposito, P. B., Martin, W. L., and Muhleman, D. O., in *Proceedings of the Conference on Experimental Tests of Gravitation Theories*, p. 111, R. W. Davies, Ed., Technical Memorandum 33-499, Jet Propulsion Laboratory, Pasadena, Calif., 1971. Shapiro, I. I., Ash, M. E., Ingalls, R. P., Smith, W. B., Campbell, D. B., Dyce, R. B., Jurgens, R. F., and Pettengill, G. H., *Phys. Rev. Letters*, Vol. 26, p. 1132, 1971.

VII-9. Lorell, J., *The Moon*, Vol. 1, p. 190, 1970.

VII-10. Laing, P. A., and Liu, A. S., *Science*, Vol. 173, p. 1017, 1971.

VII-11. Gaposchkin, E. M., and Lambek, K., *J. Geophys. Res.*, Vol. 76, p. 4855, 1971.

Acknowledgment

Thanks are extended to D. L. Cain, R. M. Georgevic, A. S. Liu, H. N. Royden, G. Sherman, S. Synnot, and the *Mariner* 9 Navigation Team, especially J. W. Zielenbach and D. H. Boggs, for their important contributions. Appreciation also is extended to T. C. Duxbury, S. N. Mohan, S. K. Wong, and S. J. Reinbold for permitting us to quote their results prior to publication.

NASA — JPL — Coml., L.A., Calif.